Virginia Commonwealth University

VCU Scholars Compass

2007

Drift Tube Ion Mobility Measurements for Thermochemistry, Kinetics and Polymerization of Cluster Ions

Ridha Ben Mohsen Mabrouki
Virginia Commonwealth University

www.manaraa.com

DRIFT TUBE ION MOBILITY MEASUREMENTS FOR THERMOCHEMISTRY,
KINETICS AND POLYMERIZATION OF CLUSTER IONS

A Dissertation submitted in partial fulfillment of the requirements for the degree of
Doctor of Philosophy at Virginia Commonwealth University.

by

RIDHA BEN MOHSEN MABROUKI
B.Sc., University of Life Science of Sfax, Tunisia, 1998

Director: M. SAMY EL-SHALL
PROFESSOR, DEPARTMENT OF CHEMISTRY

Virginia Commonwealth University
Richmond, Virginia
May 2007

Acknowledgement

I would like to dedicate this work to my family: my father *Mohsen ben Lakhder Mabrouki*, my mother *Fatima bent Mohammed El-Bouzidi Fatnassi*, my *brothers* my *sisters*, my wife *Halima Mabrouki* and spatially, I would like to express my gratitude to my brother *Lazhar Mabrouki* for his encouragement and support to complete this project.

I am grateful to my advisor Professor *Samy El-Shall* who encouraged and offered me the opportunity to pursue PhD. and his efforts to guide me to have my steps in the right path. I would like to thank my colleagues: Dr. *Yehia Ibrahim*, Dr. *Hatem Mahmoud* and Dr. *Edreese Alsharaeh*, who offered the technical help. I cannot forget to thank all my friends and teachers from elementary to graduate school for their contributions to my knowledge.

Table of Contents

List of Tables

List of Figures

Abstract

DRIFT TUBE ION MOBILITY MEASUREMENTS FOR THERMOCHEMISTRY,

KINETICS AND POLYMERIZATION OF CLUSTER IONS

By RIDHA BEN MOHSEN MABROUKI, PHD

A Dissertation submitted in partial fulfillment of the requirements for the degree of Doctor
of Philosophy at Virginia Commonwealth University.

Virginia Commonwealth University, 2007

Major Director: M. Samy El-Shall
PhD., Professor, Department of Chemistry

In this work, the Drift Tube Ion Mobility technique is used to study the hydrophobic hydration and solvation of organic ions and measure the thermochemistry and kinetics of ion-molecule reactions. Furthermore, an exploratory study of the intracluster polymerization of isoprene will be presented and discussed.

The ion hydration study is focused on the $C_3H_3^+$ cation[1] and Pyridine$^{•+}$ radical cation.[2] The chemistry of the cyclic $C_3H_3^+$ cation has received considerable attention and continues to be an active area of research.[3-7] The binding energies of the first 5 H_2O

molecules to c-$C_3H_3^+$ were determined by equilibrium measurements. The measured binding energies of the hydrated clusters of 9-12 kcal/mol are typical of carbon-based $CH^+{\cdots}X$ hydrogen bonds. The ion solvation with the more polar CH_3CN molecules results in stronger bonds consistent with the increased ion-dipole interaction. Ab initio calculations show that the lowest energy isomer of the c-$C_3H_3^+(H_2O)_4$ cluster consists of a cyclic water tetramer interacting with the c-$C_3H_3^+$ ion, which suggests the presence of orientational restraint of the water molecules consistent with the observed large entropy loss. The c-$C_3H_3^+$ ion is deprotonated by 3 or more H_2O molecules, driven energetically by the association of the solvent molecules to form strongly hydrogen bonded $(H_2O)_nH^+$ clusters. The kinetics of the associative proton transfer (APT) reaction $C_3H_3^+ + nH_2O \rightarrow (H_2O)_nH^+ + C_3H_2^{\bullet}$ exhibits an unusually steep negative temperature coefficient of $k = cT^{63\pm4}$ (or activation energy of -32 ± 1 kcal mol^{-1}). The behavior of the $C_3H_3^+$/water system is exactly analogous to the benzene$^{+\bullet}$/water system[8, 9], suggesting that the mechanism, kinetics and large negative temperature coefficients may be general to multibody APT reactions. These reactions can become fast at low temperatures, allowing ionized polycyclic aromatics to initiate ice formation in cold astrochemical environments.

The solvation energies of the pyridine$^{\bullet+}$ radical cation by 1- 4 H_2O molecules are determined by equilibrium measurements in the drift cell. The binding energies of the pyridine$^{\bullet+}(H_2O)_n$ clusters are similar to the binding energies of protonated pyridineH$^+(H_2O)_n$ clusters that involve NH$^+{\cdot\cdot}OH_2$ bonds, and different from those of the solvated radical benzene$^{\bullet+}(H_2O)_n$ ions that involve CH$^{\delta+}{\cdot\cdot}OH_2$ bonds. These relations indicate that the observed pyridine$^{\bullet+}$ ions have the distonic $^\bullet C_5H_4NH^+$ structure that can

form $NH^+\cdot\cdot OH_2$ bonds. The observed thermochemistry and ab initio calculations show that these bonds are not affected significantly by an unpaired electron at another site of the ion. The distonic structure is also consistent with the reactivity of pyridine$^{\bullet+}$ in H atom transfer, intra-cluster proton transfer and deprotonation reactions. The results present the first measured stepwise solvation energies of distonic ions, and demonstrate that cluster thermochemistry can identify distonic structures.

The gas phase clustering of small molecules around the hydronium ion is of fundamental interest and is relevant to important atmospheric and astrophysical processes. In this work, the equilibrium constants for the formation of the $H_3O^+(X)_n$ clusters with X = H_2, N_2 and CO and n = 1-3 at different temperatures are measured using the drift tube technique[10]. The arrival time distributions (ATDs) of the injected H_3O^+ and the $H_3O^+(X)_n$ clusters formed inside the cell are measured under equilibrium conditions. The resulting binding energies for the addition of one and two hydrogen molecules are similar [3.4 and 3.5 kcal/mol, respectively). For the N_2 clustering with n = 1-3, the measured binding energies are 7.9, 6.9 and 5.4 kcal/mol, respectively. The clustering of CO on the H_3O^+ ion exhibits a relatively strong binding energy (11.5 kcal/mol) consistent with the dipole moment and polarizability of the CO molecule. Theoretical calculations of the lowest energy structures are correlated to the experimental results.

Finally, intracluster polymerization leading to the formation of covalent bonded oligomer ions has been investigated following the ionization of neutral isoprene clusters. The results indicate that isoprene dimer cation has a structure similar to that of the limonene radical cation.

Isoprene Dimer Radical Cation
within Isoprene clusters

Limonene Radical Cation
within Isoprene clusters
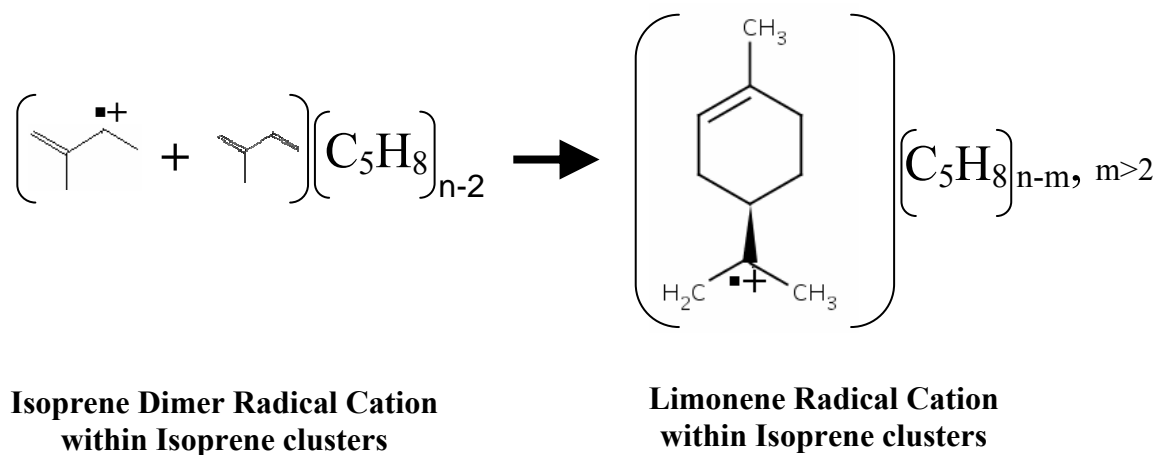
Mass-selected mobility and dissociation studies also indicate that the larger isoprene cluster ions have covalent bonded structures. The conversion of molecular clusters into size-selected oligomers is an important process not only for detailed understanding of the early stages of polymerization but also for practical applications such as the formation of new polymeric materials with controlled and unusual properties.

CHAPTER 1: Introduction

The use of the drift cell contributed to the progress and development of chemistry in general and to the thermochemistry in particular. Many research groups used and are still using the drift cell for their research.[11, 12] In our laboratory the ion mobility drift tube was used to investigate binding energies of cluster ions[1, 10, 13-15], to identify structures of organic molecules in the gas phase[16] and to study the kinetics of ion-molecule reactions in the gas phase[17].

The study of ion-molecule and cluster reactions is of fundamental interest for the understanding of intermolecular interactions, ion solvation, organic reaction mechanisms, astrochemistry and many other related fields. The thermochemistry of ion-molecule clustering reactions has been extensively studied using high pressure mass spectrometry. Energetic information has been also obtained for dissociation experiments.[18-24] An example of thermochemistry measurements done by high pressure mass spectrometry in our laboratory is the association energy of the $C_6H_6^+$ ion with neutral benzene molecules. The measured enthalpy and the entropy of the reaction of $C_6H_6^+$ with one molecule of benzene C_6H_6 are -17.7 kcal.mol^{-1} and -27.4 cal.mol^{-1}.K^{-1} respectively [25]. Also in our lab, the benzene-pyridine system was investigated and the strength of the clustering bond of $(C_6H_6.C_5H_5N)^{\bullet+}$ was studied. Structures of molecular clusters, oligomers, and large biological ions have been determined using drift tube (ion mobility) measurements. The mobility of an ion through a buffer gas depends on its average collision cross section, which in turn depends on its conformation. Ions with open structures undergo more

collisions with the buffer gas and travel more slowly than ions with compact structures[26-28]. Recently, the structure of benzene cluster ions (1-6) were determined by drift cell mobility measurements[29]. The structures of benzene cluster ion isomers (generated by EI ionization) have been determined and several isomers were identified[25]. The same ion-mobility cell was used to characterize the electronic states of a series of transition metal cations (V^+, Cr^+, Fe^+, Ni^+, Cu^+, Zr^+, Nb^+, Mo^+, Pd^+, Ag^+ and Au^+) by measuring their mobilities at different conditions[30]. Structures of some metal-ion benzene clusters {$Ni^+(C_6H_6)_n$, $Pd^+(C_6H_6)_n$} were identified by the measurements of their mobilities in the drift cell.

For the first time, evidence of thermally self-initiated polymerization of styrene in the gas phase was provided. In this study, the mobility measurements of styrene cluster ions generated by EI ionization were achieved[31]. Information about the structure of the ionized oligomers was obtained through a combination of experimental and theoretical investigations. CID (collision induced dissociation) of selected styrene cluster ions was studied at different temperatures to confirm that the gas phase polymerization of styrene proceeds via an initiation mechanism similar to the condensed phase.

Recently, the stepwise hydration and deprotonation of the benzene radical cation by neutral water clusters in the gas phase have been reported with a steep negative temperature coefficient[8, 9]. The kinetically measured activation energy of the deprotonation of the benzene radical cation by an assembly of water molecules was found to be negative by 34 kcal. mol^{-1}.

In this work, we focus on four aspects of cluster ions. The first aspect is the thermochemistry, where the focus will be on the $C_3H_3^+$ cation and the pyridine cation. In

this section, stepwise clustering reactions with water are studied in addition to the deprotonation reactions by associated water molecules to form protonated water clusters. The thermochemistry is extended to reach the solvation of these ions by polar ligands with minor possibilities for extended hydrogen bonds network and the acetonitrile is chosen to be the one. The last part of this chapter deals with a comparison between the C_3H_3, the pyridine and the benzene cations.

The second part will focus on the solvation of organic molecules in the gas phase where the hydronium ion will be taken as an example. The binding energy of the hydronium ion was studied with different ligands. The hydrogen, nitrogen and carbon monoxide are chosen because they cover the differences in polarizability and in the dipole moment. These differences can reveal the importance and the contribution of the polarizability and the dipole moment to intermolecular interactions. Finally, following the successful study of the thermal polymerization of styrene oligomers, the cationic polymerization, structures and the mechanisms of formation of isoprene and limonene oligomers in the gas phase were investigated.

In the condensed phase, the ionic and the ion-molecule interactions are of fundamental importance in chemistry and biochemistry. The chemical and physical properties of ions and cluster ions generated by different ionization techniques (EI, MALDI, ESI or LVI) can be better understood in the absence of solvent molecules, because the presence of solvent in large number of molecules in a solution makes the ionic interactions difficult to understand. The role of the solvent could be much better understood if the same reactions are carried out in the complete absence of solvent where

the ions are "naked" or in the presence of a controlled amount of solvent molecules. The gas phase is the appropriate way to do such studies[32], where the clustering of solvent molecules around ions can be experimentally measured through successive equilibrium steps to provide useful thermochemical information.

Solvation of ions in solution can extensively affect many chemical and physical properties such as acid-base property, dielectric constant, degree of hydrogen bonding, dipole moment, polarizability, diffusion, etc. The formation of clusters in the gas phase combined with the capability of controlling the amount of solvent molecules makes it easy to follow the changes in these properties through successive steps of solvation. Cluster ions' solvation can help explain the ionic properties in solutions.

CHAPTER 2: Experimental Setup

2.1 Vacuum System

The QMS-IM-QMS, has four stainless steel vacuum chambers, as shown in Figure1 and 2. It is a home built machine designed by Dr. Mark Rusyniak and Dr. Yehia Ibrahim, two former graduate students in our laboratory. The first chamber is the cluster source chamber which is pumped by a Varian VHS-6 diffusion pump with a pumping speed of 3000 L/s (He) and backed by an Edwards E2M30 rotary vacuum pump. A typical pressure in this region is 1-9 $\times$ 10^{-5} Torr.

The second chamber is separated from the first one by a 3 mm orifice skimmer cone. This region houses the electron-impact (E.I.) ionizer and the first quadrupole mass filter assembly. It is pumped by an Edwards Diffstak 160/700 M diffusion pump with a 1300 L/s (H_2) pumping speed. A typical pressure in this region is 1-2 $\times$ 10^{-6} Torr.

The third chamber, which is the main one, houses two sets of ion lenses and the drift/reaction cell. This region is pumped by an Edwards standard Diffstak 250/2000P diffusion pump with a speed of 3000 L/s in H_2, and it is backed by an Edwards E2M40 two stage vacuum pump. The pressure in this region depends mainly on two factors: the size of the orifice of the entrance and exit plates of the drift cell, and the pressure of the gas inside the drift cell, which is typical around 10^{-5} Torr.

The last chamber houses the second quadrupole mass spectrometry assembly and the detector. This chamber has a cylindrical shape, and it is pumped by an Edwards

standard Diffstak 150/700 M diffusion pump with a speed of 1300 L/s in H_2 where the pressure is maintained at 5-9 × 10^{-7} Torr. The second and the fourth chambers share the same foreline, and they are backed by an Edwards E2M40 two stage rotary vacuum pump.

The pressure in all the chambers is controlled by ion gauges (Scientific Instrument Services ion gauge tube 3/4' Pyrex), and the foreline pressure is monitored by a thermocouple gauge tube (Edwards, type ATC-M D 355 13 000).
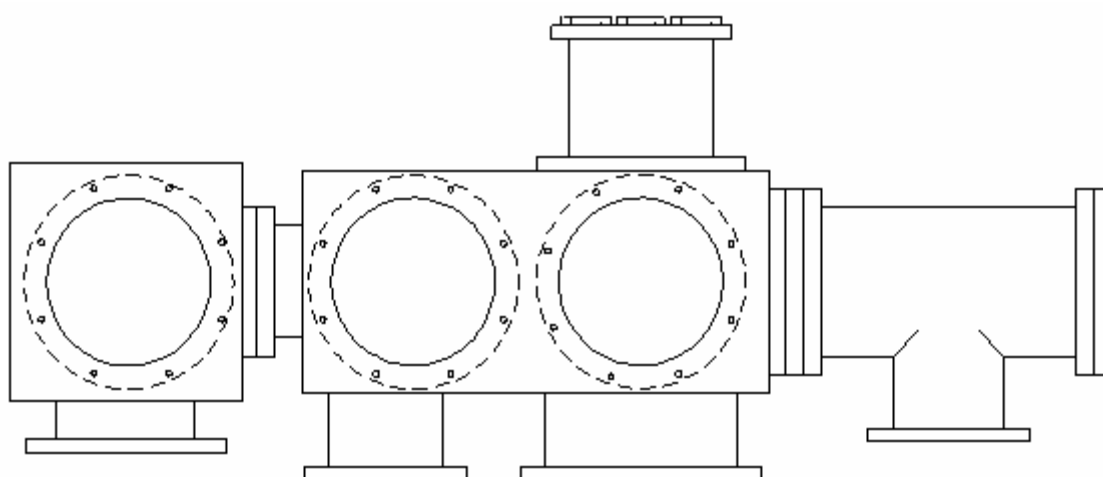
Figure 1: Front view of the instrument showing four vacuum chambers without diffusion pumps, mechanical pumps, or the forelines for clarity.
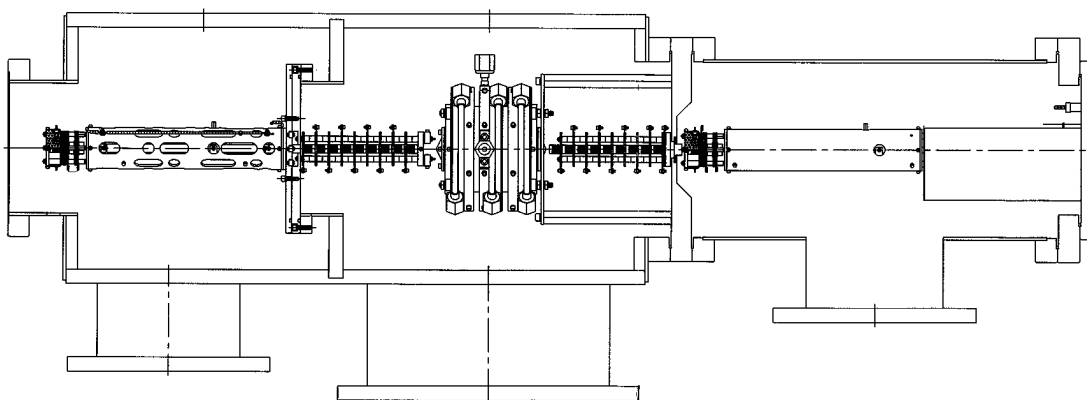
Figure 2: Cut view of the different component of the ion mobility system and their mounting structures in each of the four chambers, excluding the cluster source.

2.2 Cluster formation

The clusters are generated by a supersonic adiabatic expansion, where the vapor of a chemical compound is mixed with a carrier gas, Helium or Argon, in most cases at high pressures of 30-100 psi, then expanded in the low pressure cluster chamber ~ 10^{-7} Torr. This expansion is done by a pulsed nozzle valve operating at a frequency range from 10 to 100 Hz. Orifice of the nozzle flange vary from 0.2 to 0.5 mm. When this gas is expanded, the thermal energy of the gas in the high-pressure source is converted into a directed velocity V as the gas is expanded. If C_p and T_S are the heat capacity of the gas and the temperature of the source, respectively, the energy balance of an ideal gas of molecular weight m will be given by the following equation:

$$C_p T_S = C_p T_B + \frac{1}{2} m V^2 \qquad (1)$$

Where T_B is the beam temperature. It is clear that the temperature of the formed beam is lower than the initial temperature of the source, since $\frac{1}{2} m V^2 \geq 0$. This cooling resulting from the adiabatic expansion promotes the formation of clusters. The expansion of a gas in a collision-free region (a few nozzle diameters) creates a directed motion of the gas which leads to a decrease in the vibrational, rotational and translational temperatures. The latent heat of condensation during the clustering increases the internal temperature of the clusters. However, collisions with an inert gas provide cooling of the internal temperature of the clusters[33]

2.3 Ionization method

The QMS-IM-QMS can be combined with many types of ionization methods: Electron Impact (EI), Matrix Assisted Laser Desorption Ionization (MALDI), Electrospray Ionization (ESI) and LVI (laser vaporization ionization). In our laboratory we are using EI ionization to ionize a cluster beam formed by supersonic adiabatic expansion, and the LVI to generate metal cations. In some cases we used a dye laser, with a selected wavelength pumped by an Excimer laser to ionize a chromophore. By using a dye laser, we can set the laser to a specific wavelength which corresponds to a specific transition in the sample to populate a specific excited state. The mass spectrum in figure 3 represents a typical cluster distribution obtained by EI ionization. In some other systems[34] the EI ionization generates the singly and doubly charged cluster ions at the same time.

2.4 Drift cells and ions trajectory

The drawing in Figure 4, is a representation of the components of the ion mobility system. The trajectory of the ion in this system can be divided into four sections: in the first chamber the expansion takes place and a neutral molecular beam is generated and then skimmed by a skimmer separating the first chamber from the second one. In the second chamber the beam is ionized by electron impact ionization, (in the LVI the beam coming from the first chamber is already an ion beam), the selection of the ion can take place using the first quadrupole mass filter. The focusing and transfer of the selected ion is achieved by the first set of Einzel lenses. The beam is focused into the drift cell pinhole entrance by vertical and horizontal steering lenses. The main section is the third chamber

housing the drift cell centered between two sets of einzel lenses. The last section contains the second quarupole where the ion and/or the product formed inside the drift cell can be scanned before reaching the detector.

2.5 High temperature drift cell

The new high temperature drift cell has some differences from the old one. The major difference is the capability of reaching higher temperature (500 ^{o}C). The heating method used with the old cell did not work with the new cell, especially at high temperatures. Some modifications were needed to achieve the upper limit of the temperature including the heating wires, the type of current and the voltages applied.

The new cell is heated by tantalum wires running inside ceramic tubes which are inserted into the cell body. The cell body contains eight ceramic tubes and the end cap contains only two. The two parts are heated separately. The heat is generated from a DC current transferred from the AC current by the use of a combination of isolation transformer and a dynode conversion as a bridge rectifier. This conversion of the applied current from AC to DC is needed because the ceramic becomes conductive at high temperature and the voltage applied to the heating wires will interfere with the voltage applied to the cell. The other difference includes the shorter length where this cell is only 5 cm long, the pinhole entrance and exit are smaller where the pressure can reach up to 8 Torr and this can contribute to the mobility measurements by increasing the resolution.
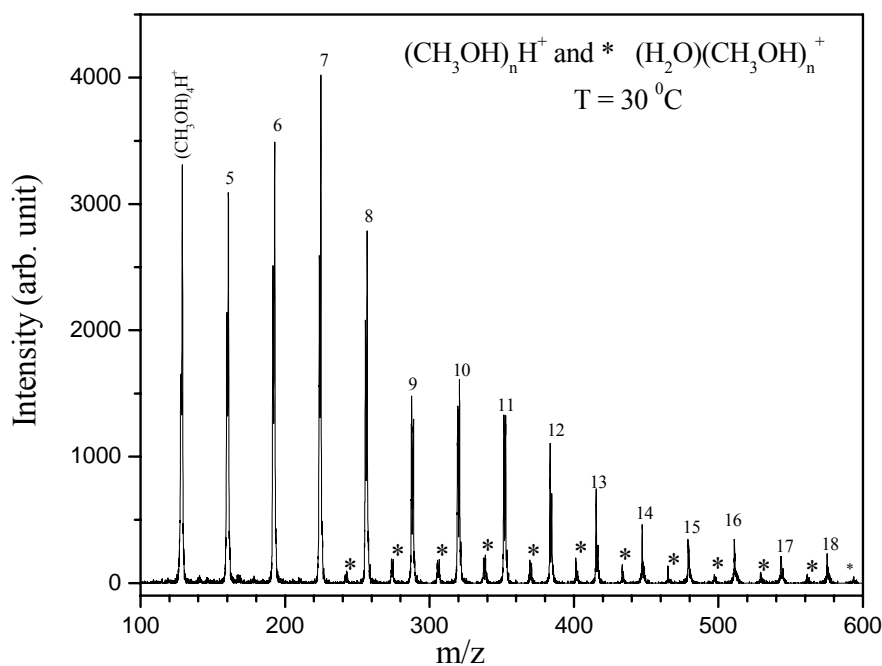
Figure 3: Typical methanol cluster ion mass spectrum by pulsed supersonic expansion of methanol vapor in helium. The neutral cluster beam was ionized by electron impact ionizer at the first quadrupole mass filter and detected after crossing the vacuumed drift cell and the second quadruple.
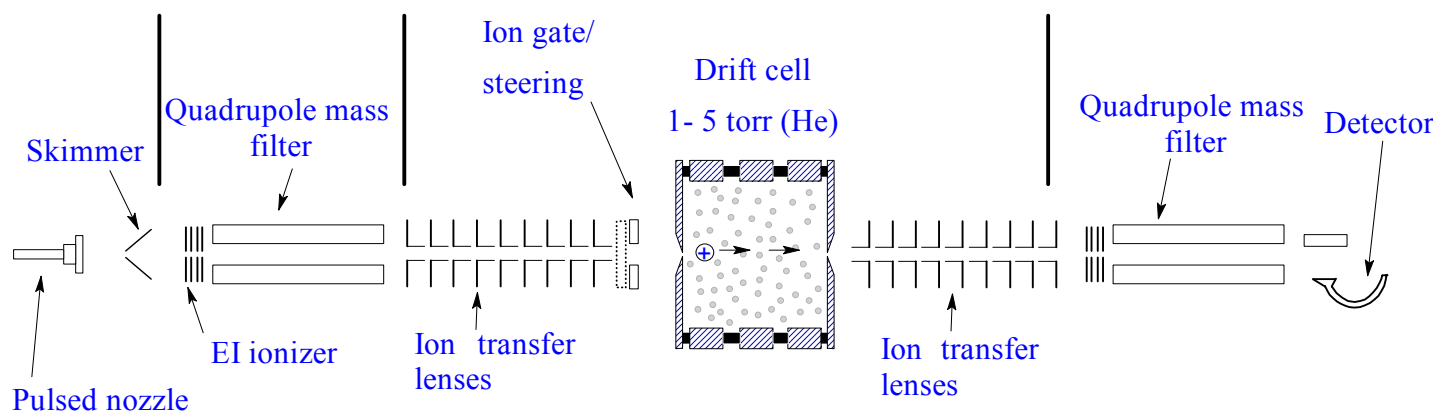
Figure 4: The ion mobility system can be divided into four sections for the expansion, the ionization, the reaction and the detection parts.
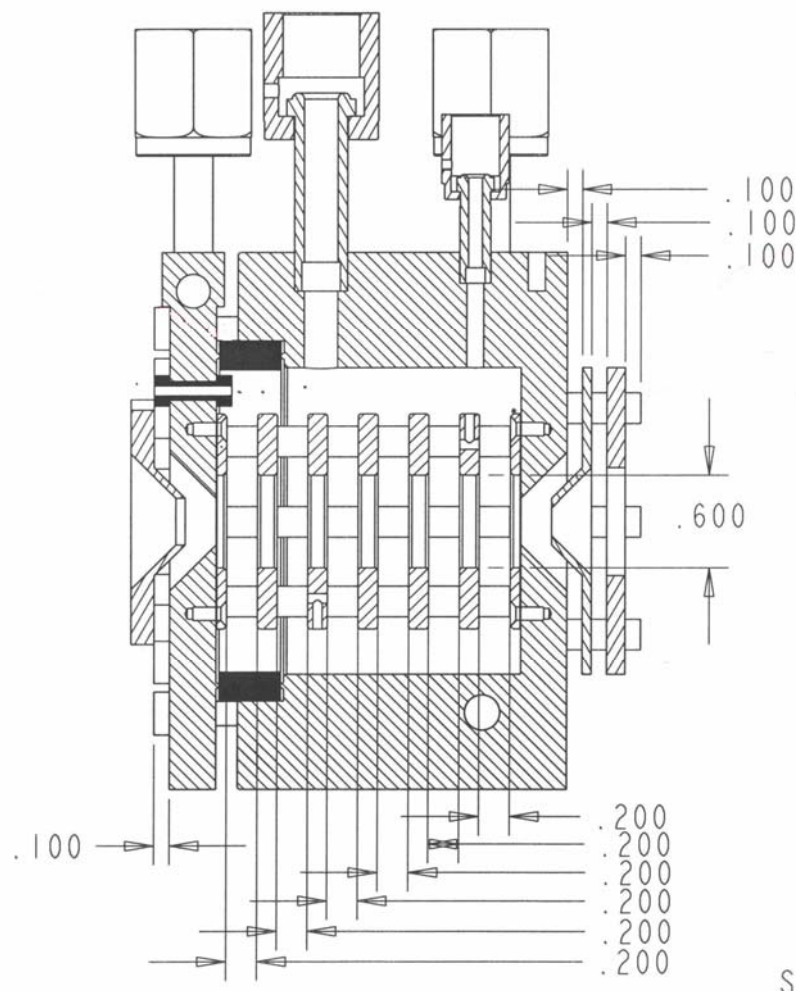
Figure 5: Schematic representation of the high temperature drift cell showing the five copper rings forming the cell with the separating ceramic spacers and the set of lenses before and after the cell section.
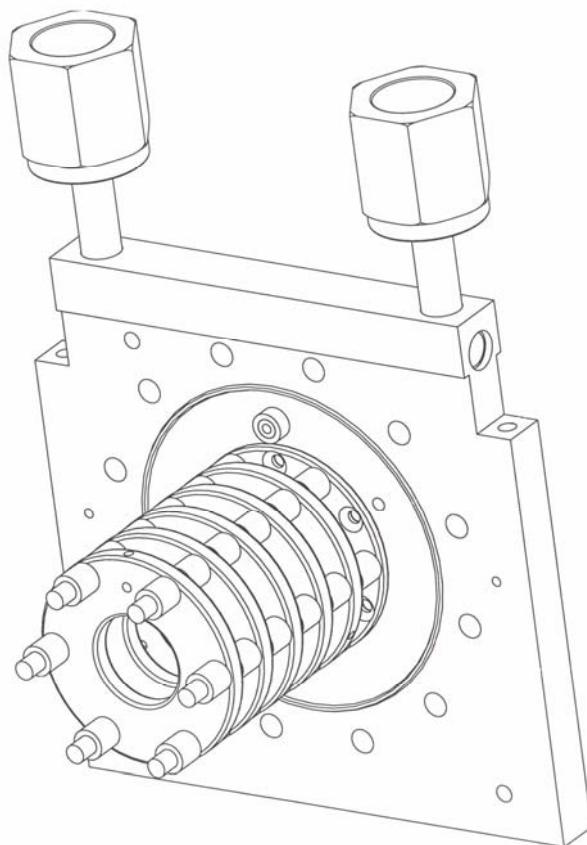
Figure 6: Five copper rings forming the high temperature cell are mounted in to an end cap plate which has its own inlet and outlet on the cooling liquid nitrogen.
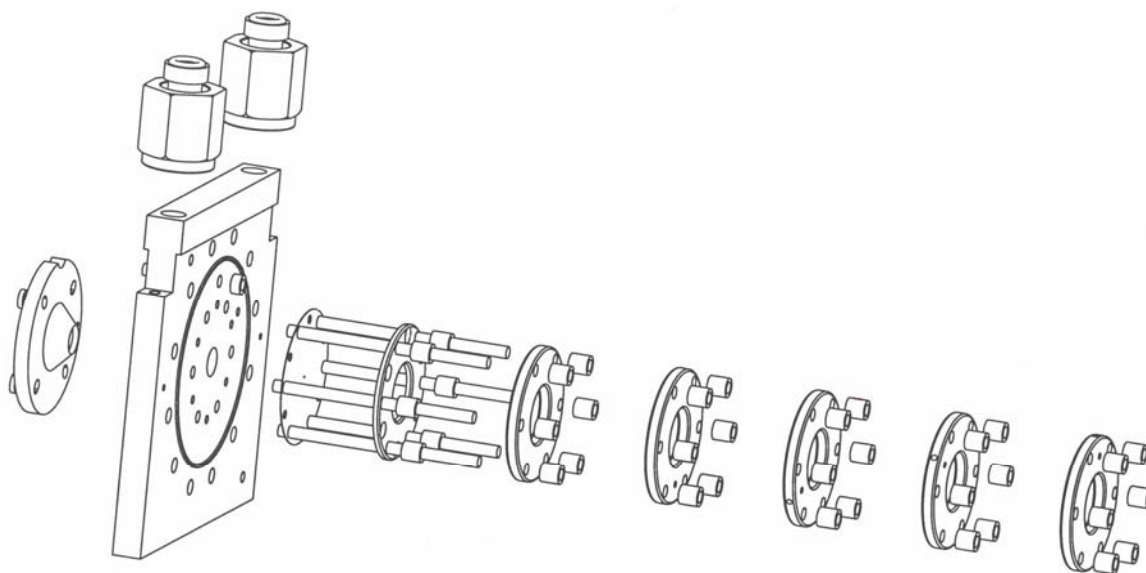
Figure 7: This is a simplified view for the mounting of the copper rings, the ceramic spacers and the trapping lens to the end cap.

2.6 Measurements

2.6.1 Thermochemistry and equilibrium measurements

The gas phase chemistry of ion-molecule reactions is better studied with the ion mobility drift cell compared to high pressure mass spectrometry (HPMS)[35]. One of the major advantages of the ion mobility drift cell is the generation of ions outside the drift cell, which can eliminate the formation of undesirable products through a charge transfer reaction. The mass selection of the ions prior to their injection into the cell makes the studied system cleaner and avoids the presence of simultaneous reactions and products inside the drift cell.

In the equilibrium measurements, the neutral molecular beam generated by the supersonic adiabatic expansion of water vapor (in the current work) (HPLC Aldrich grade) is ionized by the EI ionizer located coaxially before the first quadrupole mass filter, where the first stage of mass selection of the ion of interest will take place (H_3O^+ in the current work). The mass selected ions will be injected (in 5-15 ms pulses) into the drift cell filled with a known concentration of reactant pure gas (H_2) or in some other cases a mixture of a reactant gas and He where the partial pressures are well known . The drift cell pressure is maintained constant by the use of flow controllers (MKS no.1479A) and the cell temperature can be varied from 80 to 550 K and is controlled by K-type thermocouples and maintained constant within ±1 K. Cooling is done by flowing liquid nitrogen through copper tubes surrounding the drift cell and the heating is achieved by heaters located inside the drift cell rings. The injected ions lose their excess energy at the entrance of the cell by collisions with the gas molecules escaping from the drift cell

orifice. After many collisions, an equilibrium will be quickly established between the injected ions and the neutral molecules (H_2) inside the cell. The arrival time distributions ATDs of H_3O^+ and the formed adduct $(H_3O.H_2)^+$ are collected after the second stage of mass selection achieved by the second quadrupole mass spectrometer.

The clustering reaction is:

$$(H_3O^+)(H_2)_{n-1} + H_2 \Leftrightarrow (H_3O^+)(H_2)_n \qquad (2)$$
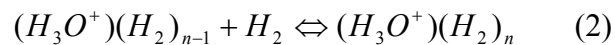
The rate constant of the reaction is:

$$k = \frac{[(H_3O^+)(H_2)_n]}{[(H_3O^+)(H_2)_{n-1}] \times p(H_2)} \qquad (3)$$

Where p (H_2) is the pressure of the Hydrogen gas inside the drift cell, $[(H_3O^+)(H_2)_n]$ and $[(H_3O^+)(H_2)_{n-1}]$ are the concentrations of the product and reactant ions.

From general chemistry concepts we know:

$$\Delta G^o = \Delta H^o - T\Delta S^o$$
$$\Delta G^o = -RT \ln k \qquad (4), (5)$$

Where R is the molar gas constant.

Combining equation XX and XX together yields

$$-R \ln k = \frac{\Delta H^o}{T} - \Delta S^o \qquad (6)$$

The van't Hoff plot is a plot of $-R\ln k$ as a function of $1/T$ which is a straight line where the slope is the cluster binding energy and the intercept is the entropy of the reaction.

Experimentally, the rate constant of the reaction is measured from the ration of the intensity of the ATDs of the reactant and product ions which is proportional to their concentrations. The pressure is converted from Torr to atmosphere unit.

$$k = \frac{I_{[(H_3O^+)(H_2)_n]} \times 760}{I_{[(H_3O^+)(H_2)_{n-1}]} \times p_{(H_2)}} \qquad (7)$$
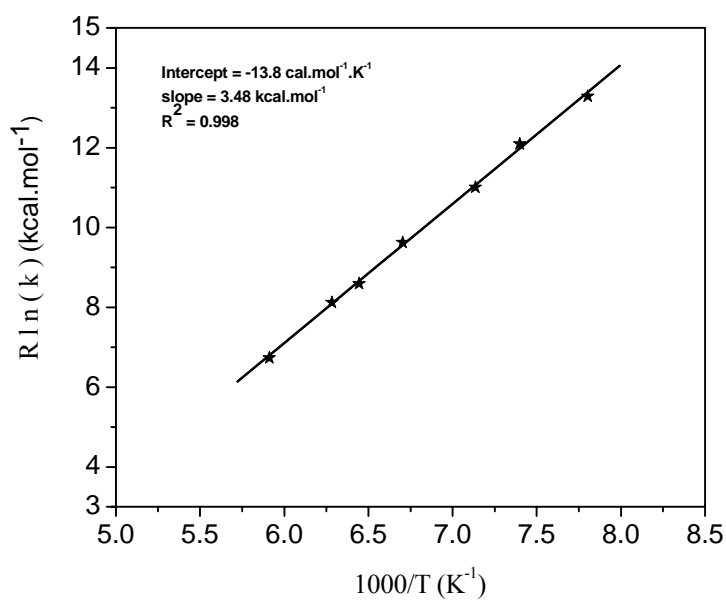
Figure 8: Example of van't Hoff plot showing the binding energy and the entropy of the first H_2 molecule on the H_3O^+ ion.

It is well established to check for the equilibrium conditions before starting to measure the rate constant of any clustering reaction. A good test of equilibrium comes from the identical ATDs of the reactant and product ions. If $(H_3O^+)(H_2)_{n-1}$ and $(H_3O^+)(H_2)_n$ ions are in equilibrium, then their ATDs must be identical and their apparent mobilities are equal. To check further that the equilibrium was achieved, at constant temperature and pressure, we varied the residence time of the ions inside the drift cell by varying the drift cell voltage until a constant ratio was obtained, as this is a good indication of equilibrium.

2.6.2 Mobility and structure investigation

The mobility K of a given ion, whether it is a single ionic chemical compound or an assembly of a certain number of molecules in a cluster, is a measure of its velocity across a drift cell filled with a non-reactive gas (He, Ar or N_2) under the influence of weak and uniform electric field. This mobility K expressed in $cm^2/V.s$ is defined as:

$$K = \frac{\vec{v_d}}{\vec{E}} \qquad (8)$$

Where $\vec{v_d} = \frac{z}{t_d}$ is the drift velocity (z is the drift cell length in cm and t_d is the drift time in s) and $\vec{E} = \frac{V}{z}$ (V is the drift voltage in Volt) is the electric field across the drift region. The mobility of this ion depends on its shape and structure. The smaller ions will have a higher mobility and the larger ones will have a lower mobility.

Since the mobility is related to the buffer gas density, it is conventional to scale the mobility to the calculated density at standard temperature and pressure, which will define the reduced mobility as:

$$K_o = \frac{P \times 273.15}{760 \times T} K \qquad (9)$$

Where P is the pressure in Torr and T is the temperature in Kelvin.

The 9 equation can be rearranged to give

$$t_d = \left(\frac{z^2 \times 273.15}{T \times 760 \times K_o} \right) \left(\frac{P}{V} \right) + t_o \qquad (10)$$

Where t_d is the ion drift time, the time spent by the ion inside the drift cell, and t_o is the time spend by the ion outside the drift cell, between the drift cell exit and the detector.

The plot of t_d as a function of P/V is straight line with slope α

where $\alpha = \left(\frac{z^2 \times 273.15}{T \times 760 \times K_o} \right)$ and the intercept is t_o.

Experimentally, ions are formed by EI ionization of the neutral molecular beam resulting from the supersonic adiabatic expansion. After a quadrupole mass-selection, ions of interest are injected into the drift cell in narrow pulses of 10-50 µs. The drift cell is filled with buffer gas (He) at a constant high pressure. The ions lose their excess energy (kinetic energy) and are thermalized by collision with the buffer gas molecules escaping from the drift cell. Their motion inside the drift cell is driven by two factors: they are accelerated by the weak electric field and decelerated by collisions with the buffer gas molecules. The second quadrupole is set to mass select the ion of interest

where its arrival time is collected as a function of time. The arrival time of the ions is taken at different drift cell voltages which correspond to different P/V values.

The mobility of a given molecular species can be theoretically calculated using a mobcal software designed and used by M. Bowers research group. This software can provide a calculated mobility using three different methods: the projection approximation (PA), the hard sphere (HS) and the trajectory method (TM).

To identify the structure, the experimental mobility will be compared to the calculated one and the collected arrival time distribution will be fitted to a theoretical ATD predicted by a transport equation.
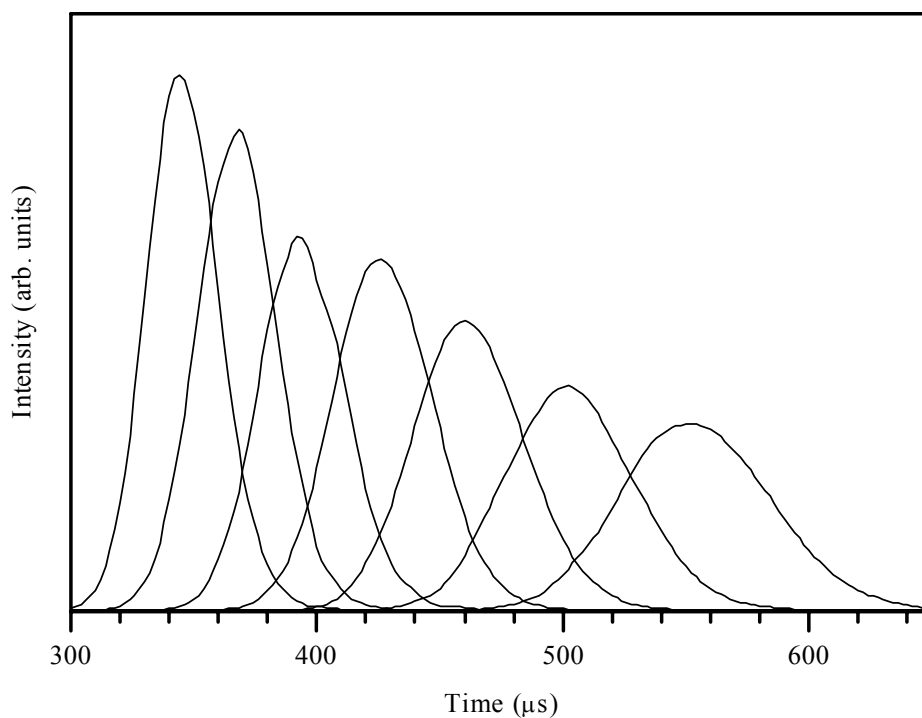
Figure 9: The arrival time distributions (ATDs) of injecting 10 μs $C_3H_3^+$ ion pulse into drift cell filled with 2.52 torr He at decreasing cell voltages of 3V steps. The earlier ATD corresponds to a drift voltage of 40 V while the later ATD corresponds to a drift voltage of 22V.
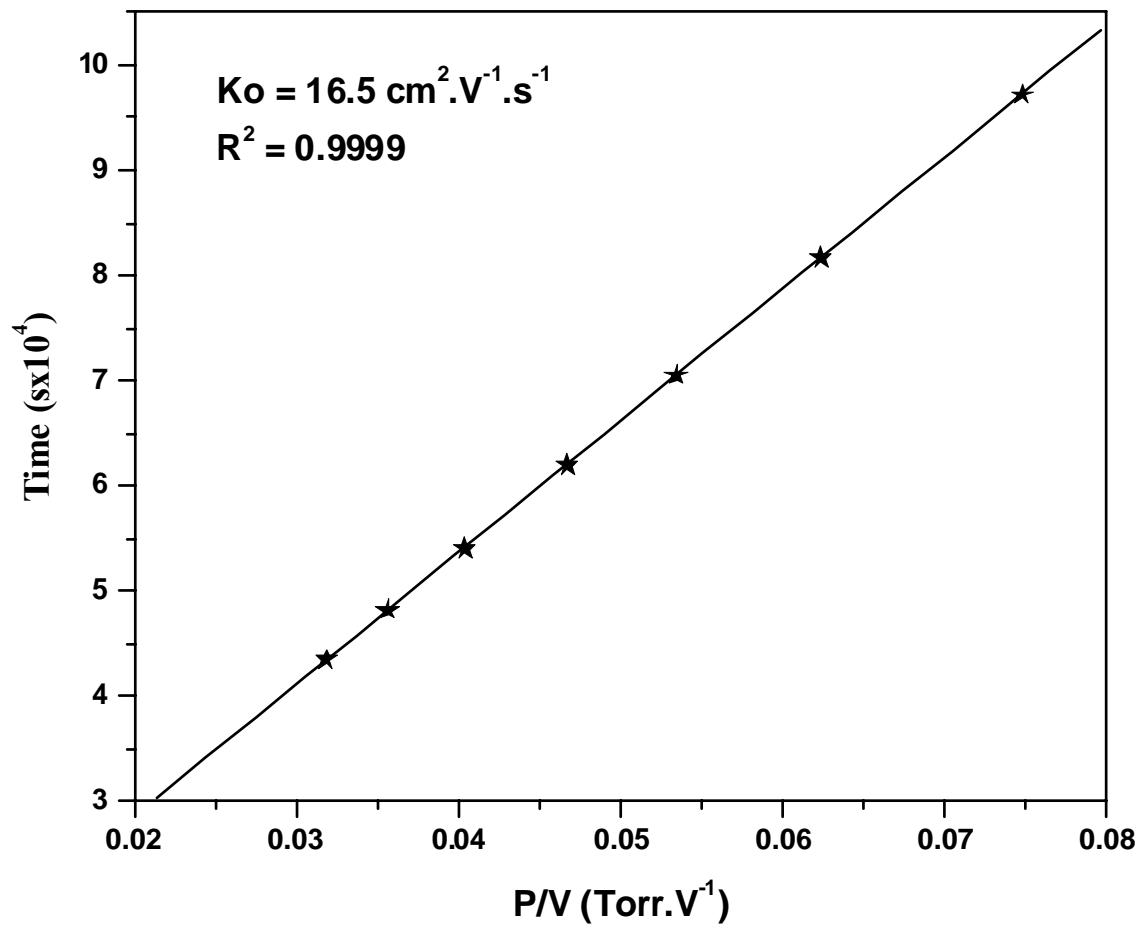
Figure 10: Plot of arrival time vs. P/V for the data in figure 9

2.6.3 Kinetics measurements

The ability to change the residence time of the injected ions inside the drift cell combined with the variable temperature and pressure makes the kinetics measurements of chemical reaction possible by the use of IM-MS technique.

For a proton transfer reaction, second order ion-molecule reaction

$$AH^+ + B \rightarrow A + BH^+ \qquad (11)$$

The rate constant of this reaction (k) is defined as

$$-\frac{d[AH^+]}{dt} = k[AH^+] \times [B] \qquad (12)$$

where $\dfrac{-d[AH^+]}{dt}$ is the rate of disappearance of AH^+, $[AH^+]$ and $[B]$ are the concentrations of AH^+ and B respectively.

The rearrangement and the integration of equation XX yields

$$-\ln \frac{[AH^+]}{[AH^+]_o} = k[B]t \qquad (13)$$

where $[AH^+]_o$ is the initial concentration of $AH^{\bullet+}$

Since the $[B] \gg [AH^+]$ (number of density of B is ten order on magnitude higher than AH^+) the reaction is pseudo-first order, and the pseudo-first order rate constant will be given by the plot of $-\ln \dfrac{[AH^+]}{[AH^+]_o}$ as a function of t the ions drift time.

Measuring the rate constant of the reaction at different cell temperature make the Arrhenius parameters accessible.

$$\ln(k) = \ln(A) - \frac{Ea}{RT} \qquad (14)$$

The plot of ln(k) as a function of 1/T is a straight line. The activation energy can be extracted from the slope and ln(A) is the intercept.

CHAPTER 3: Hydrophobic hydration of organic ions

3.1 Introduction

The hydrophobic hydration of organic molecular ions in the gas phase can reveal some important information: the strength of the ion-water interactions and the changes that can occur to the water hydrogen bond network. In some cases, the presence of water molecules around the ion can lead to its deprotonation to form protonated water clusters. The ion then becomes a radical which can initiate radical polymerizations. This information is useful in much area such as biological studies, interstellar chemistry, polymer chemistry, and atmospheric chemistry.

Cyclic $C_3H_3^+$ is an aromatic ion; in fact, it is the smallest cyclic aromatic species. Correspondingly, c-$C_3H_3^+$ is stable and unreactive. This ion and its linear isomers are common in environments where hydrocarbons are ionized, such as in electron impact mass spectra,[3] and presumably present in the hydrocarbon-containing ionospheres of Jovian planets[4] and Titan,[5] and in interstellar clouds.

Ions interact in these environments and in solution with polar molecules and solvents. The binding energies of the solvent molecules in the inner shell of the hydrocarbon ions can be measured using gas-phase clustering equilibria.[6, 36, 37] For example, we investigated recently the interactions of ionized aromatics with solvent

molecules, including a detailed study of the benzene$^{\bullet+}$/water system, where we measured binding energies of up to eight solvent molecules.[6, 36]

In addition to building up clusters, the solvent molecules can also react with the core ions by extracting a proton.[6,36,7,38] For example, we observed recently the deprotonation of benzene$^{\bullet+}$ by several H_2O molecules.[6,36] The rate coefficients of the deprotonation reaction displayed an unprecedented large negative temperature coefficient of $k = cT^{-67\pm4}$ (or an negative activation energy of -34 ± 1 kcal/mol). The deprotonation reaction is driven energetically by the formation of $(H_2O)_nH^+$ clusters that contain strong ionic hydrogen bonds (IHBs). Proton transfer driven by the association of several molecules through exothermic bond formation may be called associative proton transfer (APT) reactions. The energetic role of forming new IHB networks is supported by the fact that molecules that cannot form strong IHB networks such as CH_3CN do not deprotonate the benzene$^{\bullet+}$ ions.[9]

Distonic ions are radical ions that contain a protonated heteroatom, and a separate radical site. Distonic isomers are formally related to conventional cations by an H atom shift $H\text{-}CRX^{\bullet+} \rightarrow {}^{\bullet}CRX\text{-}H^+$ to a heteroatom. The distonic ions can be reaction intermediates, [39,40] or stable isomers[41-43]. Distonic ions can be characterized by their collisional dissociation and by neutralization - reionization,[44-53] and by distinctive ion-molecule reactions[42,53-41, 54-56] Relevant to the present study, N-protonated distonic structures were reported in ionized pyridine itself[7,8] and in ionized pyridine derivatives.[46, 57-62] The reactions of distonic pyridine with several neutrals were studied under low-

pressure energetic CID conditions. In these systems the distonic ion extracts an O atom from water to form a C=O bond at the radical site, while the classical ion does not react.[46]

The protonated heteroatoms of distonic ions can participate in hydrogen bonding. Such hydrogen-bonded complexes can be intermediates in ion dissociation.[63-67] Distonic ions can also form stable complexes, such as $OHC^•=OH^+\cdot\cdot OH_2$,[68] $^•CH_2OH_2^+\cdot\cdot OH_2$,[69] and $^•CH_2OH_2^+\cdot\cdot O(H)CH_3$,[68] and $^•CH_2CH_2O(H)H^+\cdot\cdot O(H)CH_2CH_3$,[68] and such complexes can be identified, for example, by ligand exchange reactions.[53]

The energetic of these hydrogen bonds are known experimentally, but some authors compared them to bonds formed by protonated ions and applied proton affinity correlations[70,71] to estimate the bond strength.[68, 72,73,74] These estimates assume that a remote radical site affects neither the proton affinity at the heteroatom nor the hydrogen bond formed with a neutral ligand after the site is protonated. The first assumption is consistent with calculations that show that a remote radical site does not affect the proton affinity of a heteroatom.[75] However, the second assumption, concerning the effects of a remote radical site on hydrogen bonds of distonic ions were not investigated.

Radical ions, including distonic species, can also form hydrogen bonds with solvents in nature, for example, when ions are formed in ice that is doped with organics and subjected to ionizing radiation on interstellar dust grains.

To better understand the interactions of distonic ions with solvents, the thermochemistry of these interactions needs to be characterized. In the present work we apply equilibrium studies to study the solvation of distonic ions. Namely, we shall look at

the stepwise solvation of pyridine$^{\bullet+}$ and 2-F pyridine$^{\bullet+}$ by several H_2O molecules, and compare the thermochemistry with the solvation of other radical and even-electron ions.

3.2 The $C_3H_3^+$ cation system

3.2.1 Structure of the $C_3H_3^+$ cation

Benzene vapor (Aldrich, 99.9% purity) was expanded to form a neutral molecular beam, which was ionized by electron impact at 100 eV. The resulting $C_3H_3^+$ (m/z 39) fragment ions were mass selected and injected in 5-15 µs pulses, at energies of 5 – 20 eV, laboratory frame, into the drift cell.

The selected ion $C_3H_3^+$ resulting from the fragmentation of benzene ion can have a linear or cyclic structure. The linear ion can rearrange to form the cyclic (more stable) using the excess of energy gain from the EI ionization or by collisions with neutral molecules at the entrance of the drift cell.

A mobility study was needed to confirm the structure of the selected ion. For these experiments, He, (ultrahigh purity, Spectra Gases 99.999%) was used as the buffer gas. The mass spectrum, in Figure 12 collected at drift cell pressure of 2.5 Torr of pure He shows the presence of unique ion, $C_3H_3^+$ inside the drift cell.

The experimentally measured mobilities and collision cross-sections at different temperatures are compared to theoretical values obtained for both the linear and the cyclic structures of the $C_3H_3^+$ cation. The structures used in the theoretical calculations are presented in Figure 11, where the cyclic structure of the $C_3H_3^+$ ion (on top) shows three equivalent hydrogen atoms on the ion with a bond length of 1.079 Ǻ, separated by

an angle of 120 $^{\circ}$ and the C-C bond length is found to be 1.370 Å. On the other hand, the linear structure (underneath) has two different type of hydrogen atoms, one single H-atom bounded to a terminal carbon atom with a bond length of 1.078 Å and two H-atoms in the other terminal carbon atom with a longer bond length (1.092 Å), the C-C bonds are 1.348 and 1.232 Å.
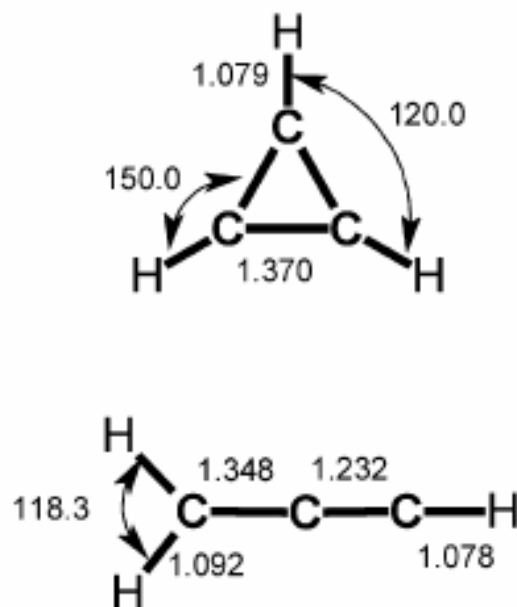
Figure 11: Optimized structures for the linear and cyclic $C_3H_3^+$ ion used in the theoretical investigations of the mobility.

Table 1: Summarized results for the measured and calculated mobilities and collision cross section for the $C_3H_3^+$ ion. Within the temperature range from 126 to 303 K, the experimental values are found to be closer and agree more with the theoretical cyclic structure of the $C_3H_3^+$ ion.

T (K)	K_o(Exp.)		$c\text{-}C_3H_3^+$		$l\text{-}C_3H_3^+$	
	K_o	$\Omega(\text{Å}^2)$	K_o	$\Omega(\text{Å}^2)$	K_o	$\Omega(\text{Å}^2)$
303	16.9	33.0	16.2	34.5	15.2	36.6
271	16.8	35.2	16.5	35.7	15.6	37.8
225	17.5	37.0	16.9	38.1	16.1	40.1
175	17.9	41.0	17.4	42.1	16.6	44.0
126	17.9	48.3	17.6	49.1	16.9	50.9

At the high temperature of 303 K, the experimentally measured mobility 16.9, is found to be closer to the calculated value for the cyclic structure 16.2 than the calculated one for the linear isomer 15.2. At low temperature, 126 K, the measured mobility,17.9, is in better agreement with the cyclic value (17.6) than the linear one (16.9). This agreement between the experimentally measured mobility and the calculated one for the cyclic structure is consistent at each temperature. The mobility study favors the presence of the cyclic structure inside the drift cell rather than the linear one.

To further investigate the structure of the selected $C_3H_3^+$ cation, we introduced a small amount 0.050 Torr of ethylene (C_2H_4) with 0.3 Torr of pure water vapor into the drift cell. If the linear isomer is present inside the drift cell it will react with the ethylene with a half-life time of about $4x 10^{-7}$ sec. under our conditions and the linear $C_3H_3^+$ cation will be totally converted to $C_5H_5^+$ as a final product, but our mass spectrum did not show the presence of $C_5H_5^+$(mass 65 amu).

The EI ionization of benzene can produce both the cyclic and linear isomers of $C_3H_3^+$, the enthalpy of formation of the linear is 282 kcal.mol^{-1}and the one for the cyclic is 257 kcal.mol^{-1}.The linear isomer can rearrange to form the more stable cyclic structure by the collision with the gas molecules escaping from the drift cell pinhole or by an excess of energy gained from the injection energy, which is higher than the rearrangement barrier of the linear ion to form the cyclic one.
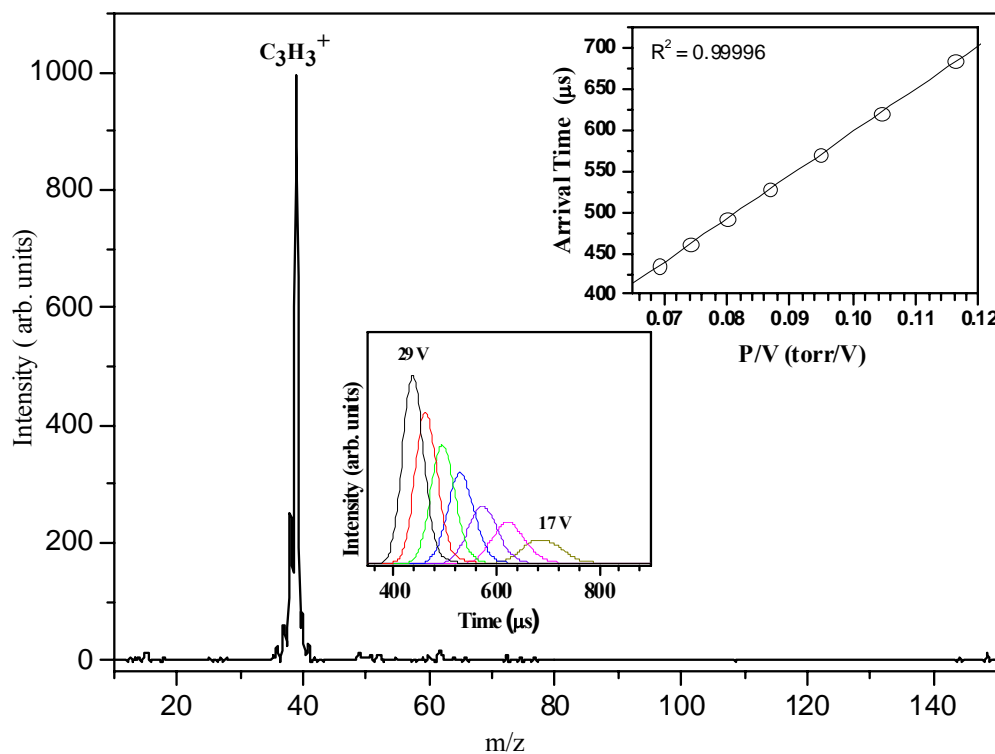
Figure 12: The collected mass spectrum showing the presence of unique $C_3H_3^+$ cation at a drift cell pressure of 2.5 Torr of He as a buffer gas at room temperature. In the center, a plot of the intensity of the ion as a function of the drift time is presented. In the upper corner, a plot of the arrival time of the $C_3H_3^+$ collected at different drift cell voltages as a function of P/V in Torr/Volt to measure the mobility.

3.2.2 Hydrophobic hydration of the $C_3H_3^+$ cation

3.2.2.1 Thermochemistry of the hydration of c-$C_3H_3^+$ ion

The $C_3H_3^+$ cation is injected into the drift cell containing 0.3 Torr of pure water vapor. By collisions with the water molecules escaping from the drift cell pinhole the mass selected ion is quickly thermalized. Upon many collisions inside the drift cell, equilibrium is quickly established between the reactant $C_3H_3^+$ cation and the products formed by addition of water molecules.

$$(C_3H_3)^+ . W_{n-1} + W \leftrightarrow (C_3H_3)^+ . W_n \qquad (1)$$
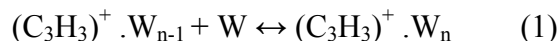
Products of reactions in the cell were identified by mass spectra presented in Figure 13 which is obtained through scanning a quadrupole mass filter after exit from the drift cell. The arrival time distributions (ATDs) of the reactant and product ions were collected by monitoring the intensity of each ion as a function of time. Equilibrium among the cluster ions of various sizes is demonstrated in Figure 14 through identical ATD peaks of the reactant ($C_3H_3^+$), and the products, $((C_3H_3^+)(H_2O)_n)$. To further test equilibrium we varied the residence time of the ions by applying drift fields of 1 – 4 V/cm inside the drift cell at 302 K and $P(H_2O) = 0.3$ Torr. Under these conditions the ion residence times varied between 0.4 and 3.0 ms. The observed equilibrium constants were independent of reaction time which further demonstrates that equilibrium was established during the observable reaction times.

Intensity ratio of ions in the association equilibria, $I[(C_3H_3^+)(H_2O)_n]/I[(C_3H_3^+)(H_2O)_{n-1}]$ was measured from the integrated peak areas of the

ATDs at the known temperatures and pressures. The equilibrium constants were obtained using Equation 1.

$$Keq = \frac{I\left[C_3H_3^+(H_2O)_n\right]}{I\left[C_3H_3^+(H_2O)_{n-1} \times P(H_2O)\right]} \qquad (1)$$

I is the intensity of the peaks taken from the ATDs and $P(H_2O)$ is the partial pressure of the water vapor inside the drift cell. All the equilibrium experiments were conducted at low drift cell fields of 1 V/cm and corresponding long residence times of 3 ms. The equilibrium constants measured as a function of temperature yield ΔH^o and ΔS^o from the slopes and intercepts of the van't Hoff plots. All of the results were replicated three or more times.

Collected mass spectra in Figure 13 following the injection of the $C_3H_3^+$ ion, show at high temperature (60 ^{o}C), the presence of two series of cluster ions. One corresponds to the clustering of water molecules on the $C_3H_3^+$ ion, $(C_3H_3^+)(W)_n$ where W = H_2O and n =1-2, and the other one is the protonated water clusters formed by deprotonation of the $C_3H_3^+$ ion, H^+W_n starting from n = 4. When the temperature is decreased to 30 ^{o}C, the intensity of the $C_3H_3^+$ reactant ion decreases and a peak relative to the addition of a third water molecule on the $C_3H_3^+$ ion appears and an increase in the protonated water clusters to reach $H^+(W)_6$. At the lowest temperature (18 ^{o}C), we observed the addition of six water molecules on the $C_3H_3^+$ ion and a jump in the protonated water cluster size. Unexpected cluster-like behavior was observed where the intensity for the $(C_3H_3^+)(H_2O)_4$ is found to be higher than the intensity of $(C_3H_3^+)(H_2O)_3$. This is accompanied by a sharp increase in the intensity of the protonated water clusters.
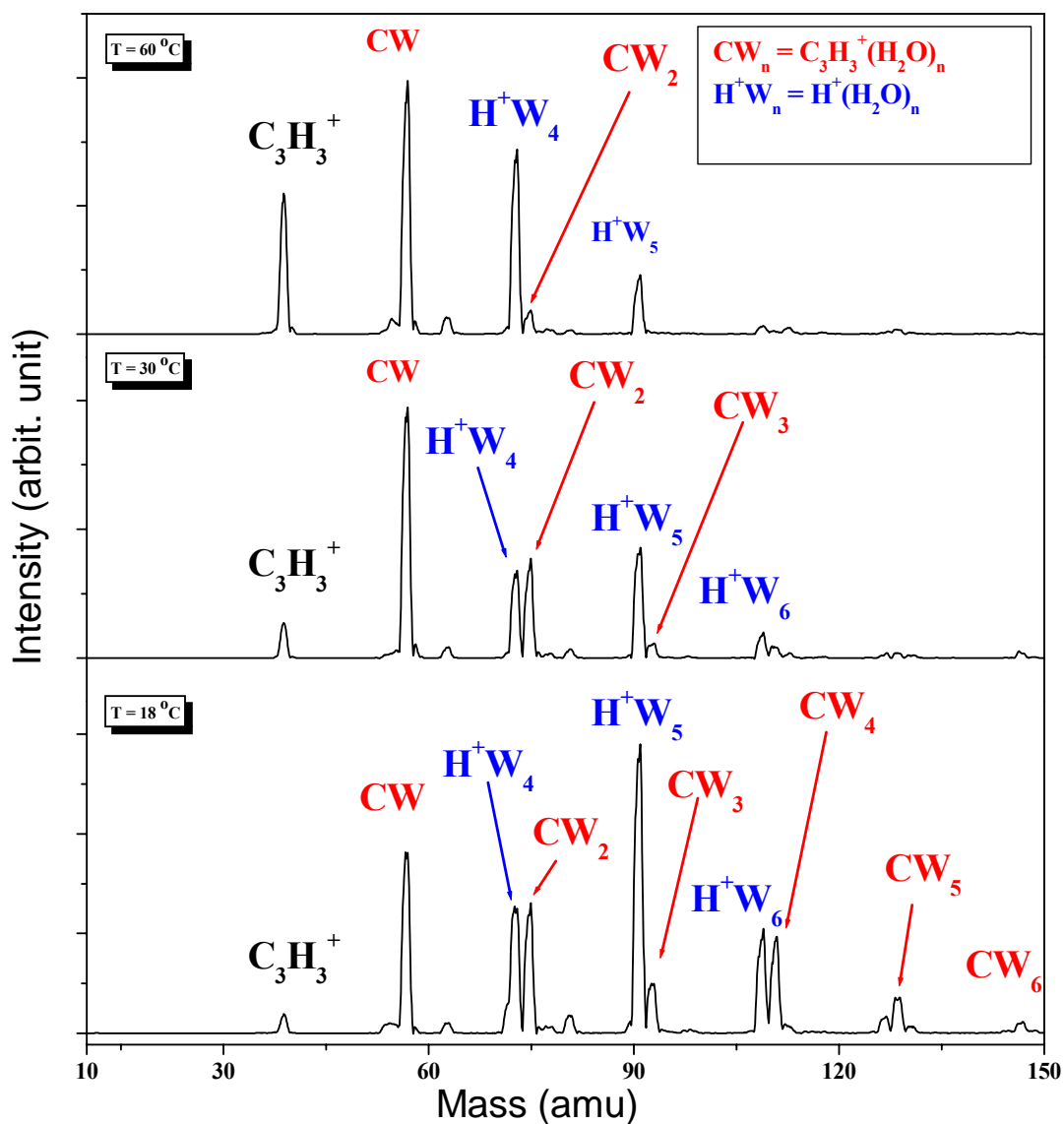
Figure 13: Mass spectra collected at different drift cell temperatures showing the stepwise clustering of water molecules on the $C_3H_3^+$ ion and the protonated water cluster ions. Notice at low temperature (18 ^{o}C), the unusual intensity of the $C_3H_3^{\bullet+}W_3$.

The equilibrium conditions of the stepwise hydration of the $C_3H_3^+$ are fulfilled and the equal ATDs of the $(C_3H_3^+)(H_2O)_n$ ions n = 0-5 is clearly observed in figure 14. The equal ATDs of multiple ions existing at the same time at a given temperature can confirm the presence of numerous equilibria taking place inside the drift cell. The addition of multiple water molecules to the ions happens simultaneously. Once the equilibria are established and confirmed, equilibrium constants are collected by measuring the intensities of each set of ions in equilibrium at a constant drift cell temperature and pressure. The drift cell pressure is held constant for all the measurement and the temperature is varied and controlled to within ± 1 K. At each increment of temperature an equilibrium constant is collected and the van't Hoff plots are generated (Figure15) for the sequential clustering of water molecules on the $C_3H_3^+$ ion. The binding energies of the stepwise clustering of water molecules around the $C_3H_3^+$ cation are measured for up to five from the slopes of the van't Hoff plots. The entropies of the reactions are given by the intercept. The experimental results are summarized in Table 2.

Table 2: Measured binding energy for the hydrophobic hydration of the $C_3H_3^+$ cation.

n	ΔH^o (Exp.) kcal.mol^{-1}	ΔS^o (Exp.) cal.mol^{-1}.K^{-1}	Binding Energy (Calc.) kcal.mol^{-1}
1	-11.7	-18.8	-11.9
2	-10.3	-17.2	-10.7
3	-8.5	-15.8	-9.7
4	-12.3	-25.0	-9.2
5	-10.0	-19.6	_

The measured binding energies of the stepwise clustering of water molecules on the $C_3H_3^+$ can be divided in two branches. The first branch includes the formation of hydrogen bonds between the first three water molecules and each of the equivalent hydrogen atoms of the $C_3H_3^+$ ion. The typical bond strength of such a system $CH^{\delta+\cdots}OH_2$ is about -10 kcal.mol^{-1} [76-79]. The binding energy in this system is to some extent higher by few kcal.mol^{-1} than the one found in the benzene-water system and this can be attributed to the higher charge density on the $C_3H_3^+$ ion as compared to $C_6H_6^{\bullet+}$ The second branch will include the higher cluster of water molecules around the $C_3H_3^+$ ion for $n \geq 4$. The bond strength and the binding energy values for clusters with $n \geq 4$ are found to be similar to the 8-10 kcal.mol^{-1} measured in large hydrated clusters[76]. Therefore, the $C_3H_3^+(H_2O)_n$ $n = 2$ and 3 can have isomers of comparable energies with direct bonds to the core ion as an internal solvation and with the outer shell water-water bonds as an external shell. These isomers may be in equilibrium in the observed populations, as observed in other cluster systems.[76]
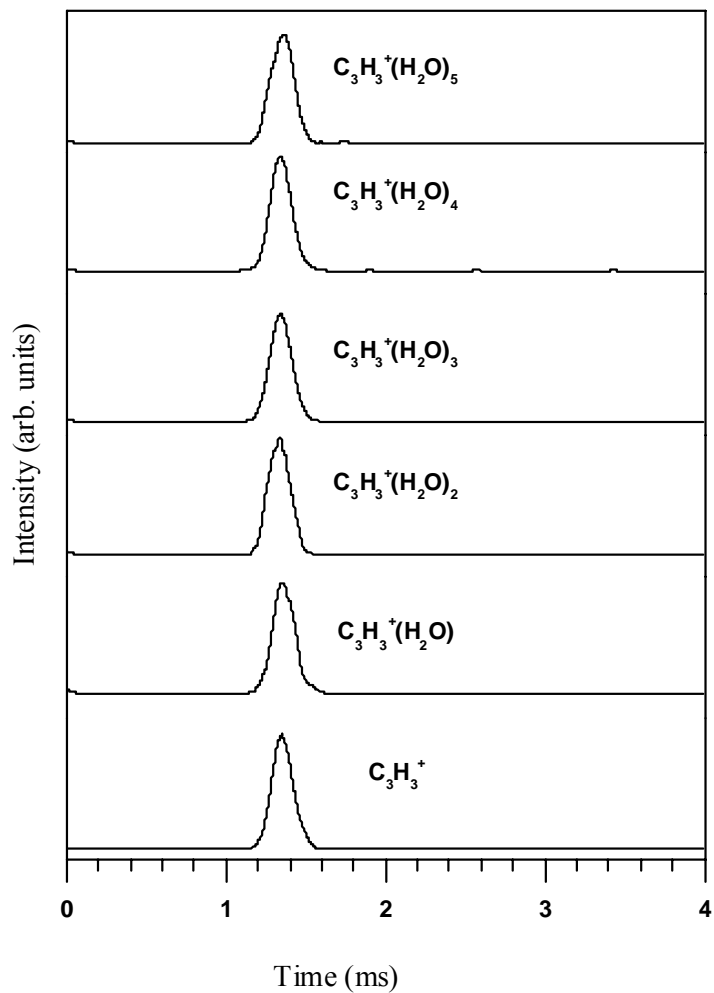
Figure 14: ATDs of the $C_3H_3^+$ ion and the $(C_3H_3^+)(H_2O)n$, where n = 1-5 product ions of the reaction of $C_3H_3^+$ with water molecules inside the drift cell at 18 ^{o}C and 0.3 Torr of pressure.

3.2.3 Structures and calculated energies for the hydration of c-$C_3H_3^+$

Calculated structures for the $C_3H_3^+(H_2O)_n$ are obtained using the ab initio calculations at the MP2/6-31+G** level along with their energies to the most stable isomer of each cluster. The achieved structures are presented in figure 16.

The clustering of the first water molecule on the $C_3H_3^+$ ion shows the presence of two isomers: 1a and 1-b. The isomer 1-a has the hydrogen bond aligned between the oxygen atom of the water molecule and the hydrogen atom of the $C_3H_3^{•+}$. This isomer is found to be more stable than isomer 1-b by 0.74 kcal/mol. The hydrogen bond length in isomer 1-a is 1.851 Å lower than the 2.557 Å bond length of isomer 1-b. For the addition of the second water molecule on the $C_3H_3^+$ ion, the calculations show the formation of four possible isomers, isomer 2-a is the most stable one. In this isomer the second water molecule attacks one of the remaining two hydrogen atoms of the $C_3H_3^+$ ion in a similar way to the first hydrogen bond, The bond lengths in isomer 2-a (1.890 Å) are found to be slightly higher than that in isomer 1-a. This can be attributed to the dispersion of the charge up to the presence of the second water molecule. Isomer 2-b is less stable than 2-a by 0.46 kcal/mol. We notice in this isomer interactions between each of the water molecules and the $C_3H_3^+$ and also appearance of water-water hydrogen bond formation. In isomer 2-c the two water molecules are bonded together by hydrogen bonds and only one of them forms a hydrogen bond with the $C_3H_3^+$ ion. The least stable isomer is 2-d where both water molecules attack the $C_3H_3^+$ ion from one C-H site. One H_2O molecule is bonded to the carbon atom and the other is bonded to the hydrogen atom. The two water molecules formed a water-water hydrogen bond between each other.

The clustering of three water molecules on the $C_3H_3^+$ ion is expected to lead to the formation of the first solvation shell where the three water molecules form three hydrogen bonds with the hydrogen atoms of the $C_3H_3^+$ ion. However the calculations show the formation of seven possible isomers, the solvated ion (isomer 3-d) is not the most stable one. The stability is retrieved in isomer 3-a where the three water molecules form a cyclic trimer structure by hydrogen bonds and the interaction is between the $C_3H_3^+$ and the formed cyclic trimer. This structure is clearly different from the classical ion solvation structure where the addition of the third water molecule induces the rearrangement of the water molecules to form a cyclic structure. The water-water interactions within the cycle structure can give more stability to the formed $C_3H_3^+(H_2O)_3$ compared to the classical ion solvation (isomer3-d) where three independent hydrogen bonds are formed. Isomer 3-b is more stable than isomer 3-d by 1.2 kcal/mol. Nevertheless, the three water molecules are not forming a cyclic structure but the presence of the water-water interactions can be the origin of this stability. The isomer, 3-c contains the water-water interactions and water-$C_3H_3^+$ interactions, but it still shows a small stability compared to isomer 3-d. Finally isomers 3-e, 3-f and 3-g are the least stable and their energies are higher than the most stable isomer 3-a by 2.66, 3.39 and 4.70 kcal/mol respectively. For the hydration of the $C_3H_3^+$ by four water molecules, six isomers are presented. Isomer 4-a, where the four water molecules form a well known tetramer cyclic structure[80, 81] is mainly the stable one. In this isomer (4-a) the four water molecules are connected together by hydrogen bonds forming a quadratic cyclic structure which will interact with the $C_3H_3^+$ ion by formation of two hydrogen bonds with diagonal

oxygen atoms. In isomer 4-b, the four water molecules formed a trimer cyclic structure bonded to one water molecule by water-water hydrogen bond. Their interactions with the $C_3H_3^+$ ion formed the second stable isomer with an increased energy by 2.22 kcal/mol as compared to isomer 4-a. The addition of one water molecule to the classically solvated ion seen in structure 3-d by water-water hydrogen bond from the second solvation shell is found to be the third lowest in energy (4-c). When the water-water interactions are reduced in isomer 4-c and the water molecules tend to form a second solvation shell the energy is increased by 5.00 kcal/mol compared to isomer 4-a. Isomers 4-d, 4-e and 4-f are higher in energy by 5-9 kcal/mol relative to isomer 4-a. It is noteworthy that the formation of cyclic water structures with three or four water molecules forms the most stable cluster isomers with the $C_3H_3^+$ ion. The tendency of the water molecules to form cyclic structure in the presence of the c-$C_3H_3^+$ ion is consistent with the structural behavior of neutral water clusters[80, 81].

Figure 16, includes the lowest energy clusters formed by the hydration of the c-$C_3H_3^+$ ion by up to four water molecules. In all the formed cluster ions, $C_3H_3^+(H_2O)_n$, n = 1-4 more than 90 % of the total charge is localized on the core ion. The partial charges on the hydrogen atoms of the $C_3H_3^+$ ion (around 0.3 C) are not awfully disturbed by the clustering of water molecules. In the presence of cyclic water structures, the interactions between the $C_3H_3^+$ ion and these cyclic structures are achieved by stretched hydrogen bonds of more than 2 Å which is found to be longer the one observed with one and two water molecules on the $C_3H_3^+$ ion (1.8 Å). The theoretical calculations of the binding energies for the water molecules on the $C_3H_3^+$ ion and the $CH^{...}OH_2$ bond lengths are

conducted at three different levels. The calculated vales with the BSSE corrections and the experimental ones are presented in Table 3. For the addition of 1, 2 and 3 water molecules the calculated binding energies are in good agreement with the experimentally measured values. However, it is clear that the interatomic distance between the oxygen atom of the water molecule and the hydrogen atom of the $C_3H_3^+$ ion in the $C_3H_3^+(H_2O)$ is highly sensitive to the degree of electronic correlations as shown in Table 3. The lowest energy structures presented in figure 16 and figure 17, obtained with full geometry optimizations at the MP2/6-31+G** level, are expected to capture most of the electronic correlation as shown in Table 3. The BSSEs are calculated in cases where the addition of a water molecule to the lowest energy isomer of the (n-1) cluster results, after geometry optimization, in the lowest energy isomer of the (n) cluster. For the $C_3H_3^+(H_2O)_4$ cluster the addition of the fourth water molecule to the lowest energy isomer (3-a) does not produce the lowest energy structure of the $C_3H_3^+(H_2O)_4$ cluster (4-a). Therefore, the binding energy calculated on the basis of the lowest energy isomer of the $C_3H_3^+(H_2O)_4$ cluster (11.99 kcal/mol at the MP2/6-31+G** level in comparison with the experimental value 12.3 kcal/mol) does not include the BSSE correction. It should be noted that the presence of several isomers with comparable energies and many different connecting pathways makes the calculations of the BSSEs. Therefore, the corrected binding energies are uncertain for the large clusters. However, it should be clear that the measured binding energies in these systems may reflect an average of several possible structural isomers with comparable energies.

Table 3: Calculated and experimental binding energies of the hydration of the $C_3H_3^+$ ion at three different levels, and the $CH^{\cdots}OH_2$ bond length in angstroms.

n	MP2//ROHF/ 6-31+G**[b]	B3LYP/ 6-31+G**[c]	MP2/ 6-31+G**[d]	Experimental Values
1	11.95 (13.71)	12.70 (13.60)	11.83 (13.78)	11.70
2	10.74 (12.47)	10.91 (11.81)	10.51 (12.46)	10.30
3	9.67 (11.41)	9.21 (10.14)	(10.61)	8.50
4	(10.20)	(9.05)	(11.99)	12.30
$CH\ldots OH_2$ (Å)	1.946	1.806	1.851	

[a] the values between brackets do not include BSSE; only ZPVE is included.

[b] MP2 energies on the optimized ROHF/6-31+G(d,p) structures.

[c] optimized at the B3LYP/6-31+G** level

[d] optimized at the MP2/6-31+G** level.
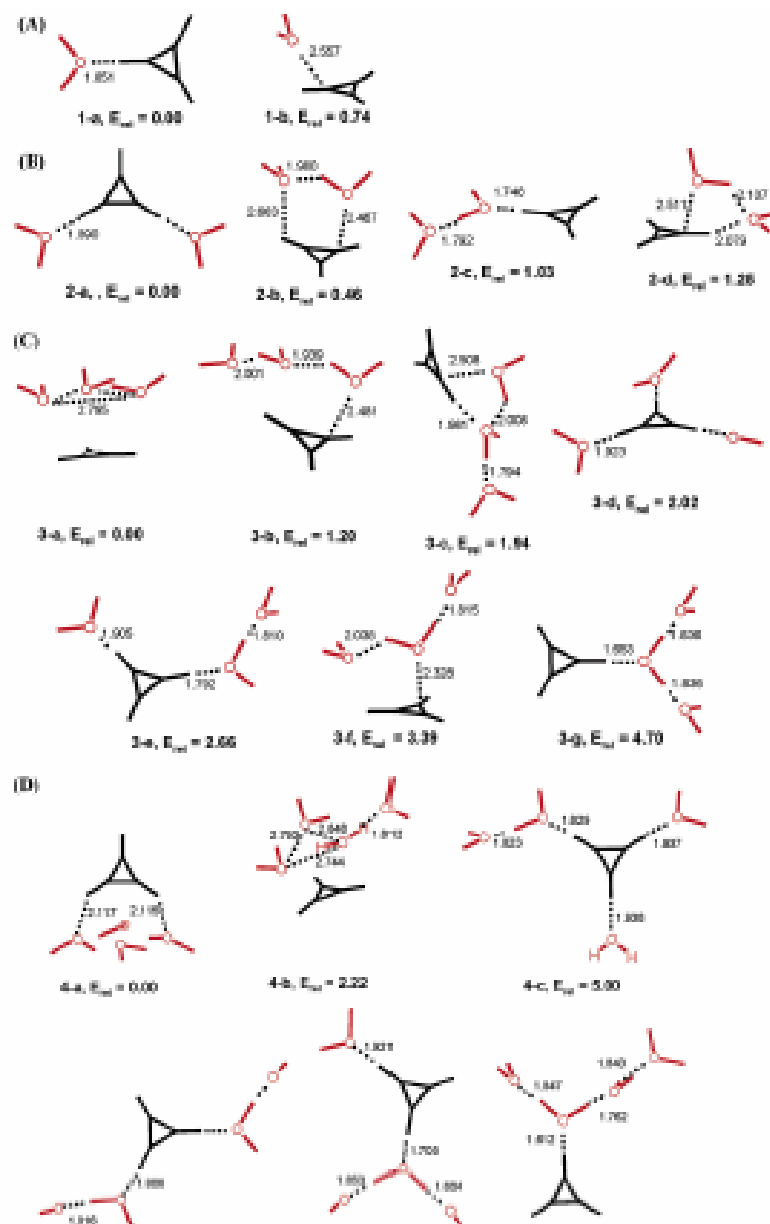
Figure 15: Section A and B presents the isomeric structures of the clustering of one and two water molecules calculated at the MP2/6-31+G** level. The calculated structures for the isomers of $C_3H_3^+(H_2O)_3$ and $C_3H_3^+(H_2O)_4$ are presented in sections C and D at the same calculation level. E_{ref} is the energy in kcal/mol relative to the most stable isomer in each n. The bond lengths are expressed in angstroms (Å).
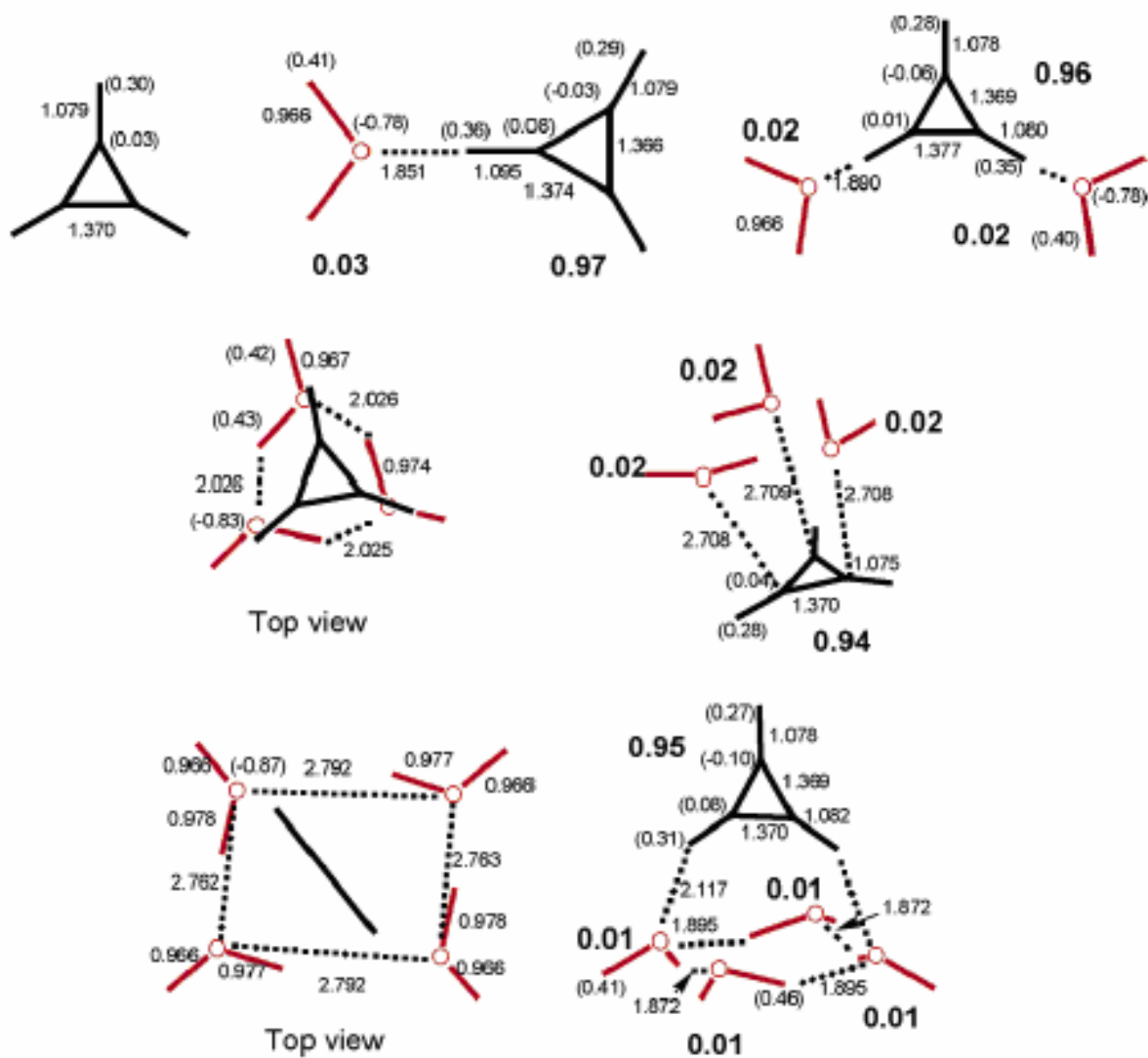
Figure 16: Lowest energy isomers of the c-$C_3H_3^+$ ion and the c-$C_3H_3^+(H_2O)n$, n = 1-4 clusters calculated at the MP2/6-31+G** level. The bond lengths are in angstroms (Å), the atomic charges are in parentheses and the molecular charges are in bold.

3.2.4 Kinetics and energetics of the deprotonation of the c-$C_3H_3^+$

The collected mass spectra, in figure 13, shows that the intensity of the protonated water clusters $H^+(H_2O)_n$ is increased at low temperature (18 ^oC). At the same time, irregularity is observed in the $C_3H_3^+(H_2O)_n$, by a decrease in the intensity of the $C_3H_3^+(H_2O)_3$ and unexpected increase in the intensity of $C_3H_3^+(H_2O)_4$. The protonated water clusters $H^+(H_2O)_n$ are formed from the $C_3H_3^+(H_2O)_n$ clusters by an associative proton transfer (APT) reactions similar to these reactions.

$$C_3H_3^+ + nH_2O \rightarrow (H_2O)_nH^+ + C_3H_2^\bullet \qquad (2)$$
$$C_3H_3^+(H_2O)_{n-1} + H_2O \rightarrow (H_2O)_nH^+ + C_3H_2^\bullet \qquad (3)$$
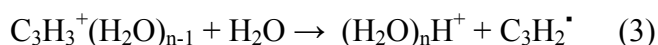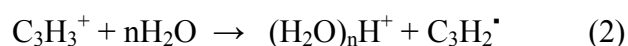
Both reactions (2) and (3) can direct to the formation of the protonated water clusters $(H_2O)_nH^+$ and they are both endothermic for small n. They become exothermic at sufficiently large n due to the stability of the formed product, the protonated water clusters. In fact, the energetics of reaction (3) turns from endothermic into approximately thermoneutral at n = 4 corresponding to the $C_3H_3^+(H_2O)_3$ reactant. Actually, the weak minimum observed at $C_3H_3^+(H_2O)_3$ can be explained by a depletion of the total amount of $C_3H_3^+(H_2O)_3$. The $C_3H_3^+(H_2O)_3$ add one water molecule to form the higher cluster $C_3H_3^+(H_2O)_4$ with the equilibrium process. The same $C_3H_3^+(H_2O)_3$ is deprotonated to form the protonated water clusters $(H_2O)_nH^+$ by APT reaction. The identical ATDs in figure 14 confirm that equilibrium is established between the reactant $C_3H_3^+(H_2O)_3$ and

the product $C_3H_3^+(H_2O)_4$ and it is not affected by the APT reaction taking place at the same time.

Experimentally, the mass selected $C_3H_3^+$ ion is injected into the drift cell filled with pure water vapor and up to the high number of collisions between the ion and the water molecules product are formed inside the drift cell. The protonated water clusters are generated by the APT reaction from the $C_3H_3^+(H_2O)_n$ clusters therefore, the $C_3H_3^+(H_2O)_n$ clusters are the reactants and the protonated water clusters $H^+(H_2O)_n$ are the products as shown in reaction (3).

$$C_3H_3^+(H_2O)_{n-1} + H_2O \rightarrow (H_2O)_nH^+ + C_3H_2^\bullet \qquad (3)$$
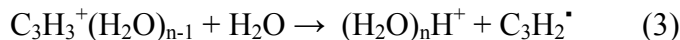
The rate of the disappearance of the $C_3H_3^+(H_2O)_{n-1}$ clusters can be expressed as:

$$\frac{d([C_3H_3^+(H_2O)_{n-1}])}{dt} = -[C_3H_3^+(H_2O)_{n-1}]\,k \qquad (3)$$

Where k is the rate constant of the pseudo-first-order reaction. A rearrangement and integration of both sides of the equation can give:

$$-\ln\left(\frac{[C_3H_3^+(H_2O)_{n-1}]}{[C_3H_3^+(H_2O)_{n-1}]_o}\right) = kt \qquad (3)$$

where t is the reaction time. In this experiment the reaction time is collected from the ATDs of the product ions.

Since the disappearance of the $C_3H_3^+(H_2O)_{n-1}$ clusters is proportional to the appearance of the protonated water clusters $H^+(H_2O)_n$ and the $[C_3H_3^+(H_2O)_{n-1}]_o$ is equal to the total amount, equation (4) can be rearranged to give:

$$-\ln\left(\frac{[H^+(H_2O)_n]}{[C_3H_3^+(H_2O)_{n-1}] + [H^+(H_2O)_n]}\right) = kt \qquad (4)$$

The reaction time t can be controlled by changing the drift cell voltage. The plot of the natural logarithm of the normalized ratio as a function of the reaction time t is a straight line and its slope gives the rate constant of the reaction k at that given temperature.

At each drift cell temperature, a rate constant can be collected and the activation energy (E_a) of the APT reaction can be derived from the Arrhenius equation:

$$k = A \exp(^{-E_a}\!/_{RT}) \qquad (5)$$

The rearrangement of the Arrhenius equation can give:

$$\ln(k) = \frac{-E_a}{R}\frac{1}{T} + \ln(A) \qquad (6)$$

The plot of ln(k) as a function of 1000/T is a straight line and its slope multiplied by - R (ideal gas constant) gives the APT activation energy in kcal.mol^{-1}. Ln(A) is given by the intercept

The experiments are conducted in a specific range of drift cell temperature where the APT is taking place. The time profile of the changes in the concentrations of the reactants $C_3H_3^+(H_2O)_{n-1}$ and products $H^+(H_2O)_n$ are shown in **Figure 17**. It is clear, from **Figure 17**, that the concentrations of the sum of the $C_3H_3^+(H_2O)_{n-1}$ clusters decay as the reaction time t is increased. On the other hand the concentration of the sum of the $H^+(H_2O)_n$ clusters is increased. The concentration-time profile is presented at two different temperatures (293 and 279 K).I It is significant that the decay of the reactants $C_3H_3^+(H_2O)_{n-1}$ is sharper at the lower temperature (279 K) where the APT reaction is faster, and the product concentration increase more rapidly at lower temperature. The rate

coefficients show a very large negative temperature coefficient, which may be obtained from the plot of ln(k) as a function of ln(T) in the exponential form as $k = cT^{-63\pm4}$ or as an Arrhenius activation energy of -37 ± 1 kcal.mol-1. This can be obtained from the Arrhenius plot in **Figure 17**.

Negative temperature coefficients were observed in bimolecular ion-molecule reactions, in hindered reactions and in association reactions. The observed temperature coefficients of $k = cT^{-2}$ or $k = cT^{-8}$ are due to competitive dissociation of the reaction complexes to product or back to reactonts.[46] However, the much larger temperature coefficients of the deprotonation reactions in the $C_3H_3^+$/water system may be attributed to a different source. In this case a many-body cluster $C_3H_3^+(H_2O)_n$, (n = 3) needs to be assembled first to make the deprotonation reaction (3) energetically possible. These clusters may be seen as the reactive fraction of the overall cluster population. This reactive fraction of the equilibrium cluster populations increases with decreasing temperature. The commutative enthalpy change for forming the $C_3H_3^+(H_2O)_n$ clusters is the sum of the reaction enthalpies of the first n steps, respectively. In the present system this enthalpy is – 30.5 kcal/mol for n = 3 and 43.0 kcal/mol for n = 4, in some range as the observed Arrhenius activation energy of – 37 kcal/mol. As to the energetics of the deprotonation reactions, we may consider the energetics of the overall reaction (2) or of the stepwise reaction (3) above. The energetics may be calculated from the proton affinities of H_2O (165 kcal mol[1]) and of the $c\text{-}C_3H_2^.$ radical (227 kcal mol^{-1})[82], the binding energies of the $(H_2O)_nH^+$ clusters of 32, 21, 18 and 13 kcal mol^{-1}, for n = 2-5 respectively[80] and, for reaction (3), the binding energies of the $C_3H_3^+(H_2O)_n$ clusters

(**Table 2**). For the overall reaction (2) we find, for deprotonation by n H_2O molecules, (n = 1 to 5) the ΔH^o values of 62, 30, 10, -7 and -20 kcal mol^{-1}. Therefore, the overall reaction becomes exothermic for deprotonation by 4 H_2O molecules. For the stepwise reaction (3) for deprotonation by a total of 1 – 5 H_2O (i.e., with n going from 1 to 5 in reaction (3), has ΔH^o values of 62, 41.7, 20.3, 1.5 and -7.7 kcal mol^{-1} respectively. Thus, this reaction becomes about thermoneutral at the deprotonation of the 3-fold solvated ion $C_3H_3^+(H_2O)_3$, and exothermic at the deprotonation of the 4-fold solvated ion $C_3H_3^+(H_2O)_4$.

The thermochemistry of the overall reaction (2) is relevant if the reaction proceeds effectively in one step, i.e., if the cluster assembles without stabilization, retaining the exothermicicty of all the association steps as internal energy for deprotonation/dissociation to form products. This is possible in the experiments that use neat water vapor, where collision with every successive H_2O molecule can lead to association with the release of the binding energy into internal energy, rather than removing energy from the cluster. However, if a third body is present, it would stabilize the growing cluster and no internal energy would be available for deprotonation/dissociation. In fact, we observed such a third-body effect in the Benzene$^{\bullet+}$/water system where the addition of He quenched deprotonation.[14]

The stepwise reaction (3) becomes near thermoneutral with deprotonation of the 3-fold solvated cluster by the fourth H_2O molecule, which is consistent with the observed results. An intermediate mechanism, where the incipient clusters are partially thermalized between steps is also possible.
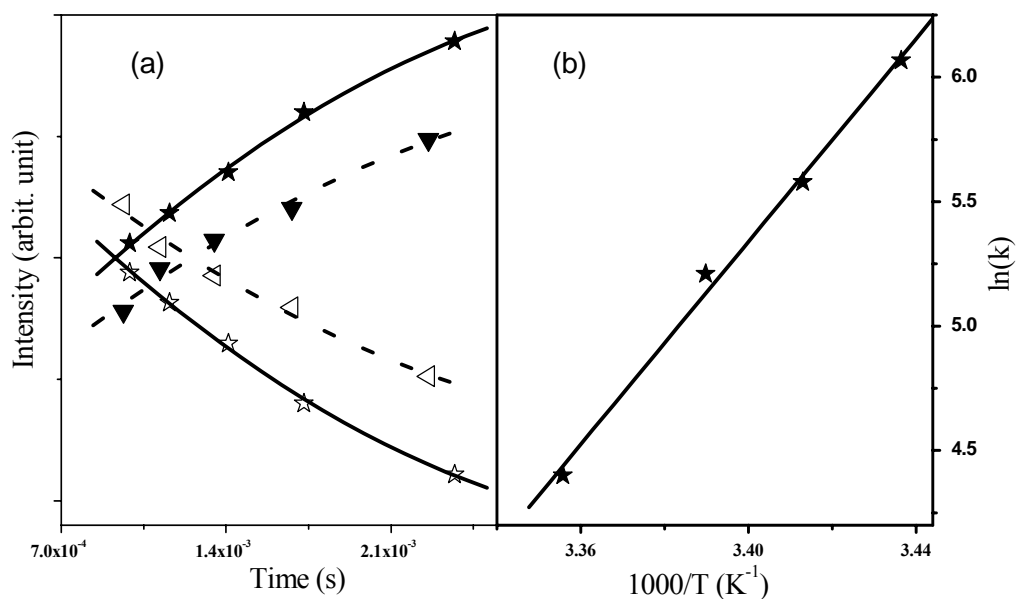
Figure 17: On the left side (part a): The stars (first solid line from top): normalized intensity of H^+W_n as a function of time at $T = 16\ ^oC$ and $P = 0.24$ Torr of pure water vapor. The triangles (second dashed line from the top): normalized intensity of H^+W_n as a function of time at $T = 20\ ^oC$ and $P = 0.24$ Torr of pure water vapor. The empty triangles (third dashed line from top): normalized intensity of $C_3H_3^+W_n$ as a function of time at $T = 20\ ^oC$ and $P = 0.24$ Torr of pure water vapor. The empty stars (last solid line from top): normalized intensity of $C_3H_3^+W_n$ as a function of time at $T = 16\ ^oC$ and $P = 0.24$ Torr of pure water vapor. On the right (part b) is an Arrhenius plot of $ln(k)$ as a function of $1000/T$.

3.2.5 Solvation of the c-C$_3$H$_3$$^+$ cation by acetonitrile molecules

The hydration of the c-C$_3$H$_3$$^+$ with water molecules result in the formation of extended hydrogen bond network, therefore, we observed the formation of stable trimer and tetramer cyclic water clusters interacting with the c-C$_3$H$_3$$^+$ and sometimes leading to its deprotonation via APT reactions. The solvation of the c-C$_3$H$_3$$^+$ by the nonprotic acetonitrile molecules can be interesting because of the lack of the formation of extended hydrogen bond network.

The mass spectra presented in figure 19, are collected at different temperatures after the injection of the c-C$_3$H$_3$$^+$ ion into the drift cell containing 0.1 Torr. of pure CH$_3$CN. It is clear that when the temperature is decreased the population of the c-C$_3$H$_3$$^+$(CH$_3$CN)$_n$ clusters is shifted in the direction of the higher clusters. The H$^+$(H$_2$O)(CH$_3$CN)$_3$ cluster ion demonstrates a remarkable enhanced stability at all temperatures. The equilibrium conditions for the reactions between the C$_3$H$_3$$^+$ ion and the CH$_3$CN molecules are confirmed and the equal ATDs of the product ions are presented in Figure 20a. The van't Hoff plots are generated for the addition of the first three CH$_3$CN molecules and they are displayed in Figure 20 b. The experimental binding energies of the CH$_3$CN molecules on the C$_3$H$_3$$^+$ are summarized in **Table 4**. The highly polar acetonitrile molecule (μ = 3.6 D) forms a stronger bond with the C$_3$H$_3$$^+$ ion (-15.1 kcal/mol) as compared to the one formed with water (-11.7 kcal/mol) and it takes 40.6 kcal/mol to solvate the C$_3$H$_3$$^+$ ion with three CH$_3$CN molecules when only 30.5 kcal/mol can do it with three water molecules. The first three acetonitrile molecules are attached to the core ion and forms the inner solvation shell by CH$^{\delta+\cdots}$N bonds. The outer shell

solvent molecules are formed by similar bonds but they are between the nitrogen atoms and the hydrogen atom of the methyl group. Typical strength for these bonds is about 8-10 kcal/mol and therefore, starting an outer shell with acetonitrile molecules does not show a significant thermochemical effect.

Table 4: Thermochemistry of the solvation equilibria of the $C_3H_3^+$ ion by CH_3CN.
$C_3H_3^+(CH_3CN)_{n-1} + CH_3CN \leftrightarrow C_3H_3^+(CH_3CN)_n$

n	ΔH^o (kcal/mol)	ΔS^o (cal.mol^{-1}.K^{-1})
1	-15.3	-21.5
2	-13.3	-18.2
3	-12.0	-21.6
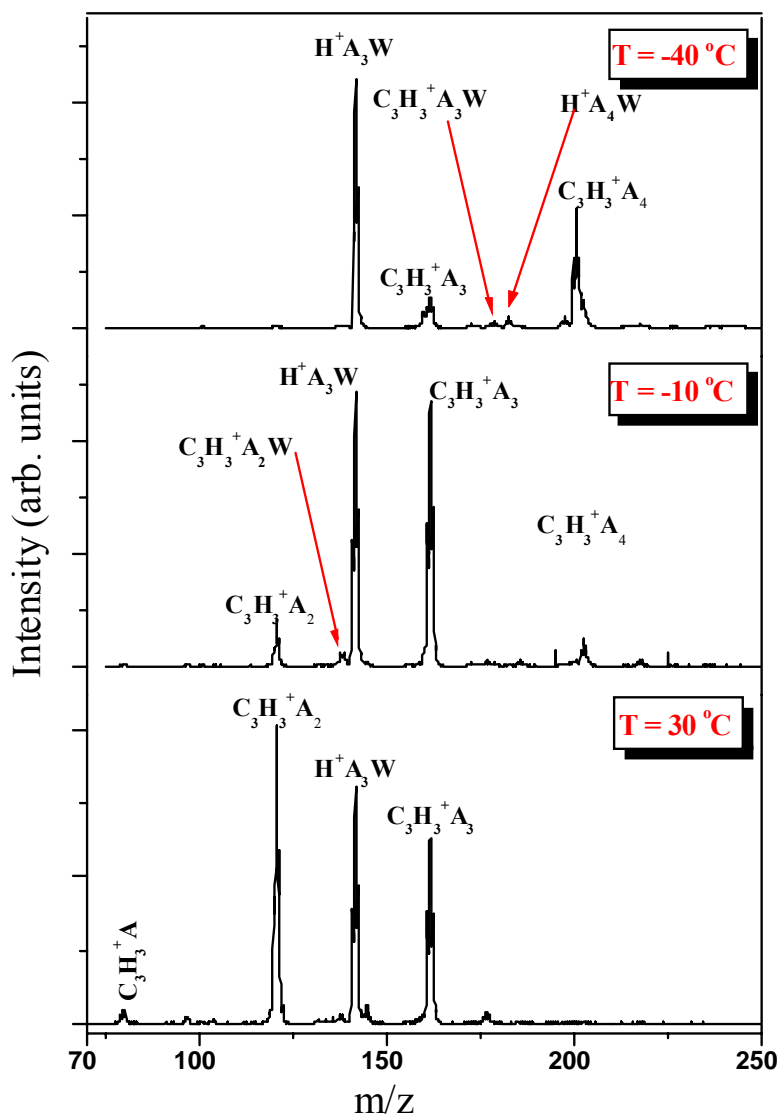
Figure 18: Mass spectra collected at different drift cell temperatures showing the stepwise clustering of acetonitrile molecules on the $C_3H_3^+$ where W represents water (H_2O) and A represents acetonitrile (CH_3CN).
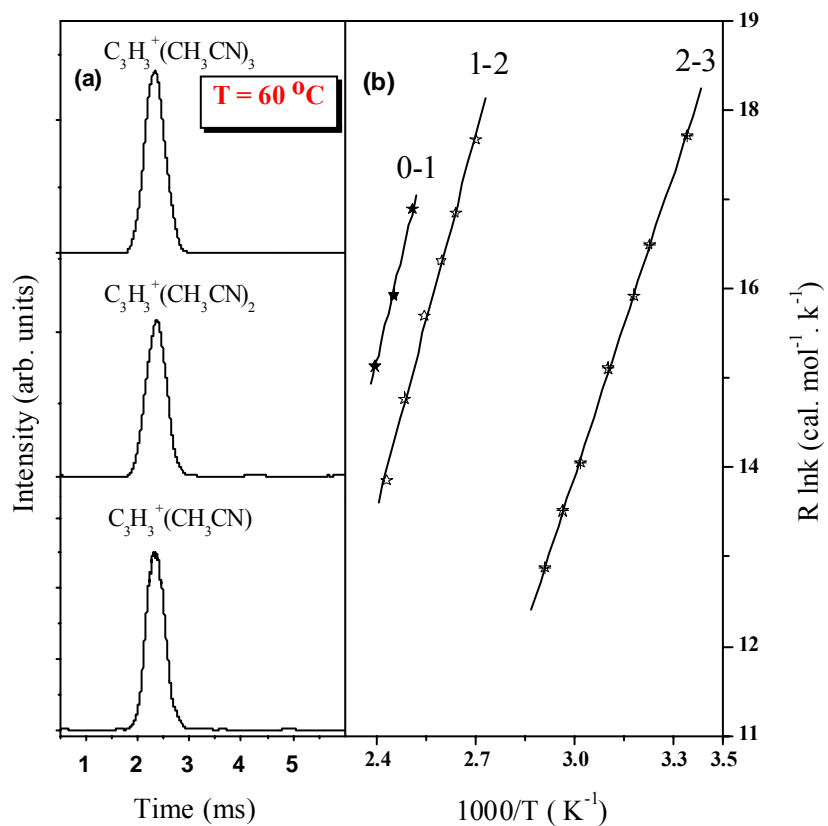
Figure 19: (a) Collected ATDs at 60 °C for the products formed by interactions between the $C_3H_3^+$ ion and the CH_3CN molecules through an equilibrium process confirmed by the equal ATD of all the ions. (b) van't Hoff plots relative to the addition of up to three acetonitrile CH_3CN molecules on the $C_3H_3^{\bullet+}$.

3.3 The Pyridine$^{\bullet+}$ system

3.3.1 Hydrophobic hydration of the pyridine$^{\bullet+}$ and 2-F-pyridine$^{\bullet+}$

The expansion of 100 psig of ultra pure helium seeded with a 0.1 % of pyridine or 2-F-pyridine vapor through a pulsed nozzle, operating at 100 Hz, into a vacuum chamber where the typical pressure is around 10^{-7} Torr., results in the formation of a neutral molecular beam. This beam will be ionized by EI ionization using 100-120 eV electrons to form the pyridine$^{\bullet+}$ or the 2-Fpyridine$^{\bullet\bullet+}$ When the protonated pyridine or 2-F-pyridine is needed, a source of proton, as a small amount of methanol CH_3OH or CD_3OD was added to the expansion. In all the studies, the ion of interest was always mass selected by the first quadrupole mass filter. The pyridine$^{\bullet+}$ (mass 79 amu) is injected into the drift cell filled with 0.27-0.40 Torr. of pure vapor of H_2O or D_2O. The injected ion was quickly thermalized by collisions with the water molecules escaping from the drift cell entrance pinhole. The pyridine$^{\bullet+}$ interacts with the water molecules inside the drift cell. Formation of new products takes place and equilibrium can be established.

$$C_5H_5N^{\bullet+}(H_2O)_{n-1} + H_2O \leftrightarrow C_5H_5N^{\bullet+}(H_2O)_n \qquad (6)$$
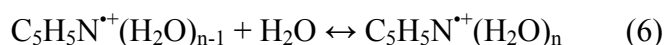
The stepwise clustering of water molecules on the pyridine$^{\bullet+}$ ion is expressed in equation (6). A typical testes for the equilibrium comes from the constant intensities ratio of the reactant $C_5H_5N^{\bullet+}(H_2O)_{n-1}$ and the product $C_5H_5N^{\bullet+}(H_2O)_n$ ions when the reaction time is varied by changing the drift cell voltage at a constant pressure and also the equal ATDs of all the ions which is fulfilled and Figure 20 shows that the $C_5H_5N^{\bullet+}$ and the products $C_5H_5N^{\bullet+}(H_2O)_n$ up to n = 3 are in equilibrium and have an equal arrival time.
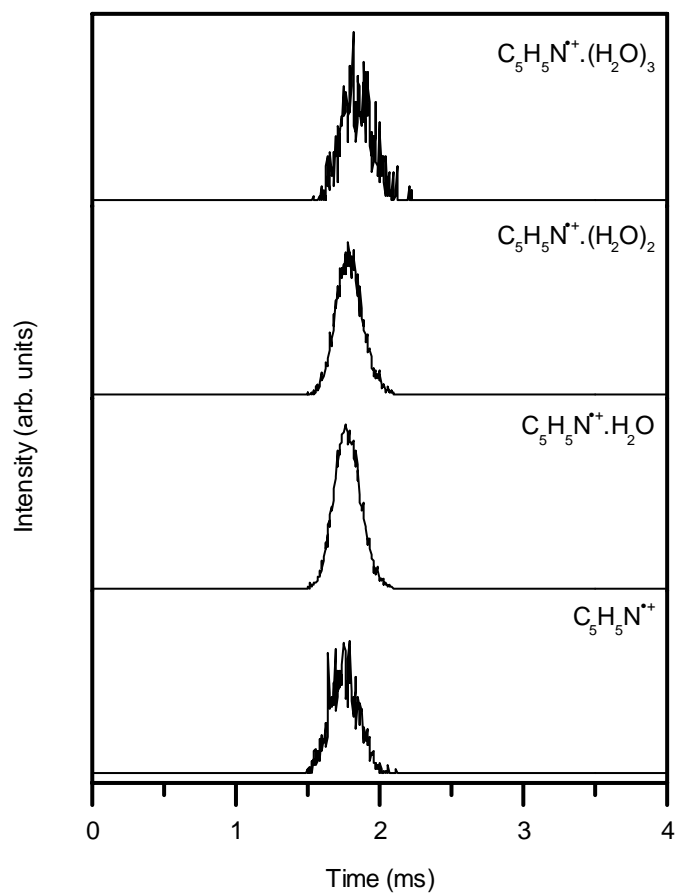
Figure 20: Arrival time distributions (ATDs) of ions formed by the injection of pyridine[•+] ions (17 eV lab. injection energy) into 0.45 mbar H_2O vapor at 304 K

The equilibrium constant of the stepwise clustering reactions can be obtained from the following equations:

$$K = \frac{\left[C_5H_5N^{\bullet+}(H_2O)_n\right]}{\left[C_5H_5N^{\bullet+}(H_2O)_{n-1}\right] \times \left[H_2O\right]} = \frac{I_{C_5H_5N^{\bullet+}(H_2O)_n}}{I_{C_5H_5N^{\bullet+}(H_2O)_{n-1}} \times P_{H_2O}} \qquad (7).$$

where I is the intensity of the ion obtained from the integration of the area under the ATDs peak. The drift cell temperature is varied and at each point of temperature an equilibrium constant is measured to generate the van't Hoff plots (Figure 21) of the clustering reactions. The binding energy ΔH^o and the entropy of the reaction ΔS^o are the slope and the intercept of the van't Hoff plots, given in kcal.mol^{-1} and cal.mol^{-1}.K^{-1} respectively.

Three different experiments are carried out for the stepwise solvation of three different ions by water molecules, the pyridine ($C_5H_5N^{\bullet+}$), the protonated pyridine ($C_5H_5NH^+$) and the 2-Fpyridine ($C_5H_4FN^{\bullet+}$). For each one of these reactions, the equilibrium conditions are satisfied and their ATDs are found to be identical for each set of cluster ions. Collected van't Hoff plots exposed in **Figure 21**, shows the addition of water molecules on these ions where the 2-Fpyridine adds up to five water molecules. However, only additions of three water molecules on the pyridine and protonated pyridine ions are measured. The experimental binding energies and the entropies of all the reactions are summarized in table 5.
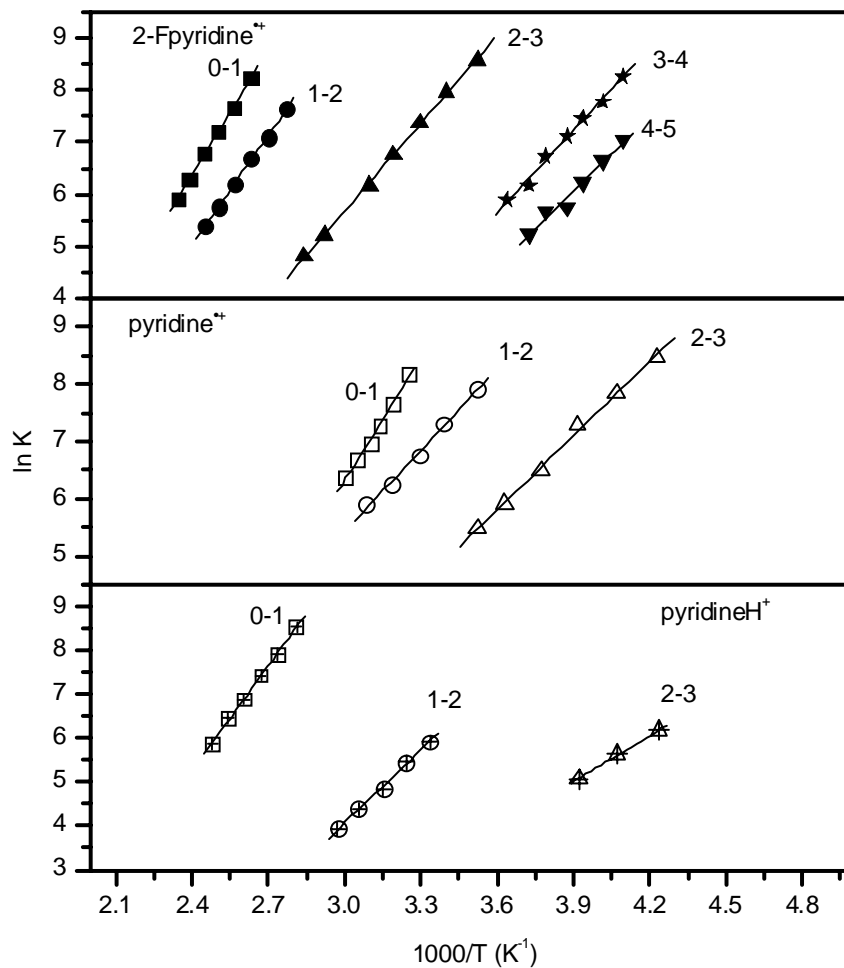
Figure 21: van't Hoff plots for the association equilibria $B(H_2O)_{n-1} + (H_2O) = B(H_2O)n$ for the ions B = 2-Fpyridine$^{\bullet+}$, pyridine$^{\bullet+}$ and pyridineH$^{\bullet+}$.

Table 5: Summarized experimental binding energies and entropies of the stepwise clustering reactions of water molecules on three different ions[a].

n	Pyridine[•+]		2-FPyridine[•+]		PyridineH[•+]		Benzene[•+b]	
	$-\Delta H^o$	$-\Delta S^o$	$-\Delta H^o$	$-\Delta S^o$	$-\Delta H^o$	$-\Delta S^o$	$-\Delta H^o$	$-\Delta S^o$
1	15.2	33.1	16.0	25.7	15.6 (15.0[c],16.1[d])	27.0 (25.5[c], 27.0[d])	9.0	19.5
2	9.9	19.0	13.6	22.4	11.5 (9.6[c])	26.0 (19.6[c])	8.0	18.9
3	8.8	20.2	11.3	22.3	6.9 (8.3[c])	17.1 (19.6[c])	8.0	
4	7.1	15.3	10.4	25.5			10.3	22.4
5			9.7	25.4			8.6	18.1
6			8.9[e]				7.8	15.1

[a] Units: The enthalpies and the entropies are given in kcal.mol^{-1} and cal.mol^{-1}.K[-1] respectively. Estimated uncertainties are based on standard deviations of the slopes and intercepts of van't Hoff plots, and reproducibility of cluster data from various sources: $\Delta H^o = \pm 1.0$ kcal.mol^{-1}, $\Delta S^o = 2.0 \pm$ cal.mol^{-1}.K[-1]. [b 9, 83]. [c 84]. [d 85]. [e] From measured ΔG^o assuming $\Delta S^o = -25.0$ cal.mol^{-1}.K[-1]

The binding energies of water molecules on the pyridine radical cation $C_5H_5N^{\bullet+}$ are found to be from 15-7 kcal.mol^{-1}. These values are above the expected, because in the conventional structure of the pyridine radical cation $C_5H_5N^{\bullet+}$ forms only the carbon–based $CH^{+}\cdots OH_2$ bonds similar to the one found in the benzene$^{\bullet+}$ $(C_6H_6^{\bullet+})$[9, 14]. Such hydrogen bonds are typically weak, about 8-12 kcal.mol^{-1}.[76,86]. However, the measured binding energies of the stepwise clustering of water molecules on the pyridine radical cation $(C_5H_5N^{\bullet+})$ are found to be equal to the values of the binding energies of water molecules to the protonated pyridine cation (PyridineH$^+$) within the uncertainty of $\pm$ 1 kcal.mol^{-1}. The clustering of water molecules on the 2-Fpyridine$^{\bullet+}$ shows a similar binding energy for the first water molecule (16.0 kcal/mol) and a decrease in the binding energy as the number of ligands is increased, except the values are slightly higher than what was found in the pyridine$^{\bullet+}(H_2O)_n$ and this increased interaction can be attributed to the possibility of direct interaction with the fluorine atom in the ortho-position.

The similarities between the binding energy values of pyridine$^{\bullet+}(H_2O)$ and protonated pyridineH$^+(H_2O)$ suggest a resemblance in their structures. In the protonated pyridine-water system, the water molecule is bonded to the protonated nitrogen by an $NH^{+}\cdots OH_2$ bond. This is an indication that the pyridine and the 2-F-pyridine may have a similar binding site where the first water molecule will attack. If the pyridine$^{\bullet+}$ and the 2-F-pyridine$^{\bullet+}$ demonstrate the ability of forming $NH^{+}\cdots OH_2$ bonds, than this hydrogen atom, that protonates the nitrogen molecule, must be shifted from a neighboring carbon atom which result in a the formation of protonated site and radical site. This behavior is

characteristic of distonic ions and therefore, we suggest the presence of the pyridine$^{\bullet+}$ and

2-F-pyridine$^{\bullet+}$ radical cations in distonic structures. Distonic ions are radical ions that

contain a protonated heteroatom, and a separate radical site. Distonic isomers are

formally related to conventional cations by H atom shift H-CRX$^{\bullet+}$ → $^{\bullet}$CRX-H^{+} to a

heteroatom. To better understand these similarities and to validate our proposed

structures, theoretical investigations of the binding energies and the structures of these

ions are extremely needed

3.3.2 Theoretical investigations and identification of distonic ions

3.3.2.1 Structure of the pyridine radical cation and its possible isomers

A potential energy study for the formation of pyridine distonic ion isomers from

the rearrangement of the conventional ion was completed and the results are offered in

Figure 23. In the pyridine conventional ion (structure 1a), if the hydrogen atom is shifted

from one of the two carbon atoms in the ortho position to the nitrogen atom, a barrier of

58.2 kcal.mol^{-1} was founded for this transition state (TS1) and the resulting distonic ion

(structure 1b) is more stable than the conventional one by 4.9 kcal.mol^{-1}. When the

distonic ion is formed by shift of hydrogen atom from a carbon atom in the meta position,

the barrier for this transition state (TS2) is found to be the highest (84.8 kcal.mol^{-1}) and

the formed distonic ion (structure 1c) is more stable than the conventional ion by 5.8

kcal.mol^{-1}. The most stable distonic ion isomer (structure 1d) comes from the

rearrangement of the conventional ion by shift of the hydrogen atom from the para-

postion to the nitrogen molecule. The barrier of the transition state is 63.8 kcal.mol^{-1}and

the stability is increased to 8 kcal.mol^{-1}with respect to the conventional ion energy.
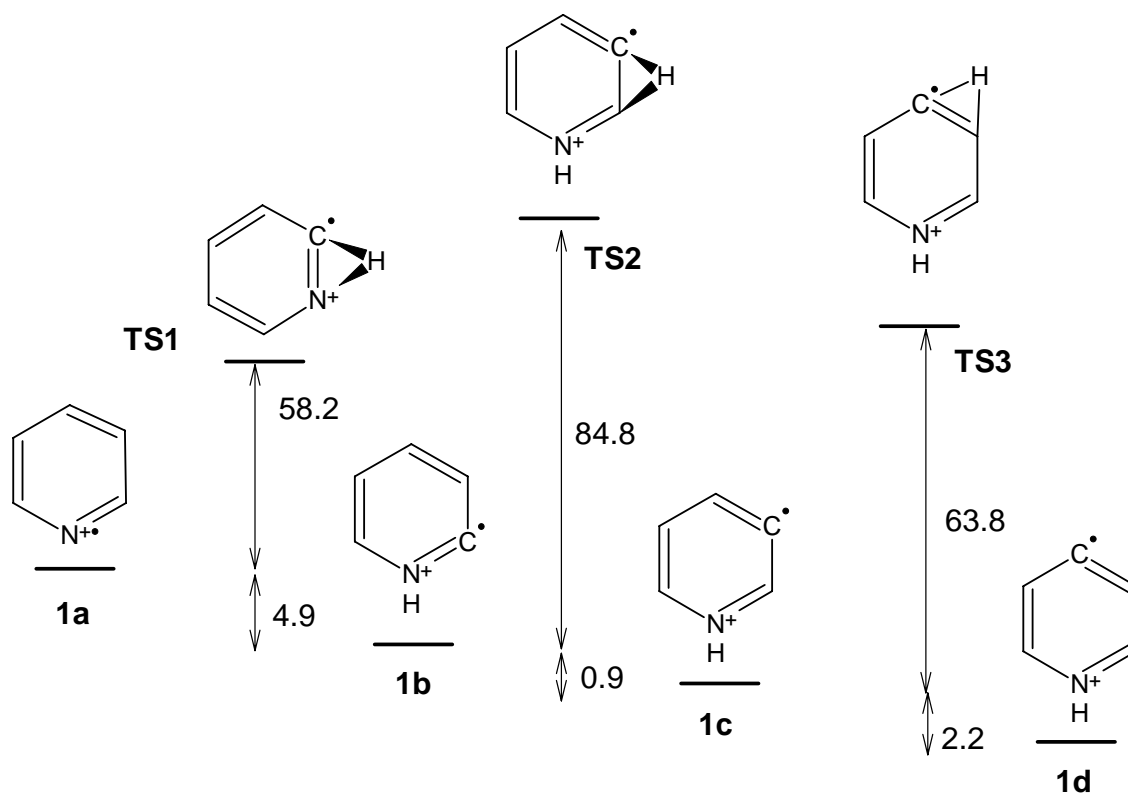
Figure 22: Potential energy diagram for conventional pyridine$^{\bullet+}$, distonic isomers and the transition states for the hydrogen shift. Energies are kcal/mol at MP2//ROHF-6-31+G** level (corrected for ZPE).

The electron impact ionization of pyridine generates the conventional ion.[46]. With the drift tube ion mobility technique, the conventional pyridine ion is injected into the drift cell with an injection energy of 17 eV which is more than what would be needed to overcome the highest barrier for the H shift in the second transition state, 84.8 kcal.mol^{-1} (3.7 eV) and previous calculations showed barriers of 60-70 kcal/mol for H shift among the isomers[44]. The 17 eV (392 kcal/mol) injection energy value is good enough to overcome these barriers where the background pressure in this region is about 10^{-5} Torr. However, an injection energy of 5 eV and collisions with water and other molecules apparently did not affect the isomers and they retain their distinct structures.[46] The formation of distonic ion can happen by proton transfer catalysis assisted by neutral ligand molecules,[87] and this can occur in ionized pyridine clusters in which ions are generated, or by interaction in the reaction cell, where a proton transfer to a ligand can lower the barrier to interconversion between isomers. For example, this mechanism was observed in HCN$^{\bullet+}$/HNC$^{\bullet+}$ catalyzed by CO,[88] in HCO^{+}/HOC^{+} catalyzed by Ar and N$_2$;[89] and in the conventional/distonic pair CH$_3$OH$^{\bullet+}$/$^{\bullet}$CH$_2$OH$_2^{+}$ catalyzed by H$_2$O.[90] Furthermore, hydrogen bonding to a ligand can decrease the barrier to rearrangement.[68]

In our system, the conventional ion C$_5$H$_5$N$^{\bullet+}$ may transfer a proton to H$_2$O in the excited [C$_5$H$_5$N$^{\bullet+}$(H$_2$O)$_n$]* clustering reaction intermediates, forming [$^{\bullet}$C$_5$H$_5$N$^{\cdots}$H^{+}(H$_2$O)$_n$]* which yield the $^{\bullet}$C$_5$H$_5$NH^{+}(H$_2$O)$_n$ distonic ion.

Optimized structures for the pyridine as a distonic and conventional ion and the protonated pyridine ion are generated for comparison reasons, by ab initio calculations at the ROHF/6-31+G** level and the results are presented in Figure 23. The similarities between the distonic ion and protonated ion structures are very obvious. When the hydrogen atom is shifted to protonate the nitrogen atom in the distonic structure, the N$\cdots$H bond length is found to be exactly equal to the one in the protonated ion (1.001 Å). Also, the atomic charges are found to be the same at the hydrogen and the nitrogen atoms. The comparison is made between the protonated pyridine ion and the distonic ion where the proton is shifted from the para-position, Figure 23 because this ion was found to be energetically the most stable one in our calculations (8 kcal/mol less than the conventional ion), and similar calculations done previously at the B3LYP/6-31+G** level (corrected for ZPE), showing the stability of isomer 1d by 3 and 2 kcal/mol over isomers 1b and 1c respectively. For the 2-F-pyridine, there are four possibilities of forming distonic structure (Figure 24) and this is relative to the positions from where the hydrogen atom can be shifted. The ab initio calculations at the ROHF/6-31+G** level shows that isomer 2c is found to be the most stable ion, where the hydrogen atom is shifted from the para position with respect to the nitrogen molecule similar to the pyridine behavior. This stability is expressed by 6.5 kcal/mol less in energy than that of the conventional one. Isomers 2b, 2d and 2e are less stable than isomer 2c and their energies are higher by 4.3, 2.3 and 3.4 kcal/mol respectively. The optimized structures of the conventional 2-F-pyridine ($C_5H_4FN^{\bullet+}$) and the distonic 2-F-pyridine ($^{\bullet}C_5H_3FNH^+$) at the ROHF/6-31+G** level are presented in Figure 25.

The calculations are extended to reach the proton affinity (PA) of some ions following the energy changes of this reaction:

$$XH^+ \rightarrow X + H^+ \quad (7)$$
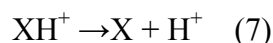
The energies of X and XH^+ species were taken from the MP2//ROHF/6-31+G** calculations at 0 K and corrected for the ZPVE and the energy of the proton is taken at zero. The pyridine PA is found to be 220 kcal/mol about 12 kcal/mol higher than the PA of the 2-F-pyridine, which are slightly lower than the tabulated experimental values, 222 and 211 kcal/mol respectively, where the experimental error margin is about ± 1.5 kcal/mol.[86] However the calculated PA of the conventional pyridine ion shows 208 kcal/mol for a deprotonation in the para position ($C_5H_5N^{\bullet+}$) and 216 kcal/mol when the deprotonation is happening at the nitrogen atom ($^\bullet C_5H_4NH^+$). Similar calculations were done for the 2-F-pyridine and the results reveal a PA of 198 kcal/mol for the conventional ion and 205 kcal/mol for the distonic ion. The experimentally calculated deprotonation of the conventional ion on the carbon atom is 208 kcal/mol (± 2-3 kcal/mol underestimations in the PA calculations), which is in excellent agreement with the value found for the deprotonation of the benzene radical cation $C_6H_6^{\bullet+}$ (211 kcal/mol). This similarity confirms the identical strength of the C-H bonds in both ions and this is can serve as an additional support towards the existence of the pyridine as a distonic ion.
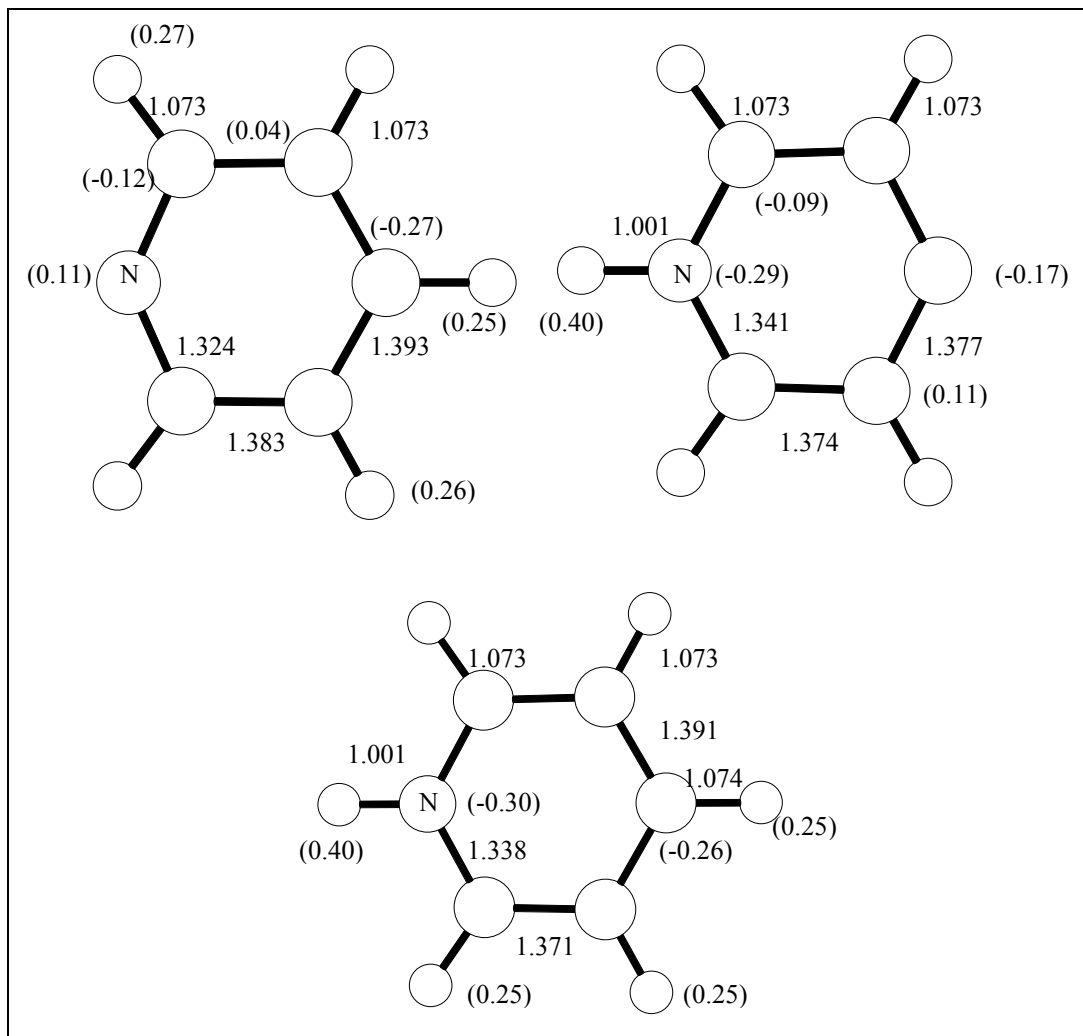
Figure 23: Optimized structures of the conventional (upper left) and distonic (upper right) isomers of pyridine$^{•+}$ and of pyridineH$^+$ (bottom), calculated at the ROHF/6-31+G** level. Distances are in Angstrom (1 Angstrom = 0.1 nm) and atomic charges are shown in parentheses. Note the similarities between the atomic charges and bond distance about the NH$^+$ centers in the protonated and distonic ions
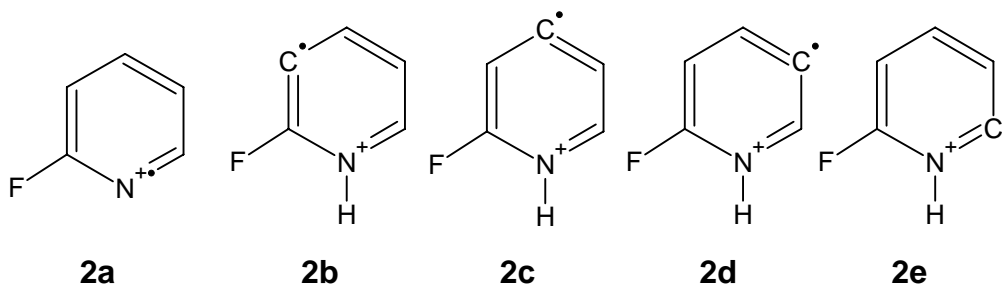
Figure 24: Isomers of the conventional (a) and distonic (b - e) isomers of the 2-F-pyridine$^{\bullet+}$ ion.
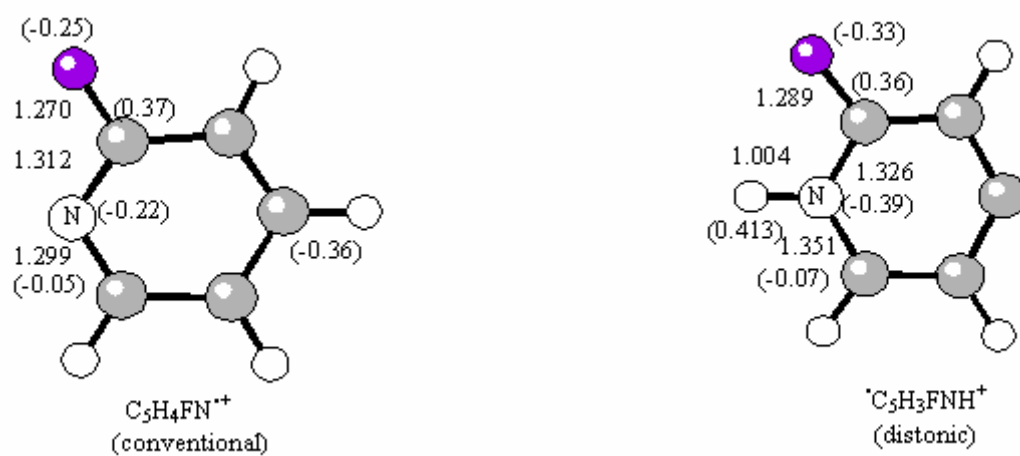
Figure 25: Optimized structures for the conventional 2-F-pyridine and the distonic 2-F-pyridine ions at the ROHF/6-31+G** level.

3.3.2.2 Thermochemical identification of distonic ions

The stepwise clustering energies are calculated at the MP2//ROHF-6-31+G** level and corrected for ZPE and BSSE for a series of ions: the pyridine conventional and distonic, the protonated pyridine, the 2-F-pyridine conventional and distonic, and the protonated 2-F-pyridine. The results are summarized and presented in **Table 6**. The calculated binding energy of one water molecule to the conventional pyridine ion is found to be -10.2 kcal/mol, which is 5 kcal/mol less than the experimentally measure value (-15.2 kcal/mol). However, the calculated binding energies of one water molecule to pyridine distonic isomers, (1b, 1c and 1d in figure 23) are in good agreement with the experimental value. Nevertheless, the binding energy calculated for the clustering of the three water molecules on the most stable distonic ion (structure 1d), are in full agreement with the measured values. The 2-F-pyridine shows a similar behavior and there is agreement between the calculated binding energy of the distonic ion (-15.9 kcal/mol) and the experimental values (-16.0 kcal/mol) but the conventional ion illustrates a 10.0 kcal/mol for the binding energy of one water molecule. For a comparison reasons, the calculations are extended to the protonated pyridine and protonated 2-F-pyridine. The results agree with the experiment for the protonated pyridine ion, -15.5 kcal/mol for the experimental value and -14.5 kcal/mol for the calculated one. On the other hand, the calculated binding energy of the protonated 2-F-pyridine (-15.5 kcal/mol) agrees with the value found in the distonic 2-F-pyridine and with the distonic pyridine ion, which indicates that the distonic structure of the pyridine is conserved and not affected by the presence of the nitrogen molecule in the structure.

Table 6: Stepwise binding energies of H_2O molecules to ions at MP2//ROHF/6-31+G** corrected for ZPE and BSSE.[a] Experimental values in italics.

n	Pyridine•+				2-FPyridine•+		pyridineH+	2-FpyridineH+
	C_5H_5N•+ (conventional)	•$C_5H_4NH^+$ (distonic)[b]			C_5H_4FN•+ (conventional)	•$C_5H_3FNH^+$ (distonic)	$C_5H_5NH^+$	$C_5H_4FNH^+$
		1b	1c	1d				
1	-10.2	-15.4	-15.0	-15.4 (-15.2)	-11.3	-15.9 (-16.0)	-14.5 (-15.6)	-15.5
2		-10.3		-10.2 (-9.9)			-9.9 (-11.5)	-10.3
3				-8.7 (-8.8)				

a) Units are kcal mol^{-1}.

b) The numbering refers to the position of the radical relative to the nitrogen atom, see Figure 6.

Optimized structures, at the ROHF-6-31+G** level for the additions of one and two water molecules on the protonated pyridine, $C_5H_5NH^+(H_2O)_{1,2}$ and the distonic pyridine, $C_5H_4NH^{\bullet+}(H_2O)_{1,2}$ ions are presented in Figure 27. For comparison the structure of the conventional pyridine ion with one water molecule, $C_5H_5N^{\bullet+}\cdots H_2O$ is presented in Figure 28. The clustering of one water molecule on the protonated pyridine ion shows the formation of a hydrogen bond between the oxygen atom of the water molecule and the hydrogen atom bonded to the nitrogen of the ion. The same kind of bond is established in the clustering of one water molecule to the distonic pyridine ion. The formed hydrogen bonds ($H_2O^{\cdots\bullet+}HN$) have similar strength and their lengths are comparable, 1.834 and 1.829 Å for the protonated pyridine and the distonic pyridine respectively. In both cluster ions, $C_5H_5NH^+(H_2O)$ and $C_5H_4NH^{\bullet+}(H_2O)$ the N-H bond lengths are the same (1.014 Å), the nitrogen fractional charges are equal (-0.32 C), the oxygen atom charges are identical (-0.80 C) and the hydrogen atom charges are similar (0.49 and 0.50 C). The resemblance between these two cluster ions is extended to the molecular charges, where the water molecule holds only 1 % of the total charge and 99 % remain with the core ion in both cases. However, the optimized structure for the clustering of one water molecule on the conventional pyridine ion shows the formation of a bond between the oxygen atom of the water molecule and the nitrogen atom of the ion. This bond (2.707 Å) is weaker than the previously observed one and the molecular charges are different too, where the total charge is localized on the core ion with 0 % on the water molecule.

The optimized structures of the clustering of two water molecules on the distonic pyridine $C_5H_4NH^{\bullet+}(H_2O)_2$ and the protonated pyridine $C_5H_5NH^+(H_2O)_2$ ions are included in Figure 27. In both cluster ions, the second water molecule is attached to the first one by hydrogen bond through a water-water interaction. For the distonic ion with two water molecules, two cluster isomers are shown; their energies are higher by 0.60 kcal/mol for the one having the two water molecules forming two hydrogen bonds with two adjacent hydrogen atoms of the distonic ion and by 2.43 kcal/mol for the isomer where one water molecule is forming a hydrogen bond and the other one is in shared position between two hydrogen atoms of the distonic ion.
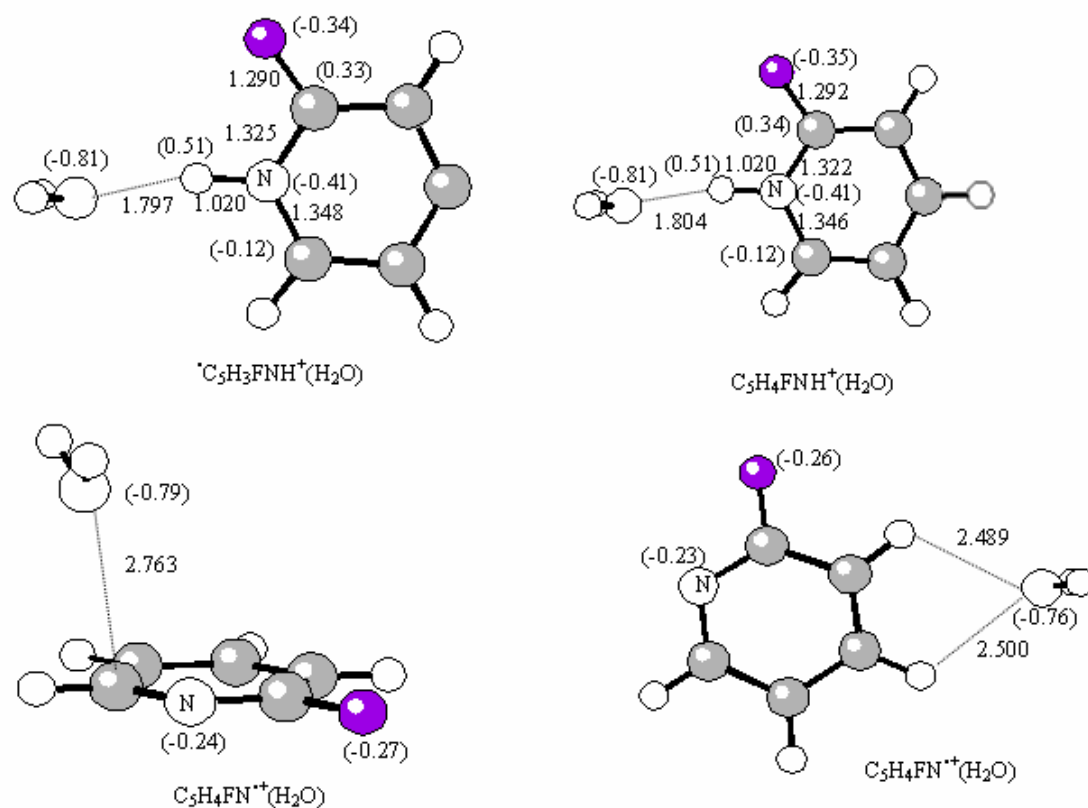
Figure 26: illustrates the optimized structures at the ROHF/6-31+G** level of the ab initio calculations for the addition of one H_2O molecule on the distonic 2-F-pyridine [$^•C_5H_3FNH^+(H_2O)$], the protonated 2-F-pyridine [$^•C_5H_4FNH^+(H_2O)$] and the conventional 2-F-pyridine [$C_5H_4FN^+(H_2O)$].

Similar to the results observed in the pyridine system, the distonic structure of the 2-F-pyridine with one H_2O molecule shows a similarity to the protonated 2-F-pyridine ion with one H_2O and dissimilarity to the conventional structure. The similarities include the hydrogen bond lengths $H_2O^{\cdots\bullet+}$H-N (1.797 and 1.804 Å), the $^+$H-N bond distances (1.020 Å), the nitrogen partial charges (-0.41 C), the hydrogen partial charges (0.51 C), the fluorine atom local charges (-0.34 and -0.35 C) in the distonic and protonated ions respectively. For the conventional ion with one H_2O molecule, two structures are presented. In one, the water molecule forms two hydrogen bonds with two adjacent hydrogen atoms in position 3 and 4 in the ion and the bond lengths are found to be 2.489 and 2.500 Å. In the second structure, the water molecule is forming a bond on a vertical direction to the carbon atom in the 6th position. However, neither of these two structures for the conventional ion presents any similarity either to the distonic ion or to the protonated ion.
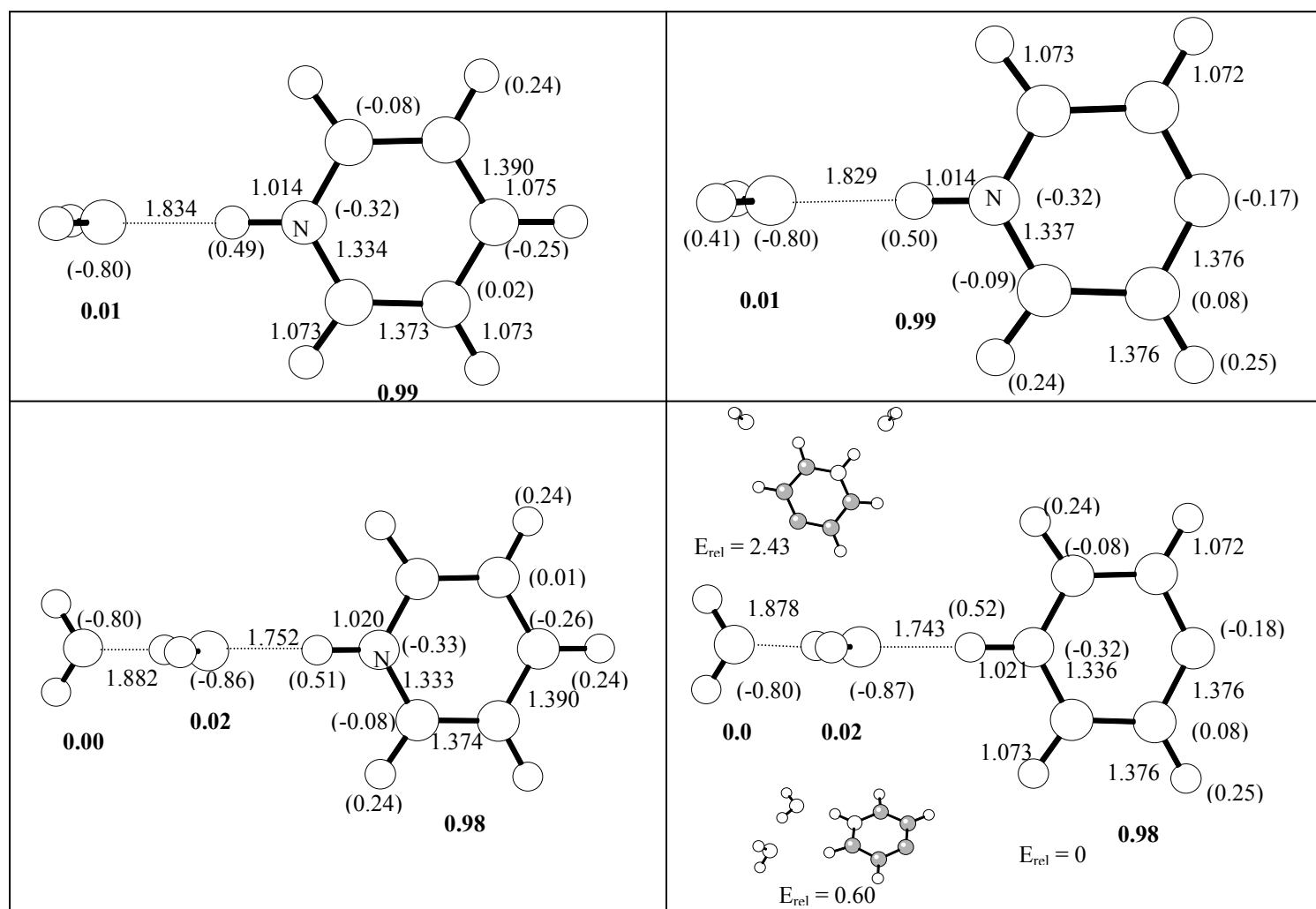
Figure 27: Optimized structures of $C_5H_5NH^+(H_2O)_{1,2}$ (left panels) and $C_5H_4NH^{•+}(H_2O)_{1,2}$ (right panels) at ROHF/6-31+G** level. Distances are in Angstrom, molecular charges are shown in bold and atomic charges are shown in parenthesis. Inserts in the bottom right panel show isomers with alternative structures and their relative energies (kcal/mol). Note the similarities between the bond lengths and atomic and group charges of the bonds and ligands in the respective clusters of the protonated and distonic ions
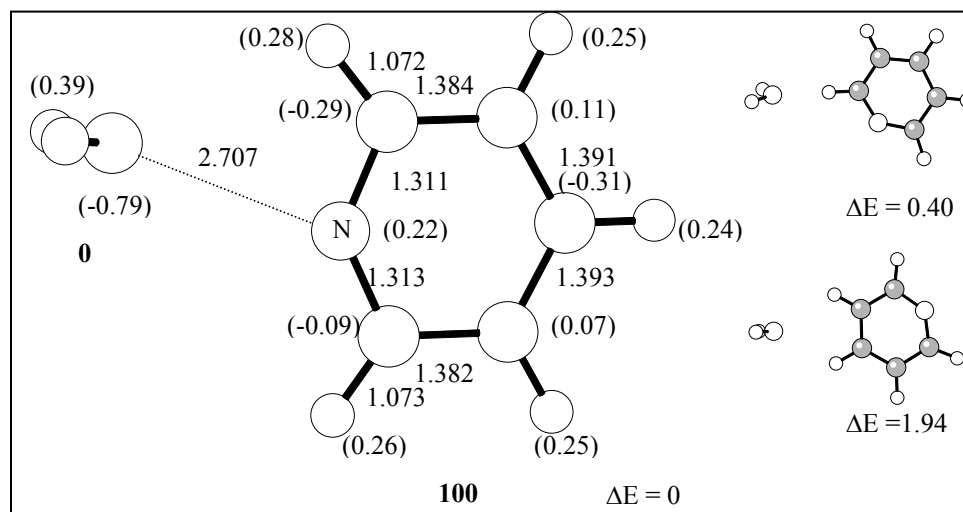
Figure 28: Optimized structures of $C_5H_5N^{\bullet+}\cdot\cdot H_2O$ (hydrated classic pyridine$^{\bullet+}$ isomer) ion at ROHF/6-31+G** level. Distances are in Angstroms, molecular group charges are in bold and atomic charges are shown in parentheses. Inserts in the bottom right panel show isomers with alternative structures and their relative energies (kcal/mol)
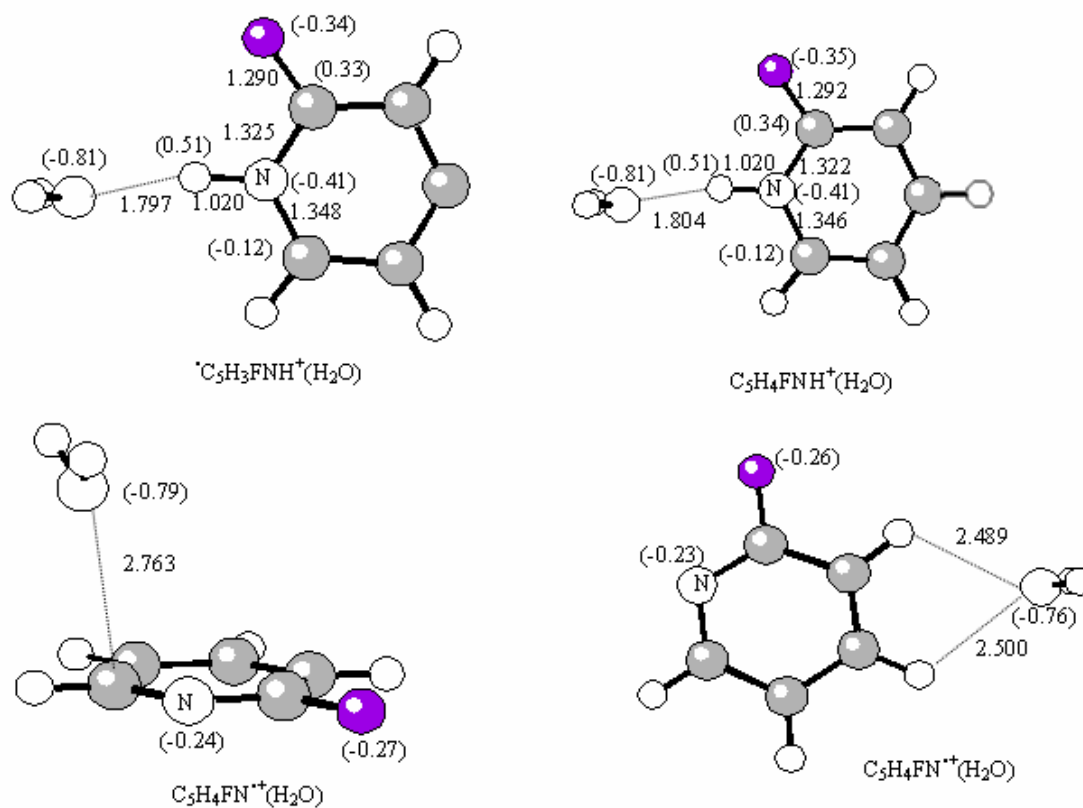
Figure 29: Optimized structures of $C_5H_4FN^{\bullet+}$(2-Fpyridine$^{\bullet+}$) (conventional and distonic), and adducts of the ions with one H_2O molecule: distonic radical ion (middle left), protonated ion (middle right), and two isomers of the conventional radical ion (bottom) at the ROHF/6-31+G** level.

3.3.3 Further reactions with water vapor

The investigation of the pyridine-water system did not stop at the solvation level, but it was extended to some observed phenomena where the study reached observed reactions of hydrogen atom transfer from water molecules to the ion. Also, H/D exchange reactions are examined and the last search was focused on the deprotonation of these ions by an assembly of water molecules to form protonated water cluster and leaving a free radical similar to the study conducted in the deprotonation reaction of the $C_3H_3^+$ ion.

3.3.3.1 Hydrogen transfer from water

The energy of the hydrogen transfer reaction (3) can be calculated for both ions based on the calculated energy differences between the conventional pyridine and the distonic pyridine ions and tabulated ion energetics.[86]

$$C_5D_5N^{\bullet+} + H_2O \rightarrow C_5D_5NH^+ + OH^{\bullet} \quad (3)$$

The calculations show that this reaction should be exothermic by 2 kcal/mol for the conventional ion, within the uncertainty of the thermochemical data. If this reaction is indeed exothermic it should be very fast and under our conditions its completion time should be less than 10^{-7}s. However the collected mass spectrum in

Figure 30 (top panel) after the injected of the C_5D_5N ion, mass 84 amu to the cell filled with 0.34 Torr of water vapor at 333 K did not show the presence of a peak at mass 85 amu relative to the transfer of hydrogen atom from water to the ion. The results are consistent with the distonic ion which is expected not to be reactive.

3.3.3.2 H/D exchange reactions

The H/D exchange reaction in the presence of the injected C_5D_5N ion into the cell filled with water vapor can be described in reaction 4.

$$C_5D_4ND^{\bullet+}(H_2O)_n + H_2O \rightarrow C_5D_4N[(H_2O)_nD^+] + H_2O \rightarrow C_5D_4N[(H_2O)_nH^+] + HDO \qquad (4)$$

The collected mass spectra at different drift cell temperatures, shown in Figure 29 and Figure 30, show that at 333 K (top panel) the H/D exchange reaction is not observed, and the injected ion C_5D_5N adds a water molecule relative to the peak observed at mass 102 amu. When the temperature is decreased to 298 K (center panel), the H/D exchange reaction is observed but it is slow. The H/D exchange reaction is clear by the presence of two peaks for each addition of H_2O molecule on the ion. For example for the addition of the first water molecule on the injected C_5D_5N ion, the scan shows the presence of a peak at 102 amu relative to the $C_5D_5N.H_2O$ ion and another peak higher in intensity at mass 101 amu relative the $C_5D_4HN.H_2O$ ion where a D atom is substituted by an H atom. For the addition of two H_2O molecules, peaks at 119 and 120 amu are observed relative to the $C_5D_4HN.(H_2O)_2$ and $C_5D_5N.(H_2O)_2$ ions respectively. When the temperature is decreased to 273 K (bottom panel), the reaction becomes fast and only ions relative to the

exchanged D atom are observed. When the protonated pyridine ion $C_5H_5ND^+$ is injected into the drift cell under the same conditions previously described, no sign for H/D exchange reactions was observed. The collected mass spectrum, at 245 K in Figure 31 shows peaks at 99, 117, 135 and 153 relative to the addition of 1-4 water molecules respectively. The presence of the protonated water clusters in small intensities can be resulting from a high injection energy process. The injection of the 2-F-pyridine ion $C_5H_4FN^+$ in D_2O vapor did not show the presence of H/D exchange reaction. However, the injection of protonated 2-F-pyridine ion $C_5H_4FND^+$ in H_2O vapor did illustrate the occurrence of H/D exchange reactions and this can be clearly distinguished from the collected mass spectra in Figure 32 where peaks at 116,134, 152 and 170 amu are observed relative to the addition of 1-4 water molecules on the exchanged ion $C_5H_4FNH^{\bullet+}$

3.3.3.3 Deprotonation reaction by water molecules

The formation of the protonated water clusters, $H^+(H_2O)_n$ becomes more favorable at higher cluster where the intra-cluster proton transfer can result in the formation of stable ions by strong hydrogen-bond network. Such a reaction is observed only with the 2-F-pyridinein and the protonated 2-F-pyridinein where the PA is relatively low PA (211 kcal/mol). The experimental results did not show the deprotonation reaction of the pyridine ion and this can be used as support argument because the distonic ion has a higher PA.
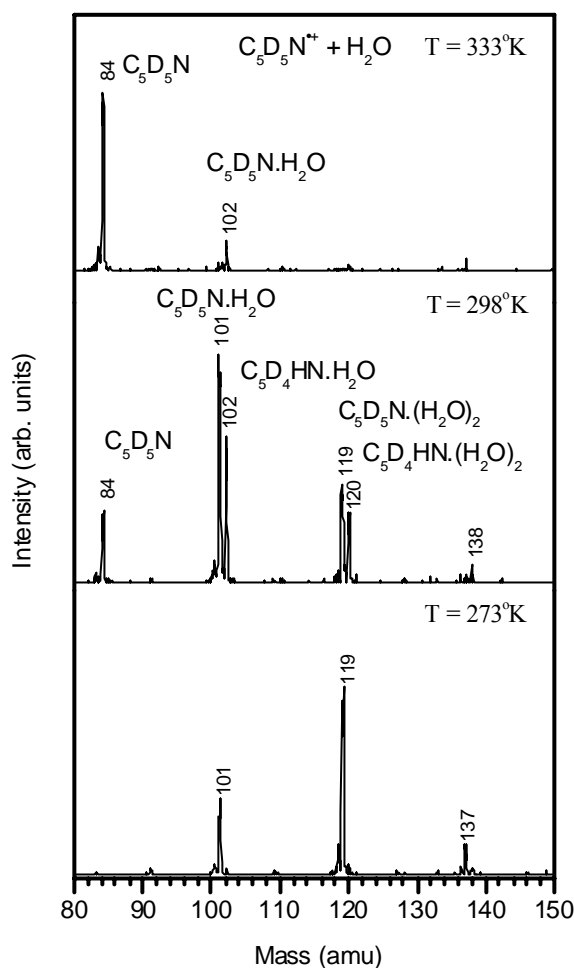
Figure 30: Mass spectra of pyridine-$D_5^{\bullet+}$ (m/z 84) injected into H_2O vapor. $P(H_2O)$ = 0.34 mbar (298°K), injection energy = 17 eV (lab frame). Top panel: Note the absence of $C_5H_5NH^+$ ions, indicating that the ion does not extract H atoms from H_2O, and the absence of H/D exchange product at m/z 101 at 333 K. Center and bottom panels: Note the presence of both non-exchanged and exchanged ions at m/z 101, 102; 119, 120, at 298 K, indicating some intra-cluster proton transfer and consequent slow H/D exchange with water vapor at 298 K, and faster H/D exchange at 273 K leaving only exchange ions. Also note the absence of $(H_2O)_nH^+$ ions indicating that the ions are not deprotonated by water vapor to form protonated water clusters.
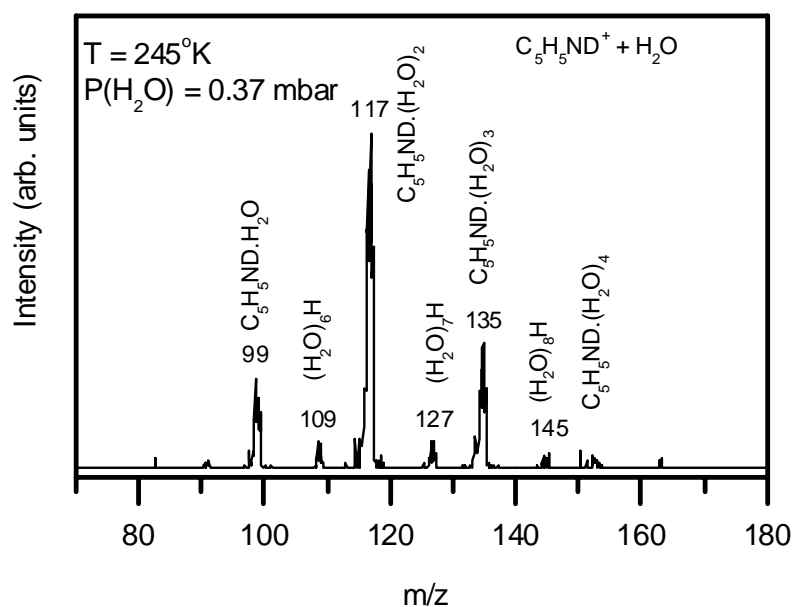
Figure 31: Injection of protonated pyridine (here, the deuterium labeled $C_5H_5ND^+$ ion), into H_2O vapor to test H/D exchange and deprotonation of the ions. (Injection energies of 17 eV lab.). Only $C_5H_5ND^+(H_2O)_n$ clusters produced. No exchange between $C_5H_5NH^+(H_2O)n$ clusters. The minor water clusters observed are possibly from high-energy injection processes. The results show that pyridineH+ does not undergo intra-cluster proton transfer to water or overall deprotonation by water.
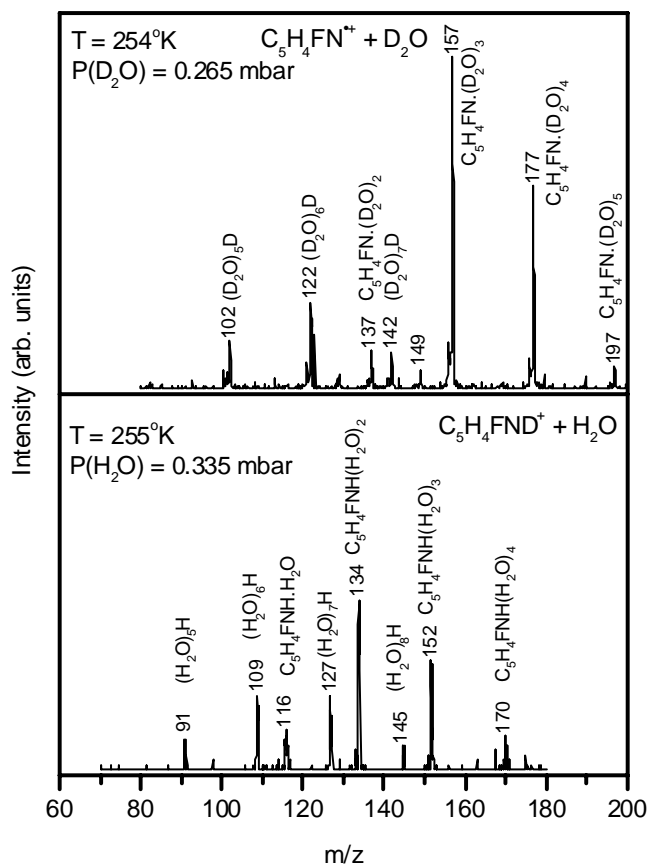
Figure 32: Injection of 2-F-pyridine[•+]into D_2O vapor (top panel) and of 2-F-pyridineD[+] into H_2O vapor (bottom panel) at injection energies of 17-20 eV (lab.). Top panel: The 2-F-pyridine[•+]$(D_2O)_n$ ions do not undergo H/D exchange to form [•]$C_5H_3ND^+(D_2O)_n$ ions, indicating no intra-cluster proton transfer. However, the water clusters $(D_2O)_nD^+$ indicate overall deprotonation by water. Bottom panel: Injection of protonated 2-$FC_5H_4ND^+$ into H_2O vapor produces the exchanged 2-$FC_5H_4NH^+(H_2O)_n$ clusters indicating D/H exchange and intra-cluster proton transfer, and the $(H_2O)_nH^+$ clusters indicating overall deprotonation. (Note: The split peaks are instrumental artifacts; each represents only one m/z value).

3.3.4 Comparison between benzene $C_6H_6^{\bullet+}$, the $C_3H_3^+$ and the pyridine$^{\bullet+}$

The stepwise solvation of the benzene radical cation, $C_6H_6^{\bullet+}$ was investigated in previous work and it will be used here for a comparison purpose. The comparison will be based on shared similarities found between these ions such as aromaticity, structures, C-H bond strength, and PAs. This number of similar properties can help understand the measured results and can reveal some useful information about the behavior of these ions in such an environment.

3.3.4.1 Binding energies of water and acetonitrile molecules

The hydration of the $C_6H_6^{\bullet+}$ by water molecules shows C-H binding energies of 8-10 kcal/mol (table 5). These values are similar to the values found in the clustering of water molecules on the $C_3H_3^+$ (Table 2) with a small increase which can be attributed to the more localized charge in the smaller ion $C_3H_3^{\bullet+}$ The benzene-water system was also used as a tool for the identification of the solvated pyridine distonic ion. Because the measured binding energies in the pyridine-water system were found higher than the expected C-H$^{\cdots}$OH$_2$ interaction which support the argument of the existence of the pyridine in a distonic in the presence of water molecules.

The solvation of the $C_6H_6^{\bullet+}$ cation by CH$_3$CN molecules is needed since the comparison to the $C_3H_3^+$ ion should be taken further where the possibility of the extended hydrogen bonds network could be interrupted. The injection of $C_6H_6^{\bullet+}$ into the drift cell containing 0.2 Torr of CH$_3$CN results in the formation of products and the collected mass spectra presented in figure 33 shows the addition of two CH$_3$CN molecules on the

$C_6H_6^{\bullet+}$ with the intensity of the second one very weak. At the same temperature, the benzene fragment $C_4H_4^+$ (labeled F in the spectrum) is adding one and two CH_3CN molecules. The $C_4H_4^+$ is a product of the dissociation of the $C_6H_6^{\bullet+}$ which can happen after collisions with CH_3CN molecules. At lower temperature (-48 ^{o}C) the cluster distribution is different where the $C_6H_6^{\bullet+}$ adds up to three CH_3CN molecules, the fragment $C_4H_4^+$ and the $C_4H_4^+(CH_3CN)_n$ are no longer present and the formation of mixed clusters is observed by the presence of protonated water adding two CH_3CN and a mixture of H_2O and CH_3CN on the $C_6H_6^{\bullet+}$ (BWA$_2$). The equilibrium conditions are met, the equal ATDs of the $C_6H_6^{\bullet+}$ and $C_6H_6^{\bullet+}(CH_3CN)_n$, n = 1-3 and the van't Hoff plots are accessible in Figure 34. The experimentally measured binding energies are summarized in Table 7. The addition of the first CH_3CN is found to have the same binding energy in both $C_3H_3^+$ and $C_6H_6^{\bullet+}$ ions (-15.3 and -15.1 kcal/mol respectively). When more CH_3CN molecules are clustered on the $C_6H_6^{\bullet+}$ the binding energies were decreased, by about 3 kcal/mol relative to the one measure with the $C_3H_3^+$ and this can be attributed to the charge effect where it is more localized in the smaller ion.

3.3.4.2 Comparison of the deprotonation reactions

The weak minimum seen in the $C_3H_3^+(H_2O)_n$ cluster distribution at n = 3 (figure 13) was observed also in the $C_6H_6^{\bullet+}$/water system but with a more distinct minimum at the same cluster size (n = 3). If the $C_3H_3^+$/water system showed that the depletion of the cluster ion at n =3 between the formation of higher cluster ion (n = 4) and the proton transfer reaction to form the protonated water cluster did not disturb the establishment of the equilibrium, then the competition in the benzene/water system was stronger from the

deprotonation reaction and the equilibrium with the higher cluster ion did not take place.[9,83] In both systems, $C_6H_6^{\cdot+}$/water and $C_3H_3^{+}$/water the deprotonation reaction of the ion and the formation of the protonated water clusters $H^+(H_2O)_n$ was observed by the association of water molecule $(H_2O)_n$ for n more than 3. The kinetics of the deprotonation reaction was studied in both systems and the results gave the same activation energy -37 $\pm$ I kcal/mol. The same reaction is observed in the 2-F-pyridine ion with water and this was attributed to the similarity found in the ions proton affinities: 211 kcal/mol for the 2-F-pyridine and 212 for the $C_6H_5^{\cdot}$ radical.
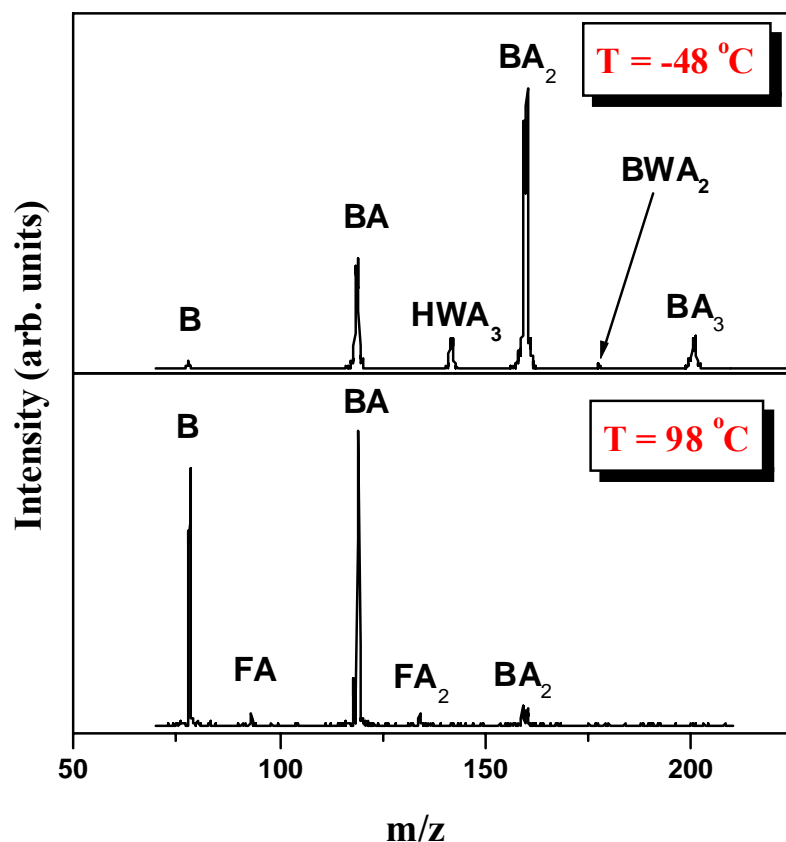
Figure 33: Collected mass spectra at two different drift cell temperatures showing the increased addition of acetonitrile molecules (A) on the $C_6H_6^{\bullet+}$(B) from 98 to -48 ^oC where three molecules are observed. The figure shows also the addition of acetonitrile molecules on the benzene fragment $C_4H_4^+$ (F) at high temperature and the formation of protonated acetonitrile water cluster (HWA_3) and the addition of water and acetonitrile on the $C_6H_6^{\bullet+}$(BWA_2).
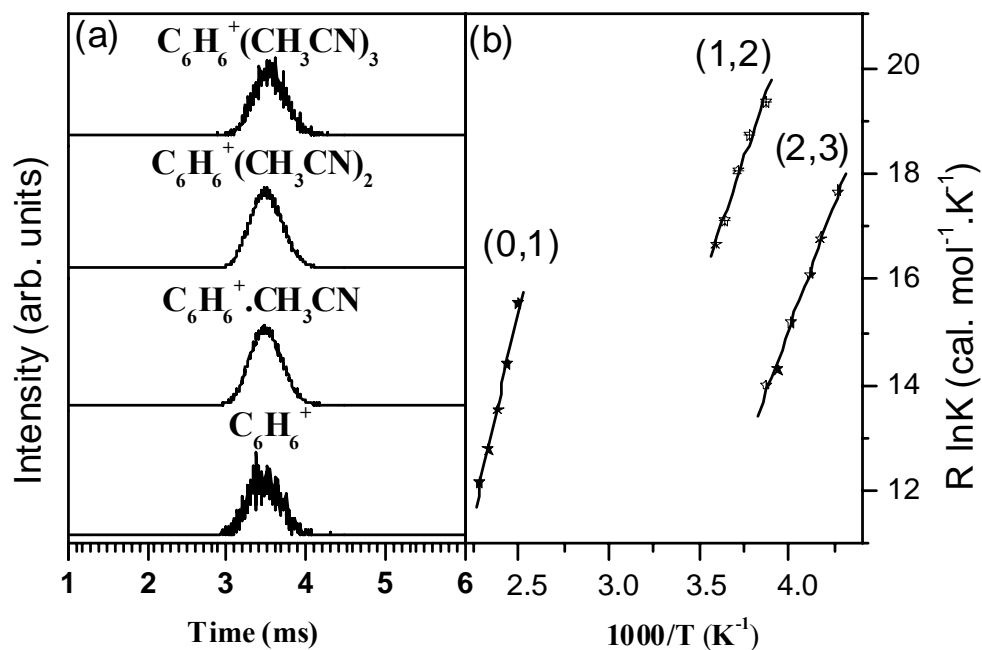
Figure 34: (a) Collected ATDs of the $C_6H_6^{\bullet+}$ and $C_6H_6^{\bullet+}(CH_3CN)_n$, n = 1-3 obtained by the equilibrium $C_6H_6^{\bullet+}(CH_3CN)_{n-1} + CH_3CN \leftrightarrow C_6H_6^{\bullet+}(CH_3CN)_n$. (b) the van't Hoff plots relative to the addition of the three CH_3CN molecules presented by (n-1)-n steps where n = 1-3.

Table 7: Binding energies measured from equilibria between $C_6H_6^{\bullet+}$ion CH_3CN molecules. $C_6H_6^{\bullet+}(CH_3CN)_{n-1} + CH_3CN \leftrightarrow C_6H_6^{\bullet+}(CH_3CN)_n$

n	ΔH^o (kcal/mol)	ΔS^o (cal.mol^{-1}.K^{-1})
1	-15.1	-22.5
2	-10.5	-19.3
3	-9.4	-22.1

3.4 Conclusions

We examined the gas-phase solvation and deprotonation of the $C_3H_3^+$ ion. Mobility and reactivity measurements indicate that we are observing the stable $c\text{-}C_3H_3^+$ isomer under our conditions. The binding energies of the hydrated clusters of about 8 – 12 kcal mol^{-1} and the somewhat stronger bonds to the more polar CH_3CN molecules are typical for carbon-based $CH^+\cdots X$ hydrogen bonds. The thermochemistry for deprotonation becomes favorable for deprotonation by four or more H_3O^+ molecules, due to the formation of strong hydrogen bonds in the product $(H_2O)_nH^+$ cluster ions. The deprotonation reactions perturb the cluster distributions, with depleted intensities of the $C_3H_3^+(H_3O)_3$ clusters, which appears to perturb the thermochemical measurements that involve this cluster.

The observed behavior of the $C_3H_3^+$/water system is fully analogous to the benzene$^{\bullet+}$/water system, suggesting that similar phenomena may apply also in other reactions of ionized hydrocarbons with solvent molecules. We observed analogous multibody associative charge transfer (ACT) reactions of benzene$^{\bullet+}$ and toluene$^{\bullet+}$ with olefins, where charge transfer is driven by the formation of covalent bonds in the product ions.[91, 92]

In a general, these associative transfer reactions are driven by the formation of strong bonds in the product ions. These associative proton or charge transfer reactions require the assembly of a multi-body cluster, which is favored at low temperatures. Accordingly, these reactions show negative temperature coefficients, including unprecedented steep negative temperature dependence in the $C_3H_3^+$/water and

benzene$^{\bullet+}$/water systems. The reactions may reach unit collision efficiency at sufficiently low temperatures. This can allow ionized polycyclic aromatics to affect polymerization and ion-induced formation of ices in low-temperature astrochemical environments.[93] We measured the thermochemistry of step-wise hydration of the pyridine$^{\bullet+}$ radical. Comparisons with the benzene$^{\bullet+}$ and with pyridineH$^+$ ions suggest that pyridine$^{\bullet+}$ has a distonic structure protonated on nitrogen that can form an NH$^+\cdots$OH$_2$ bond. This agrees with ab initio calculations that show the distonic ion to be the lowest energy isomer. The stability of the distonic vs. classical ion can be enhanced further by the stronger solvation of the distonic isomer.

The similar hydrogen bond energies of pyridine$^{\bullet+}$ and pyridineH$^+$ to H$_2$O show that a radical site away from the hydrogen bonding center has little effect on the hydrogen bond. This verifies that proton affinity correlations established by even-electron protonated ions can estimate hydrogen bond strengths also of distonic ions.[68, 72, 73,94]

The distonic structure of the pyridine$^{\bullet+}$ ion observed here is consistent with reactivity with respect to intra-cluster deprotonation and overall deprotonation. Comparing benzene$^{\bullet+}$, pyridine$^{\bullet+}$, pyridineH$^+$, 2-F pyridine$^{\bullet+}$ and 2-FpyridineH$^+$ with water vapor, we note that the deprotonation energies of the reactive sites differ only by about 10 kcal/mol yet the reactivates are different. Intra-cluster proton transfer and overall deprotonation therefore seem to be strongly sensitive to the deprotonation energies of the core ions, and to energy barriers and structural effects.

Similar to pyridine$^{\bullet+}$, the heteroatoms are protonated in the distonic, but not in the conventional, ions of other nitrogen and oxygen heterocyclics, of tertiary amines, and of

aldehydes, ketones and ethers. These distonic ions should also form strong ionic hydrogen bonds. These strong hydrogen bonds can affect their chemistry and can be used, as in the present case, to identify the distonic structures.

CHAPTER 4: Solvation of small molecules in the gas phase; Example of the Hydronium ion, H_3O^+

4.1 Introduction

The hydronium ion plays central roles in aqueous solutions, where it interacts with solutes, including dissolved gases. Such interactions also occur in ionized planetary atmospheres and in interstellar clouds where H_3O^+ ions can interact with major gas components such as hydrogen, nitrogen and carbon monoxide [95].

The thermochemistry of the bonding of H_3O^+ to small gaseous molecules is needed to model these interactions. However, few data are available on the bonding energies of H_3O^+ to common gases[86]. The reported cluster binding energies are generally small, with reported bond dissociation enthalpies (kcal mol^{-1}) and entropies (cal mol^{-1} K^{-1}) of; H_2, 3.5±05; (ΔS unreported)[96]; CO_2, 14.6, 20.7 [97] , 15.3, 24.6 [98]; N_2O, 16.9, 27.0[86].

4.2 Clustering reaction of H_3O^+ with small molecules

Water vapor (Aldrich, HPLC grade) was ionized by electron impact. The resulting H_2O^+ ions were mass selected and injected with injection energies of 5-20 eV (laboratory frame) in 5-15 μs pulses into the drift cell, where they were converted to H_3O^+ by reactions with trace water. The equilibrium studies were performed in 0.5 Torr of neat H_2, N_2 and CO gases. The reaction products were identified by scanning the second quadrupole mass filter located coaxially beyond the drift cell. The arrival time distributions (ATDs) were collected by monitoring the intensity of each ion as a function

of time after the injection. Equilibrium among the ions was demonstrated by the identical ATD peaks of the reactant H_3O^+ and products $H_3O^+(X)_n$ ions.

To further insure that the equilibrium was achieved, we varied the residence time of the ions inside the drift cell by varying the cell voltage. The test experiments at 302 K confirmed that the ion ratios remained constant independent of reaction time. These results also showed that the measured equilibrium constant is independent of the applied field across the drift cell in the low field region. The equilibrium experiments were conducted at low drift cell fields (30 V) and long residence times (1.34 ms).

Equilibrium constants were calculated from Eq. (1), where the ion intensities were obtained from the integrated peak areas of the ATDs and P(X) is the partial pressure of the gas X inside the cell (in atm, referred to standard state of 1 atm).

$$K_{eq} = I[H_3O^+(X)_n] / I[H_3O^+(X)_{n-1}] \, P(X) \quad (1)$$

The equilibrium constant measured as a function of temperature yields ΔH^o and ΔS^o from the van't Hoff equation [$\ln K = -\Delta H^o/RT + \Delta S^o/R$]. All of the experiments were reproduced in triplicate.

4.2.1 Solvation of the H_3O^+ ion with H_2 molecules

The mass spectra, in Figure 32, collected after the injection of the hydronium ion H_3O^+ into the drift cell containing 0.5 Torr of pure H_2 (ultrahigh purity, Spectra Gases 99.999%) shows at -104 ^{o}C only one peak at 19 amu corresponding to the reactant hydronium ion $H_3O^{\bullet+}$ When the temperature is decreased to -129 ^{o}C, the addition of one H_2 molecule on the hydronium ion $H_3O^+(H_2)$ become observable by the peak at mass 21 amu. The intensity of this peak increases as the drift cell temperature decreases (T = -136

^{o}C). At a lower temperature, -146 ^{o}C, the mass spectra shows the presence of a third peak at 23 amu corresponding to the clustering of second H_2 molecule on the hydronium ion $H_3O^+(H_2)_2$.
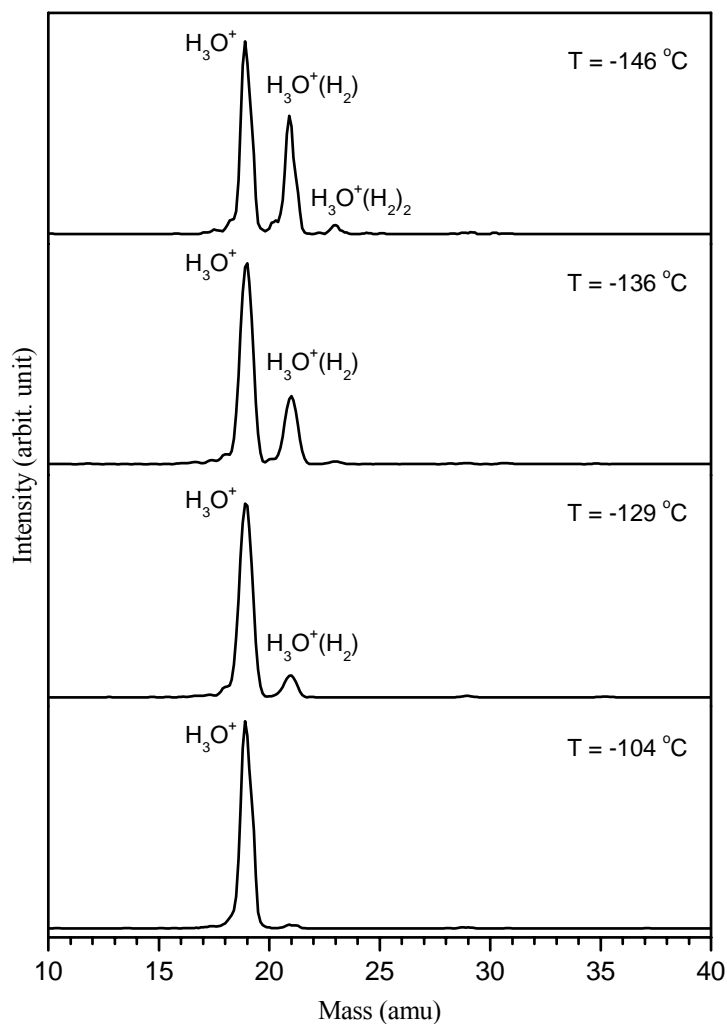
Figure 35: Typical mass spectra collected at different drift cell temperatures. The stepwise clustering of the H_2 molecules around the hydronium ion H_3O^+ is clearly observed as the temperature is decreased from -104°C to -146 °C.

The equilibrium conditions between the hydronium ion H_3O^+ and the sequential additions of the hydrogen molecules are fulfilled and Figure 36 shows the equal ATDs of the ions H_3O^+, $H_3O^+(H_2)$ and $H_3O^+(H_2)_2$. The equal ATDs of the reactant and product ions can be explained based on the ions' residence time. The reactant ion spend half of the time inside the drift cell as a reactant H_3O^+ and the other half of the time as a product $H_3O^+(H_2)_n$, because of the equilibrium existing between both ions.

Once the equilibrium is established, an equilibrium constant is measured between the reactant $H_3O^+(H_2)_{n-1}$ and the product $H_3O^+(H_2)_n$ ions and this is achieved by collecting their intensities at constant drift cell temperature and pressure which is proportional to the area under the ATD peaks, then the drift cell temperature is changed, and another equilibrium constant is collected. Within a range of drift cell temperature, a van't Hoff plots are generated (Figure 37) for the addition of hydrogen molecules on the hydronium ion. The binding energy of the association reaction is given by the slope of the van't Hoff plot and the entropy is given by the intercept with y axis.
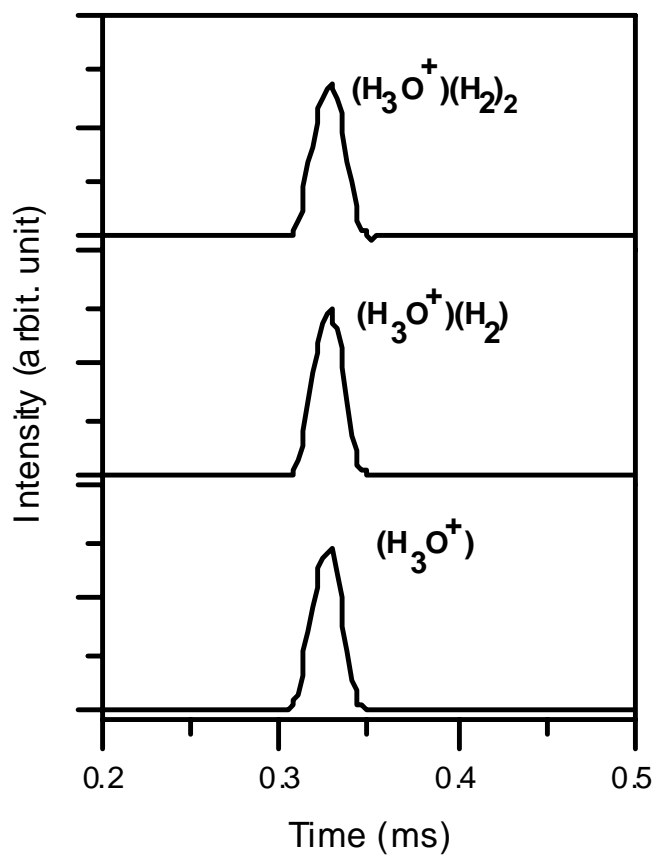
Figure 36: ATDs of the reactant H_3O^+ ion and the product ions corresponding to the addition of one and two H_2 molecules. Equal arrival time is clearly observed.
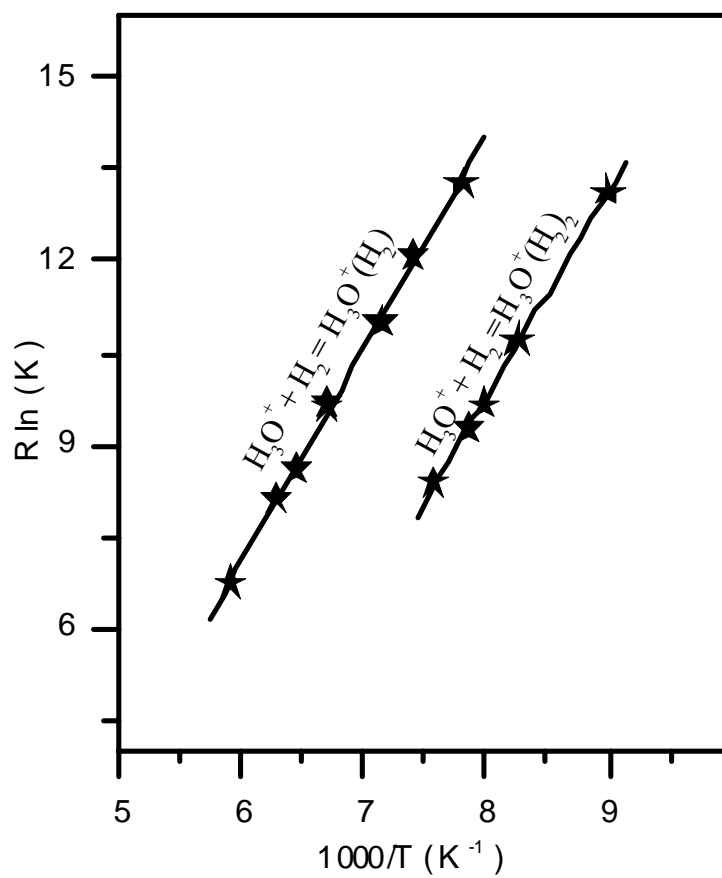
Figure 37: Generated van't Hoff plots for the equilibrium $H_3O^+(H_2)_{n-1} + H_2 = H_3O^+(H_2)_n$ where n equals 1 and 2.

The experimental value of the binding energy of the first hydrogen molecule on the hydronium ion $H_3O^+(H_2)$, is found to be small and only -3.4 kcal.mol^{-1} and the entropy of the reaction is -13.8 cal.mol-1.K-1. This value is in agreement with the -3.5 kcal.mol^{-1} reported by M. Okomura[96] using the vibrational predissociation spectroscopy technique. The second hydrogen molecule on the hydronium ion $H_3O^+(H_2)_2$, binds with similar strength (-3.5 kcal.mol^{-1}), and this can be attributed to the weak interactions between the hydronium ion H_3O^+ and the Hydrogen molecules H_2. On the other hand, this small value can be acceptable within the experimental error. Within the temperature limit the observation of higher cluster was unachievable; also the technical limit of measuring weak binding energy (less than 3 kcal.mol^{-1}) makes it difficult to report binding energy of higher clusters. It is notable that after the addition of the second hydrogen molecule the entropy drops to -17.3 cal.mol^{-1}.K^{-1}.

Theoretical calculations at four different levels were done using GAUSSIAN03 software. The calculated binding energies reported here were corrected for the unscaled-ZPE and BSSE (basis set superposition error). The BSSE was calculated utilizing the Counterpoise method as implemented in GAUSSIAN03. The results of the Calculations for the addition of H_2 molecules on the hydronium ion H_3O^+ are summarized in table 8. The experimentally measured values of the binding energies of the first two hydrogen molecules on the hydronium ion H_3O^+ ion find a good agreement with the calculations done at the B3LYP/6-311++G** level, 3.5 and 3.0 kcal.mol^{-1} respectively. The theoretical binding energy of the third hydrogen molecule is found to be 2.6 kcal.mol^{-1}. Calculations done at the MP2//ROHF/6-31+G**, MP2/6-31+G** and MP2/6-311++G**

shows a smaller binding energies of the hydrogen molecules on the hydronium ion compared to the experimental values.

Table 8: Calculated binding energies (kcal/mol) of $H_3O^{\bullet+}(H_2)_n$ at various levels.

n	MP2//ROHF/6-31+G**	MP2/ 6-31+G**	MP2/6-311++G**	B3LYP/6-311++G**	Experimental value
1	-1.0	-0.8	-1.9	-3.5	-3.4
2	-0.9	-0.7	-1.7	-3.0	-3.5
3	-0.9	-0.8	-1.65	-2.6	

The proposed structures for the clustering of the hydrogen molecules on the hydronium ion are presented in Figure 37. The binding of the first H_2 molecule on the hydronium ion H_3O^+ shows that the H-atoms of the hydrogen molecule has a fractional positive charges of 0.09 C and 0.07 C and they are both at 1.592 Å from one of the H-atom of the hydronium ion which has a fractional positive charge of 0.18 C. The oxygen atom carries a partial negative charge of – 0.13 C and the other two H-atoms of the hydronium ion hold an equal positive charge of 0.39 C. The structure of the hydronium ion with two hydrogen molecules $H_3O^+(H_2)_2$ shows that each H_2 molecule forms a bond with one of the H-atoms of the hydronium ion. Similar to the first addition, the charges on the H-atoms of the hydrogen molecules are 0.09 and 0.07 but with longer bond length, 1.634 Å. The charge on the oxygen atom becomes less negative (-0.07 C) and the two binding H-atoms of the hydronium carry an equal positive fractional charge of 0.19 C where the third free H-atom maintains a charge of 0.39 C, which is not affected by the addition of the second ligand.

Finally, the structure of the hydronium ion with three H_2 molecules $H_3O^+(H_2)_3$ shows the formation of three identical bonds between each one of the hydrogen atoms of the hydronium ion and the three H_2 molecules with a bond length equal to 1.670 Å. The H-atoms of the ion has the same positive charge (0.19 C), the charges on the H-atoms of the H_2 molecules are 0.06 and 0.08 C and atom with higher charge (0.08 C) is found closer to the core ion. The oxygen atom becomes neutral. It is notable that the total charge is conserved on the core ion and not well dispersed between all the atoms in the

complex structure, and this behavior is not perturbed by the increase of the ligands around the ion.
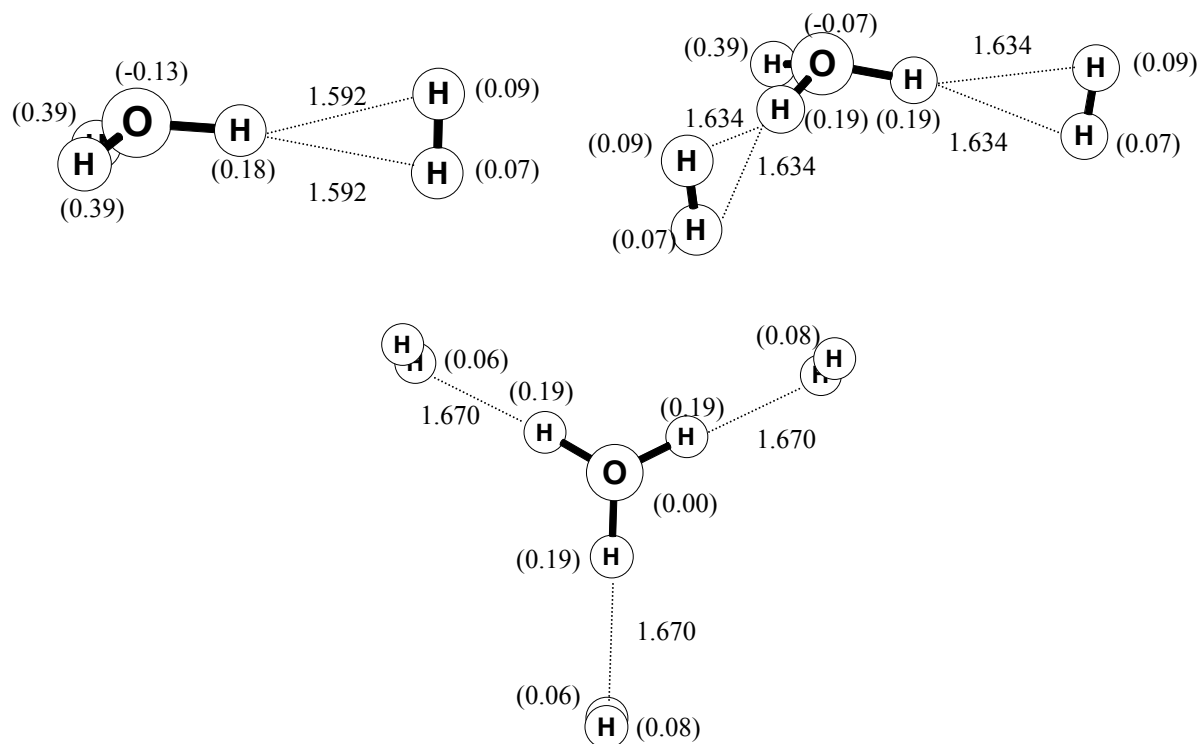
Figure 38: Optimized structures of $H_3O^+(H_2)_{1-3}$ at B3LYP/6-311++G** level. Bond lengths are in Angstroms while the molecular charges are shown in bold and atomic charges are shown in parenthesis.

4.2.2 Solvation of the H_3O^+ ion with N_2 molecules

The interactions of the hydronium ion H_3O^+ with the nitrogen molecules N_2, was studied by the injection of the mass selected ion H_3O^+ into the drift cell filled with pure nitrogen gas (high purity, Spectra Gases 99.9%). The cell pressure was maintained constant at 0.5 Torr. Up to the high number of collisions inside the drift cell, products were formed as a result of the reaction between the hydronium ion H_3O^+ and the nitrogen molecules N_2. The collected scans at different drift cell temperatures, Figure 39, show at -10 ^{o}C the presence of peaks corresponding to the hydronium ion H_3O^+, H_3O^+ with one nitrogen molecule, $H_3O^+(N_2)$, a protonated nitrogen dimer $H^+(N_2)_2$ at mass 57 amu and peaks at 37 and 55 amu for the protonated water dimer $H^+(H_2O)_2$ and trimer $H^+(H_2O)_3$ cluster ions resulting from the reaction of the hydronium ion H_3O^+ with water H_2O existing as impurity in the nitrogen gas. As the drift cell temperature is decreased from -10 ^{o}C to -30 ^{o}C the intensity of the reactant ion H_3O^+ decreases and a peak corresponding to the addition of two nitrogen molecules on the hydronium ion, $H_3O^+(N_2)_2$ starts to appear with almost no change on the intensity of the protonated ions. When the drift cell temperature is decreased to -60 ^{o}C, a peak for the addition of a third nitrogen molecule, $H_3O^+(N_2)_3$ is observed with small intensity. At the lowest temperature -110 ^{o}C, the intensities of the higher clusters $H_3O^+(N_2)_n$, n = 2-3, increased and the hydronium ion peak disappeared. When the water (impurity) inside the drift cell become frozen at -110 ^{o}C its vapor pressure is decreased and its reaction with the hydronium ion become very weak, this can explain the absence of the peaks corresponding to the protonated water clusters.
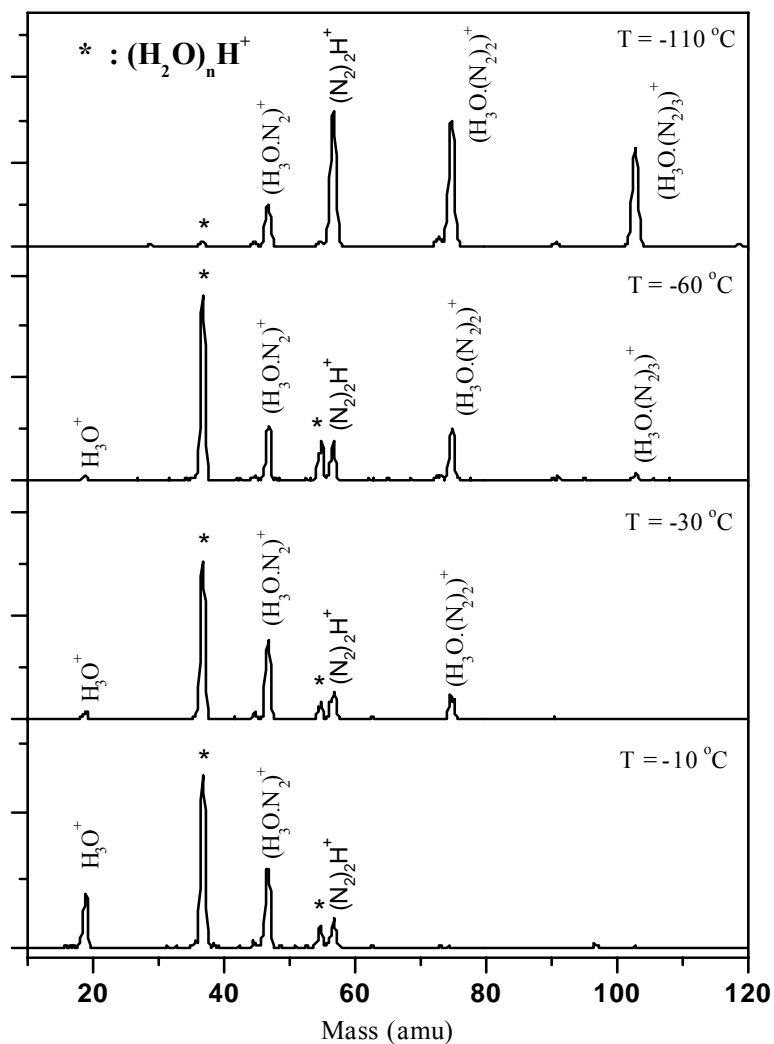
Figure 39: Mass spectra collected following the injection of H_3O^+ into the drift cell filled with 0.5 Torr of pure N_2 gas. With the clustering of N_2 on the H_3O^+ ion, the presence of the $(N_2)_2H^+$ and protonated water cluster ions are observed.

The reaction between the hydronium ion and the nitrogen molecules is quickly established inside the drift cell upon the high number of collisions. Tests for the equilibrium between the reactant H_3O^+ and product ions $H_3O^+(N_2)_n$ were completed, and Figure 39 shows the equal ATDs of these ions. Once the equilibrium conditions were fulfilled, measurements of the binding energy of the nitrogen molecules N_2 to the hydronium ion H_3O^+ can take place. The van't Hoff plots are generated by collecting equilibrium constant at different drift cell temperatures and plotting $Rln(K)$ as a function of $1000/T$.

Figure 40 point up the van't Hoff plots of the sequential addition of three nitrogen molecules on the hydronium ion. Where the binding energy of the first N_2 molecule on the hydronium ion H_3O^+ is found to be -7.9 kcal.mol^{-1} and the entropy of the reaction is -14.8 cal.mol^{-1}.K^{-1}. The addition of the second nitrogen molecule shows a decrease in the binding energy value by one kcal.mol^{-1} and an increase in the entropy of the reaction (-20.0 cal.mol^{-1}.K^{-1}). This decrease in the binding energy value is also observed with addition of the third N_2 molecule where the binding energy is -5.4 kcal.mol^{-1} and the entropy of the reaction is -17.6 cal.mol^{-1}.K^{-1}.

Theoretical calculations are conducted at diverse levels for the investigation of the stepwise clustering of nitrogen molecules N_2 on the hydronium ion H_3O^+ and the structures of the resulting products. Results are summarized in **Table 10**. Within the four levels used in this calculations, the agreement between the theory and the experiment is obvious except with the B3LYP/6-311++G** level where the results are about one kcal.mol^{-1} higher.
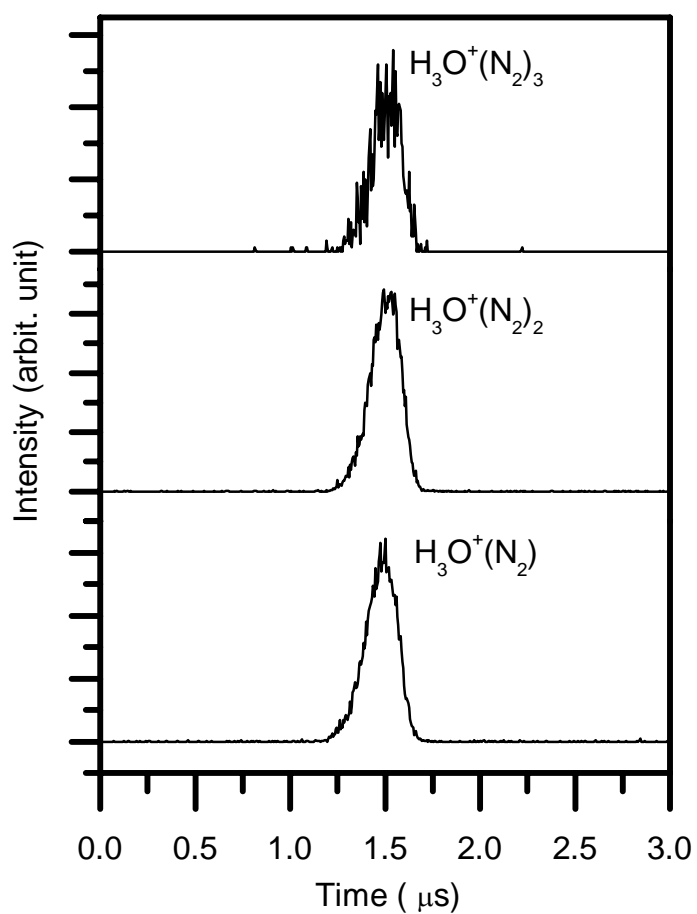
Figure 40: ATDs $H_3O^+(N_2)_n$, n = 1-3 collected at -110 ^{o}C, test of equilibrium condition is fulfilled with the equal arrival time of all the ions.
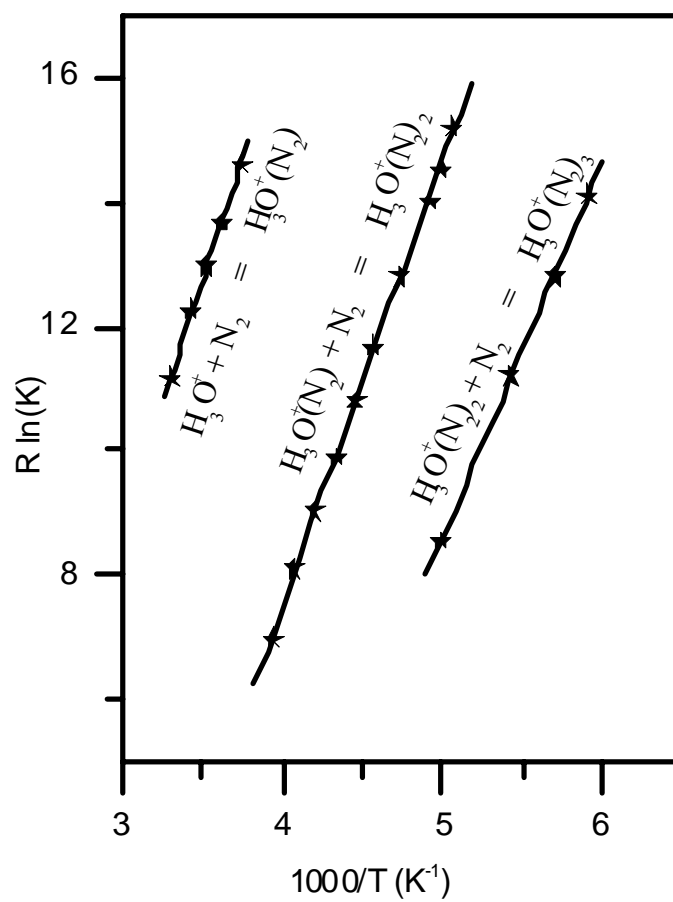
Figure 41: van't Hoff plots for the sequential clustering of three nitrogen molecules on the hydronium ion.

Table 9: Experimentally measured binding energies of $H_3O^{\bullet+}(N_2)_n$, n = 1-3 in kcal.mol-1 and entropies in cal.mol-1.K-1.

n	$H_3O^+(N_2)_n$	
	ΔH^o	ΔS^o
1	-7.9	-14.8
2	-6.9	-20.0
3	-5.4	-17.6

Table 10: Calculated binding energies (kcal.mol^{-1}) of $H_3O^{\bullet+}(N_2)_n$ at various levels.

n	MP2//ROHF/6-31+G**	MP2/6-31+G**	MP2/6-311++G**	B3LYP/6-311++G**
1	-7.6	-7.8	-8.4	-9.6
2	-6.5	-6.6	-7.1	-7.7
3	-6.0	-6.0	-6.4	-6.6
4	-2.6			

The optimized structures for the products formed by the clustering of nitrogen molecules on the hydronium ion are presented in Figure 42. For the addition of the first N_2 molecule, the nitrogen atoms enclose opposite charges. The negatively charged one (-0.08 C) is the binding one and it is oriented in the direction of one of H-atom of the hydronium ion with a bond length of 1.670 Å. The second one, with a positive charge of 0.03 C is in linear direction with the H···N complex. The binding H-atom of the hydronium carries higher charge (0.63 C) than the other two H-atoms (0.39 C) and the oxygen atom fractional charge is negative (- 0.35 C). The second N_2 molecule is oriented toward the second H-atom of the hydronium. The charge of the new binding nitrogen molecule is increased to -0.07 C and the bond length in the presence of two nitrogen molecule is increased and it is 1.745 Å for both bonds. The negative charge on the oxygen atom is to some extent decreased to -0.46 C. When the third N_2 molecule comes in place, all three H-atoms of the hydronium are identical with partial positive charges of 0.54 C. The binding nitrogen molecules carry similar negative charges of - 0.06 C and form three identical bonds with a length of 1.798 Å.

When the number of nitrogen molecules bonded to the hydronium ion is increased, the fractional charges on the binding H-atoms are decreased, and the negative charge on the binding N-atoms is increased. The resulting stretched bond length is coming from the dispersion of the total charge between all the atoms and this can direct to a weak interaction forces between the ion and the N_2 molecules. The decrease in the intermolecular forces is experimentally observed when the binding energy of one

nitrogen molecule is be -7.9 kcal.mol^{-1} and the energy is only -5.4 kcal.mol^{-1} when three

nitrogen molecules are present.
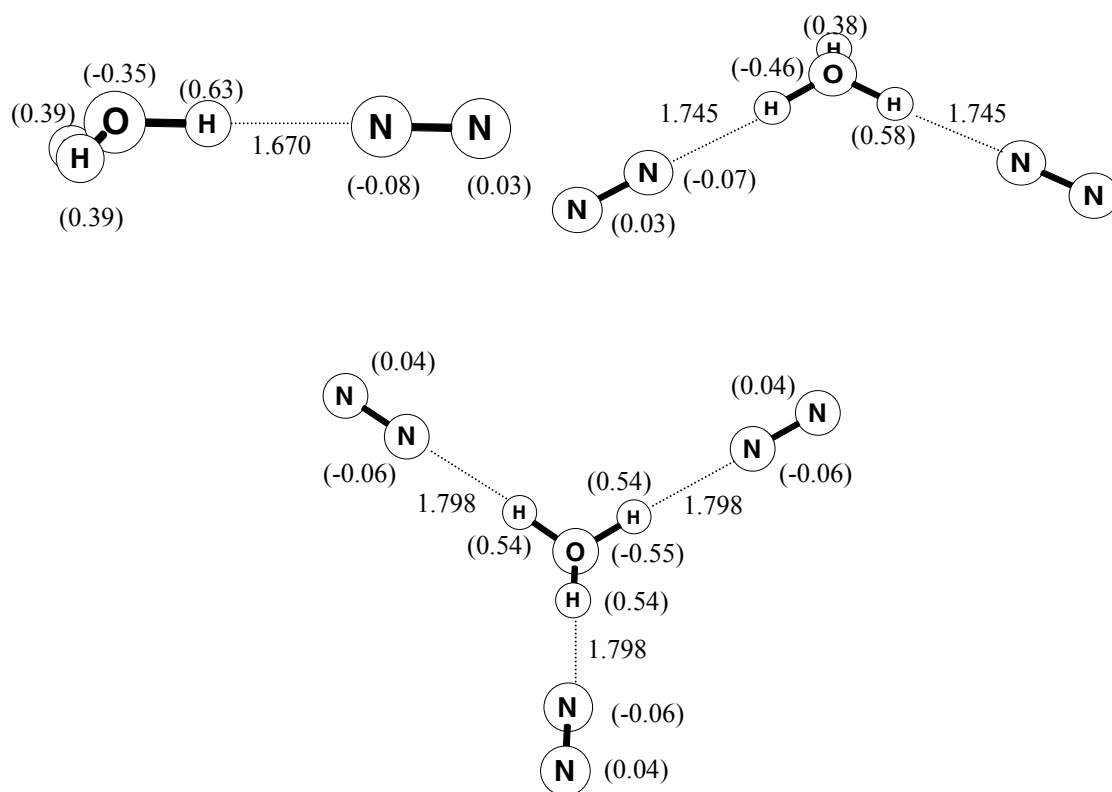
Figure 42: Optimized structures of $H_3O^+(N_2)_{1-3}$ at B3LYP/6-311++G** level. Bond lengths are in Angstroms while the molecular charges are shown in bold and atomic charges are shown in parentheses.

4.2.3 Solvation of the H_3O^+ ion with CO molecules

The interactions between the CO molecules and the hydronium ion H_3O^+ are investigated. The mass selected ion was injected into the drift cell filled with pure CO gas (high purity, Spectra Gases 99.9%). Upon the collisions with the CO molecules escaping from the drift cell entrance pinhole, the Hydronium ion is quickly thermalized and reactions with the CO molecules inside the drift cell can take place. Collected mass spectrum at different temperatures shows the stepwise clustering of CO molecules on the hydronium ion. Once equilibrium tests are completed (pressure, rate constant and the equal ATDs of the ions figure 43), the drift cell pressure and temperature are maintained constant and equilibrium constant is collected. The controllable drift cell temperature makes it easy to generate van't Hoff plots for the reactions of CO molecules and the hydronium ion, figure 43. The CO molecules are found to be strongly bonded to the hydronium ion than the H_2 or N_2 ligands. Experimental binding energy of the first CO molecule is -11.5 kcal.mol^{-1} and the entropy of the reaction is -18.6 cal.mol^{-1}.K^{-1}, when the second CO molecule is added, the binding energy value become -9.8 kcal.mol^{-1} and the entropy is -23.8 cal.mol^{-1}.K^{-1}, the third CO molecule bound with -8.6 kcal.mol^{-1} and an entropy of -27.4 cal.mol^{-1}.K^{-1}.
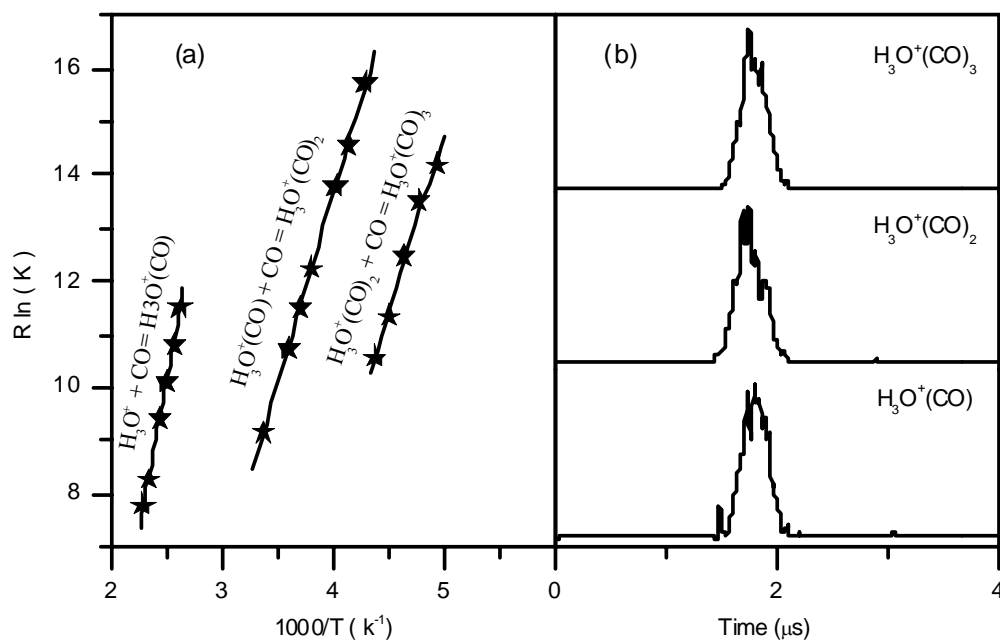
Figure 43: (a) van't Hoff plots for the equilibrium reaction $H_3O^+(CO)_{n-1}$ + CO = $H_3O^+(CO)_n$, n = 1-3 and (b) the ATDs of the equilibrated ions.

Theoretical calculations are done at different levels for the binding energy values of CO molecules on the hydronium ion. The CO molecule can form a Hydrogen bond with the Hydrogen atom of the hydronium ion using the carbon atom to form H_2O-$H^{+\cdots}C$-O or the oxygen atom to form H_2O- $H^{+\cdots}O$-C. Calculations are done for both possibilities and the bond formed by the carbon site is stronger than the one formed with the oxygen atom and in good agreement with the experimental values. The calculated energies for the formation of H-bond between the H-atoms of the hydronium and the oxygen atom of the CO molecules are found to be smaller than the experimental values by 3 to 5 $kcal.mol^{-1}$. Similar to the N_2 ligands, when the number of CO molecules bonded to the ion increases, the charge become more dispersed between all the atoms and the interaction becomes weaker. The calculated binding energy for the addition of the fourth CO molecule on the hydronium ion shows a significant drop from -8.1 to -2.3 $kcal.mol^{-1}$, this can be explained by the formation of a complete shell around the core ion and the fourth molecule is in a second shell and it is shielded from the charge which may lead to a weak interactions and therefore weak binding energy.

Structures of the formed clusters are optimized and they are shown in Figure 44.

Table 11: Calculated binding energies (kcal/mol) of $H_3O^{\bullet+}(CO)_n$ at various levels.

n		MP2//ROHF/6-31+G**	MP2/ 6-31+G**	MP2/6-311++G**	B3LYP/6-311++G**	Experimental value
1	CO	-11.8	-13.3	-14.0	-14.7	-11.5
	OC	-6.4	-5.8	-5.3	-8.2	
2	CO	-9.4	-9.9	-10.2	-10.2	-9.8
	OC	-5.6	-5.2	-4.8	-6.8	
3	CO	-8.1	-8.5	-8.8	-8.5	-8.6
	OC	-5.2	-4.8	-4.5	-6.1	
4	CO	-2.3				
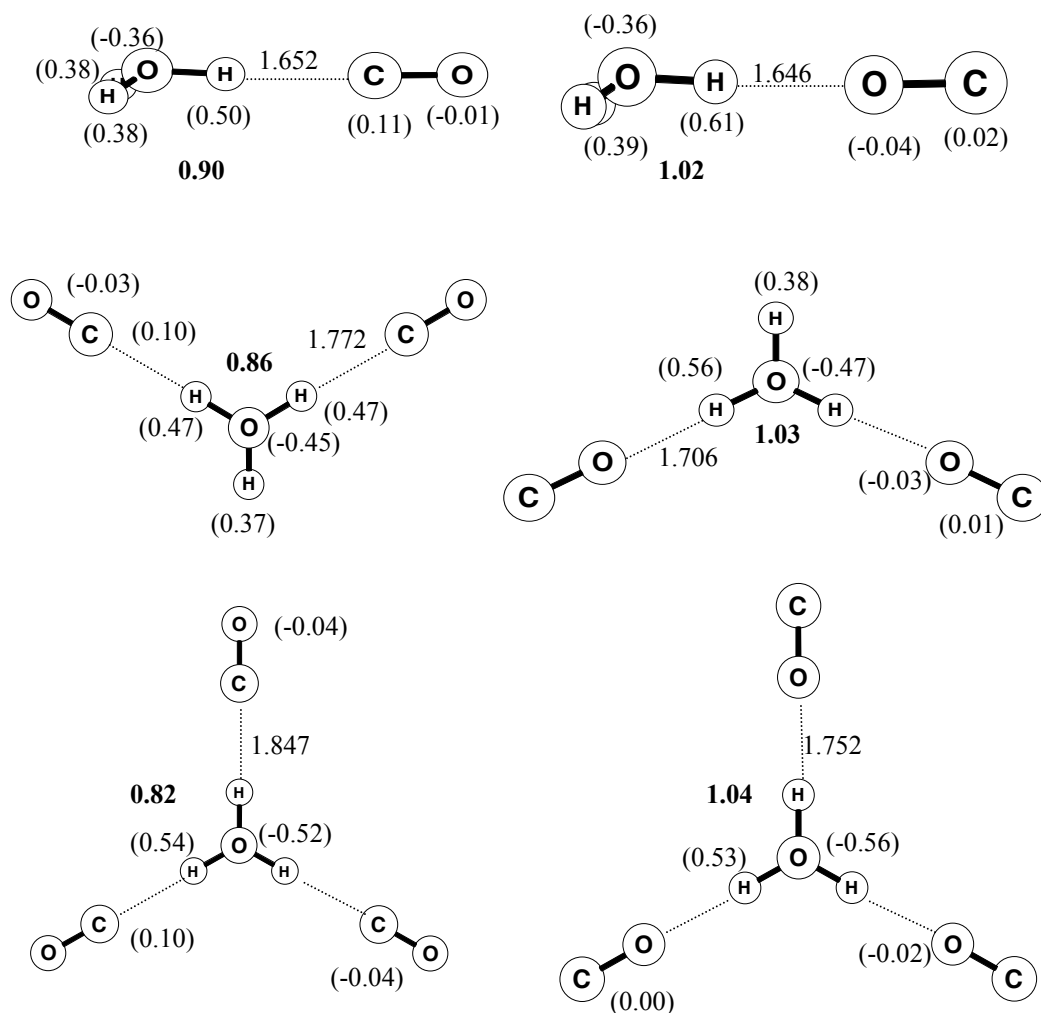
Figure 44: Optimized structures of $H_3O^+(CO)_{1-3}$ and $H_3O^+(OC)_{1-3}$ at B3LYP/6-311++G** level. Bond lengths are in Angstroms while the molecular charges are shown in bold and atomic charges are shown in parentheses.

To address the binding of CO with H_3O+ in more detail, a potential-energy surface scan was generated by varying the C⋯H bond length (in 0.05 Å step size) and the OCH angle (in 1o step size) and calculating the energy at each step. The starting geometry was that for optimized H_2OH^+⋯CO and final geometry was for H_2OH^+⋯OC at B3LYP/6-311++G** level. The energy for the final product differed from that obtained by geometry optimization of H_2OH^+⋯OC at B3LYP/6-311++G** by ~2 kcal/mol. This difference comes from the small difference in the OCHO dihedral angle between the two structures. The resulting potential energy surface in Figure 45, predicts a barrier of 18.6 kcal/mol for the inversion of H_2OH^+⋯CO to the H_2OH^+⋯OC isomer.

A more interesting feature of this system is the addition of one CO molecule on the hydronium ion H_3O^+ for a complex with binding energy of -11.5 kcal.mol^{-1}, with the same structure for the protonated formic acid H^+(HCOOH). Using tabulated thermochemistry data[86], the formation energy of the protonated formic acid from the addition of CO molecule on the hydronium ion is found to be -18.4 kcal.mol^{-1} which is more exothermic than the measured value. Clearly the formed product is not covalently bonded. On the other hand the entropy of the covalent association is usually between -40 and -60 cal.mol^{-1}.K^{-1} and the observed one is only -18.6 cal.mol^{-1}.K^{-1}.
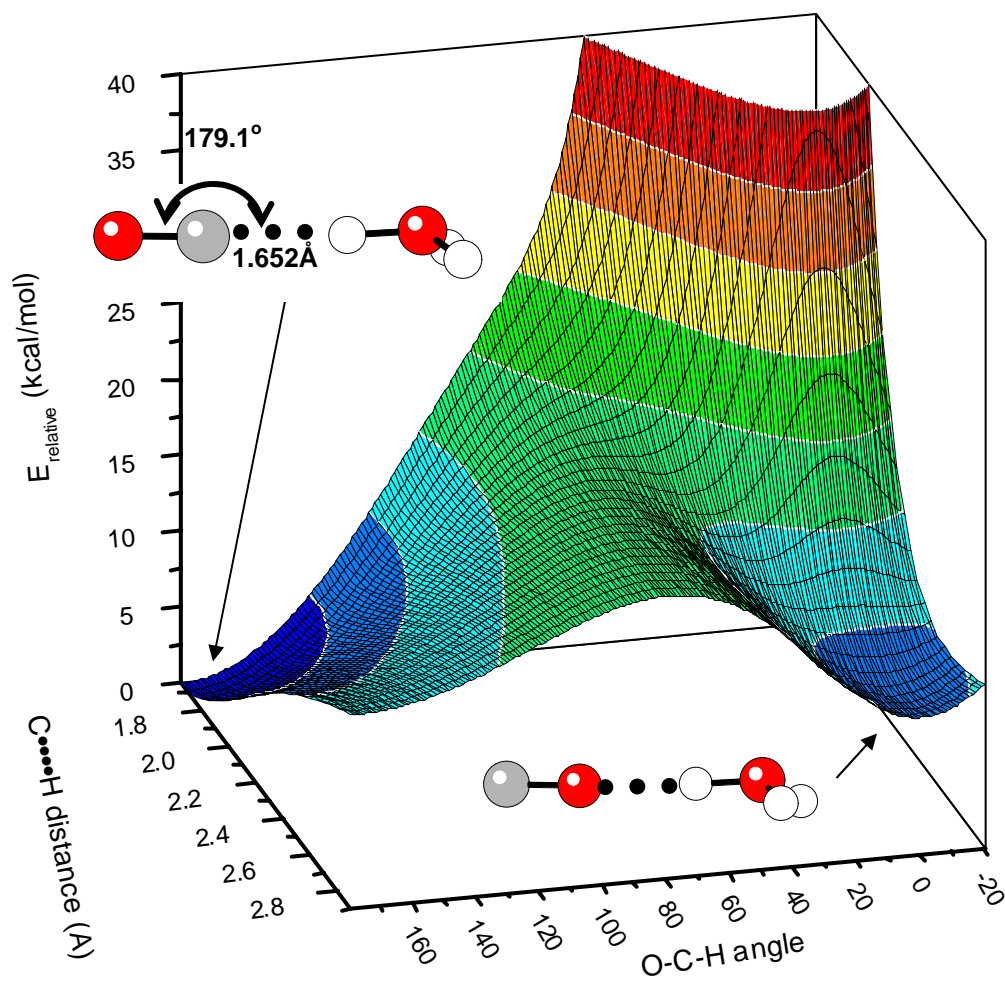
Figure 45: Potential-energy surface scan for the inversion of CO molecule in $H_3O^{\bullet+}CO$ complex. The scan was done at B3LYP/6-311++G** level of theory

4.3 Conclusions

The binding energies of one and two hydrogen molecules on the hydronium ion are experimentally measured and their values did not show a large difference -3.4 and -3.5 kcal.mol^{-1} and this can be attributed to the weak interactions. Theoretical calculations are conducted at four different levels, and it appears that at high level of electron correlation as in B3LYP/6-311++G** calculations may be needed to capture most of the details of the interactions between weakly binding hydrogen molecules and the H_3O^+ ion. For the N_2 and CO the experimental values show a small decrease in the stepwise clustering energies for each set and this is a result of the large mutual effect of the consecutive ligands. The high levels of electron correlation gives a high binding energy values and the experimetal values find the good agreement with the MP2//ROHF/6-31+G** level. In all three sets of ligands, the total charge is conserved with the core ion and the ligands effects are minor. For instance, when one or two H-atom of the hydronium ion remains unbonded they hold a charge of 0.37 to 0.39. However, the ligand molecules show some mutual steric interference as the entropy change when adding the second molecule is larger than the first one for all of the three sets.

The binding of CO by the carbon site to the H_3O^+ ion is found to be stranger than binding with the oxygen atom. Even the negative part of the ligand's dipole is closer to the H-atom and this can be dependent on the high proton affinity of the CO at the carbon atom (142 kcal.mol^{-1}) verses the one at the oxygen atom (102 kcal.mol^{-1}).[86] A covalent contribution to the $-H^{+\cdots}CO$ may be after the stranger binding in $H_2OH^{+\cdots}CO$. Similar

effects were observed in hydrogen bonded complexes of isocyanides verses cyanides with protonated amines, $R_3NH^{+\cdots}CNR$ vs. $R_3NH^{+\cdots}NCR$. The sp carbon lone pairs are involved in both of these clusters and the present $H_2OH^{+\cdots}CO$ complexes to ease the covalent contribution to the formed hydrogen bond[99].

The $H_2OH^{+\cdots}CO$ is a non-covalent isomer of the protonated formic acid $(HCOOH)H^+$, because the measured binding energy (-11.5 kcal.mol^{-1}) is smaller than the covalent association of H_3O^+ to CO which is bring into being -18.4 kcal.mol^{-1} in addition to the measured entropy (-18.6 cal.mol^{-1}.K^{-1}) which is less than the -40 to -60 cal.mol^{-1}.K^{-1} found in the covalent association reactions. This system is of fundamental interest because H_2, N_2, CO and H_3O^+ are major species in the interstellar cloud[100], in addition to the possibilities of the interstellar ion-molecule reaction which can guide to the formation of the observed clusters.

CHAPTER 5: Conclusions

In this work, the ion mobility mass spectrometry technique was used in its three possible ways, where mobility measurements, thermochemical measurements and kinetics measurements were conducted for different systems. The thermochemistry measurements were investigated in the $C_3H_3^+$ /water system where the binding energies of water molecules to the $C_3H_3^+$ ion are measured. The water was found to form stronger hydrogen bond with $C_3H_3^+$ than the one found with the benzene radical cation and this was attributed to the more localized charge in the smaller size ion. The strong ion-molecule interaction was extended to the polar acetonitrile ligands where the difference is about 2-3 kcal/mol. The electrostatic interactions between the pyridine cation and water molecules were examined and the measured binding energies provide evidence for the identification of distonic ions. The theoretical calculations supported the proposed structure of the distonic pyridine cation in the presence of water molecules by showing different values for the binding energies of water molecules to the conventional pyridine cation. The substitution of hydrogen atom by a fluorine atom in the pyridine structure did not alter the distonic property. The previously measured benzene/water binding energies were used here for the comparison because in the benzene/water system the only type of hydrogen bonds can be found is the carbon based one C-H$^{\cdots}$OH$_2$ and the strength of these bonds (8-10 kcal/mol) was not found in the pyridine/water system. The ion mobility system was used for the measurements of the binding energy of small molecules to the hydronium ion H_3O^+

In the Hydronium ion system, the ion-molecule interactions were examined for three different molecules with different properties. The size differences were investigated by measuring the binding energy to the hydrogen and nitrogen molecules. The binding energy can be increased when the polarizability is increased, and this was found in the comparison of the hydrogen to the nitrogen molecules (0.79 to 1.76 respectively). The binding energies show differences greater than 4 kcal/mol. The contribution of the dipole moment ($\mu = 0.11$ for CO) to the interaction is remarkable and the binding energy of the CO molecule to the hydronium ion is found to be more than 11 kcal/mol. In each set of these three ligands the binding energy is found to have a sharp drop after the addition of the third ligand, and this is due to the completion of the first solvation shell with the three equivalent hydrogen atoms of the hydronium ion.

The ion mobility system can be used as a tool for the structure investigation of organic molecules in the gas phase by measuring the collision cross-section of an ion traveling through the drift cell and comparing it to a calculated values for a known structure isomers. The structure of the $C_3H_3^+$ ion generated by the EI ionization was investigated. The mobility of the ion was compared to the theoretically calculated ones for the linear and cyclic isomers and the generated one was found to be cyclic. Also in the study of the cationic polymerization of isoprene and limonene in the gas phase, the mobility measurements were used. The formation of covalently bounded complex from cluster ions was examined and the measured collision cross-sections for the isoprene dimer cation were found to be exactly the same as the one measured for the limonene cation.

The kinetics of a chemical reaction can be studied by our ion mobility technique by inspecting the reaction inside the drift cell. The residence time of an ion inside the drift cell can be controlled by changing the drift cell voltage and this can give control to the reaction happening inside the drift cell. These kinds of experiments were achieved in our laboratory where the rate constant of a pseudo-first order reaction can be measured.

The kinetics measurements were done for the deprotonation of the $C_3H_3^+$ cation by assembled water molecules to form the protonated water clusters. This deprotonation reaction was also studied for the benzene/water system and the results were found to be the same in both systems. The measured activation energy for the deprotonation of these ions was found to be -37 ± 1 kcal/mol.

Literature Cited

1. Mabrouki, R., et al., - *Gas phase hydration and deprotonation of the cyclic C3H3(+) cation. Solvation by acetonitrile, and comparison with the benzene radical cation.* 2006. **- 110**(- 23).

2. Ibrahim, Y.; Ridha M., Meot-Ner, M.; El-Shall*, M. S. J. Phys. Chem. A 2007, 111, 1006-1014.

3. Hayhurst, A.N. and H.R.N. Jones, - *Chemi-Ionization in Oxyacetylene Flames.* 1982. **- 296**(- 5852).

4. Gerlich, D. and S. Horning, - *Experimental Investigations of Radiative Association Processes as Related to Interstellar Chemistry.* 1992. **- 92**(- 7).

5. Lopez, R., et al., - *An ab initio study of the reaction of propargyl cation with ammonia.* 2002. **- 106**(- 18).

6. Liu, G.X., et al., - *Water-assisted isomerization from linear propargylium (H2CCCH+) to cyclopropenylium (c-C3H3+).* 2002. **- 106**(- 43).

7. Herbst, E., et al., - *Association Reactions - Theoretical Shortcomings.* 1989. **- 85**.

8. Ibrahim, Y., et al., *Stepwise Hydration and Multibody Deprotonation with Steep Negative Temperature Dependence in the Benzene.bul.+-Water System. [Erratum to document cited in CA141:395073].* Journal of the American Chemical Society, 2005. **127**(11): p. 4114.

9. Ibrahim, Y., et al., *Stepwise Hydration and Multibody Deprotonation with Steep Negative Temperature Dependence in the Benzene.bul.+-Water System.* Journal of the American Chemical Society, 2004. **126**(40): p. 12766-12767.

10. Mabourki, R., et al., - *Clusters of the hydronium ion (H3O+) with H-2, N-2 and CO molecules.* 2006. **- 424**(- 4-6).

11. McDaniel, E.W. and D.W. Martin, *Mass spectrometric studies of mobilities, diffusion, and reactions of ions in gases.* 1971, Sch. Phys.,Georgia Inst. Tech.,Atlanta,GA,USA. FIELD URL:. p. 24 pp.

12. Bowers, M., *A Personal Retrospective of the Early Years.* Journal of the American Society for Mass Spectrometry, 2005. **16**(7): p. 984-988.

13. Mabrouki, R., E. Xie, and M.S. El-Shall, *Binding energies and structures of H3O+(X)n clusters, X=H2, N2 and CO.* Abstracts, 56th Southeast Regional Meeting of the American Chemical Society, Research Triangle Park, NC, United States, November 10-13, 2004: p. GEN-448.

14. Ibrahim, Y.M., et al., *Stepwise Hydration of Ionized Aromatics. Energies, Structures of the Hydrated Benzene Cation, and the Mechanism of Deprotonation Reactions.* Journal of the American Chemical Society, 2005. **127**(19): p. 7053-7064.

15. Momoh, P.O., et al., *- Polymerization of ionized acetylene clusters into covalent bonded ions: Evidence for the formation of benzene radical cation.* 2006. **- 128**(-38).

16. Alsharaeh, E., Y.M. Ibrahim, and M.S. El-Shall, *Initiation Mechanism and the Structures of the Early Oligomers in the Gas Phase Polymerization of Styrene.* Abstracts, 56th Southeast Regional Meeting of the American Chemical Society, Research Triangle Park, NC, United States, November 10-13, 2004: p. GEN-232.

17. Ibrahim, Y., et al., *- Stepwise hydration and multibody deprotonation with steep negative temperature dependence in the benzene(center dot+)-water system.* 2004. **- 126**(- 40).

18. McDaniel, E.W. and E.A. Mason, *The Mobility and Diffusion of Ions in Gases. (Wiley Series in Plasma Physics).* 1973. 384 pp.

19. Lindinger, W., et al., *Investigation of ion-molecule reactions using a drift tube with separated ion source.* International Journal of Mass Spectrometry and Ion Physics, 1979. **30**(3-4): p. 251-61.

20. Thomas, R., A. Barassin, and R.R. Burke, *Drift tube with selective introduction in a mass spectrometer for kinetic study of ion-molecule reactions.* International Journal of Mass Spectrometry and Ion Physics, 1978. **28**(3): p. 275-84.

21. Milloy, H.B. and M.T. Elford, *Mass discrimination in ion sampling from drift tubes.* International Journal of Mass Spectrometry and Ion Physics, 1975. **18**(1): p. 21-31.

22. Moruzzi, J.L. and L. Harrison, *Energy distributions of atomic and molecular oxygen(-) ions produced in drift tubes.* International Journal of Mass Spectrometry and Ion Physics, 1974. **13**(2): p. 163-71.

23. Long, J.W. and J.L. Franklin, *Ion-cluster reactions in a drift tube ion source.* International Journal of Mass Spectrometry and Ion Physics, 1973. **12**(5): p. 403-10.

24. Wong, S.F., T.V. Vorburger, and S.B. Woo, *Photodetachment of O3- in a drift tube.* Physical Review A: Atomic, Molecular, and Optical Physics, 1972. **[3]5**(6): p. 2598-604.

25. Ibrahim, Y., et al., *Separation of isomers by dimer formation: isomerically pure benzene+ and toluene+ ions, and their dimers: ab initio calculations on (benzene)2+.* Chemical Physics Letters, 2003. **380**(1,2): p. 21-28.

26. Hagen, D.F., *Characterization of isomeric compounds by gas and plasma chromatography.* Analytical Chemistry, 1979. **51**(7): p. 870-4.

27. Clemmer, D.E. and M.F. Jarrold, *Ion mobility measurements and their applications to clusters and biomolecules.* Journal of Mass Spectrometry, 1997. **32**(6): p. 577-592.

28. Kemper, P.R., M.T. Hsu, and M.T. Bowers, *Transition-metal ion-rare gas clusters: bond strengths and molecular parameters for Co+(He/Ne)n, Ni+(He/Ne)n, and Cr+(He/Ne/Ar).* Journal of Physical Chemistry, 1991. **95**(26): p. 10600-9.

29. Rusyniak, M.J., et al., *Gas-Phase Ion Mobilities and Structures of Benzene Cluster Cations (C6H6)n+, n = 2-6.* Journal of the American Chemical Society, 2003. **125**(39): p. 12001-12013.

30. El-Shall, M.S., et al., *Stepwise Hydration, and Multi-Body Deprotonation with Steep Negative Temperature Dependence, in the Benzene.+ - Water System.* Abstracts, 56th Southeast Regional Meeting of the American Chemical Society, Research Triangle Park, NC, United States, November 10-13, 2004: p. GEN-231.

31. Alsharaeh, E.H., Y.M. Ibrahim, and M.S. El-Shall, *Direct Evidence for the Gas Phase Thermal Polymerization of Styrene. Determination of the Initiation Mechanism and Structures of the Early Oligomers by Ion Mobility.* Journal of the American Chemical Society, 2005. **127**(17): p. 6164-6165.

32. Bowers, M.T. and Editor, *Gas Phase Ion Chemistry, Vol. 2*. 1979. 346 pp.

33. Keesee, R.G. and A.W. Castleman, Jr., *Photoabsorption and photoionization of clusters.* Studies in Physical and Theoretical Chemistry, 1990. **68**(At. Mol. Clusters): p. 507-50.

34. Rusyniak, M., et al., - *Mass-selected ion mobility studies of the isomerization of the benzene radical cation and binding energy of the benzene dimer cation. Separation of isomeric ions by dimer formation.* 2003. - **107**(- 38).

35. Pithawalla, Y.B., et al., *Comparative study of the binary clusters of acetic acid-water and acetic acid-benzene using electron impact and multiphoton ionization techniques.* International Journal of Mass Spectrometry, 2002. **218**(1): p. 49-62.

36. Calcote, H.F. and D.G. Keil, - *the Role of Ions in Soot Formation.* 1990. - **62**(- 5).

37. Hall-Roberts, V.J., et al., - *The origin of soot in flames: Is the nucleus an ion?* 2000. - **120**(- 4).

38. Cernicharo, J., et al., *Astronomical detection of propadienylidene (H2CCC).* Astrophysical Journal, 1991. **368**(2, Pt. 2): p. L39-L41.

39. Audier, H.E., et al., - *Unimolecular Decompositions of the Radical Cations of Ethylene-Glycol and Its Monomethyl Ether in the Gas-Phase - Distonic Ions Versus Ion Neutral Complexes.* 1992. - **114**(- 6).

40. Bouchoux, G., et al., *Rearrangement and dissociation of ionized 1,2-diaminoethane.* International Journal of Mass Spectrometry, 1998. **179/180**: p. 337-348.

41. Kiminkinen, L.K.M., K.G. Stirk, and H.I. Kenttamaa, - *a Remarkably Stable Organic Radical Cation - the Distonic Isomer of the Unstable Radical Cation of Dimethyl Propyl Phosphate.* 1992. - **114**(- 6).

42. Kenttamaa, H.I., - *Long-Lived Distonic Radical Cations.* 1994. - **29**(- 1).

43. Smith, R.L., et al., - *Organic Radical Cations Abstract Methylene from Ketene to Produce Stable Distonic Ions.* 1993. - **115**(- 22).

44. Lavorato, D., et al., - *Observation of the Hammick intermediate: Reduction of the pyridine-2-ylid ion in the gas phase.* 1996. - **118**(- 47).

45. Lavorato, D.J., et al., *Generation of neutral and cationic hydrogen shift isomers of pyridine: a combined experimental and computational investigation.* International Journal of Mass Spectrometry, 1998. **179/180**: p. 7-14.

46. Gerbaux, P., et al., - *Definitive characterization of some C5H5N.+ and C6H7N.+ radical cations by associative ion-molecule reactions.* 2001. - **206**(- 1-2).

47. Gerbaux, P., Y. VanHaverbeke, and R. Flammang, - *Ion-molecule reaction of pyridine with CS3 radical cations: Experimental evidence for the production of pyridine N-thioxide distonic ions.* 1997. - **32**(- 11).

48. Gerbaux, P., et al., - *Characterization of ionized heterocyclic carbenes by ion-molecule reactions.* 1999. - **13**(- 17).

49. Yu, S.J., et al., - *the Beta-Distonic Ion from the Reaction of Pyridine Radical-Cation and Ethene - a Demonstration of High-Pressure Trapping in Fourier-Transform Mass-Spectrometry.* 1993. - **115**(- 21).

50. Holmes, J.L., et al., - *the Radical Cation Ch2oh2 +. And Related Stable Gas-Phase Ion-Dipole Complexes.* 1982. - **104**(- 10).

51. Dargel, T.K., et al., *Pyrazine diradicals, carbenes, ylides, and distonic ions probed by theory and experiment.* International Journal of Mass Spectrometry, 1999. **185/186/187**: p. 925-933.

52. Schalley, C.A., et al., - *Mass spectrometry as a tool to probe the gas-phase reactivity of neutral molecules.* 1998. - **172**(- 3).

53. Stirk, K.G. and H.I. Kenttamaa, - *Bimolecular Reactions of the Beta-Distonic Isomer of the Ethanol Radical Cation - Ch2ch2oh2+.* 1992. - **96**(- 13).

54. Stirk, K.G. and H.I. Kenttamaa, - *Radical Type Reactivity in a Gamma-Distonic Radical Cation - a Gas-Phase Experimental-Study.* 1991. - **113**(- 15).

55. Beasley, B.J., R.L. Smith, and H.I. Kenttamaa, - *a New Reagent for Structure-Specific Ion-Molecule Reactions - Dimethyl Diselenide.* 1995. - **30**(- 2).

56. Nelson, E.D., R.M. Li, and H.I. Kenttamaa, - *Reactions of tert-butyl isocyanide with distonic radical cations.* 1999. - **187**.

57. Nelson, E.D., K.K. Thoen, and H.I. Kenttamaa, - *Gas-phase reactivity of the 2,6- and 3,5-dimethylenepyridinium biradicals.* 1998. - **120**(- 15).

58. Heidbrink, J.L., K.K. Thoen, and H.I. Kenttaemaa, *Polar Effects on Iodine Atom Abstraction by Charged Phenyl Radicals.* Journal of Organic Chemistry, 2000. **65**(3): p. 645-651.

59. Tichy, S.E., et al., - *Synthesis and characterization of a distonic nitrene ion: Gas-phase reactivity of singlet and triplet N-phenyl-3-nitrenopyridinium ion.* 2001. - **123**(- 32).

60. Karapanayiotis, T., et al., - *Reactions of ionised pyridazine, aminopyrazine and aminopyridine and their isomeric alpha-distonic ions.* 2004. - **236**(- 1-3).

61. Gerbaux, P., et al., *Gas-phase bimolecular reactions between .bul.CH2-(CH2)n-C+=O distonic ions and pyridine: a combined experimental and theoretical study.* European Journal of Mass Spectrometry, 2003. **9**(4): p. 305-318.

62. Trikoupis, M.A., et al., - *Hydrogen-shift isomers of ionic and neutral hydroxypyridines: a combined experimental and computational investigation.* 2002. - **217**(- 1-3).

63. Radom, L., - *Chemistry by Computer - a Theoretical Approach to Gas-Phase Ion Chemistry - the 1990 Maccoll,Allan Lecture.* 1991. - **26**(- 5).

64. Uggerud, E., - *Properties and Reactions of Protonated Molecules in the Gas-Phase - Experiment and Theory.* 1992. **- 11**(- 5).

65. Longevialle, P., - *Ion-Neutral Complexes in the Unimolecular Reactivity of Organic Cations in the Gas-Phase.* 1992. **- 11**(- 3).

66. Morton, T.H., *The reorientation criterion and positive ion-neutral complexes.* Organic Mass Spectrometry, 1992. **27**(4): p. 353-68.

67. Bowen, R.D., - *the Role of Ion-Neutral Complexes in the Reactions of Onium Ions and Related Species.* 1993. **- 28**(- 12).

68. Tu, Y.P. and J.L. Holmes, - *The chemistry of solvated distonic ions: Preparation, isomerization, and fragmentation.* 2000. **- 122**(- 23).

69. Troude, V., et al., - *Preparation and reactivity of solvated distonic ions and ionized enols in the gas phase.* 1997. **- 119**(- 39).

70. Larson, J.W. and T.B. McMahon, - *Formation, Thermochemistry, and Relative Stabilities of Proton-Bound Dimers of Oxygen N-Donor Bases from Ion-Cyclotron Resonance Solvent-Exchange Equilibria Measurements.* 1982. **- 104**(- 23).

71. Meot-Ner, M., *The ionic hydrogen bond. 4. Intramolecular and multiple bonds. Protonation and complexes of amides and amino acid derivatives.* Journal of the American Chemical Society, 1984. **106**(2): p. 278-83.

72. Hrusak, J., et al., - *The hydrogen-bridged radical cation H_2O center dot center dot center dot H center dot center dot center dot O=C-OH center dot+: A combined experimental and theoretical study of its stability and dissociation chemistry.* 1997. **- 160**(- 1-3).

73. Terlouw, J.K., et al., - *Novel Gas-Phase Ions .2. Ch2=Choh/Ch3oh +. And Ch2=Choh/H2o +.* 1984. **- 62**(- 2).

74. Terlouw, J.K., et al., *Novel gas phase ions. II. [CH2:CHOH/methanol]+.bul. and [CH2:CHOH/water]+.bul.* Canadian Journal of Chemistry, 1984. **62**(2): p. 289-92.

75. Fossey, J., et al., - *Proton affinity of some radicals of alcohols, ethers and amines.* 2003. **- 227**(- 3).

76. Meot-Ner, M., *The Ionic Hydrogen Bond.* Chemical Reviews (Washington, DC, United States), 2005. **105**(1): p. 213-284.

77. Meot-Ner, M. and C.A. Deakyne, *Unconventional ionic hydrogen bonds. 1. CHd+...X. Complexes of quaternary ions with n- and p-donors.* Journal of the American Chemical Society, 1985. **107**(2): p. 469-74.

78. Meot-Ner, M. and C.A. Deakyne, *Unconventional ionic hydrogen bonds. 2. NH+...p. Complexes of onium ions with olefins and benzene derivatives.* Journal of the American Chemical Society, 1985. **107**(2): p. 474-9.

79. Meot-Ner, M. and C.V. Speller, *Filling of solvent shells about ions. 1. Thermochemical criteria and the effects of isomeric clusters.* Journal of Physical Chemistry, 1986. **90**(25): p. 6616-24.

80. Liu, K., J.D. Cruzan, and R.J. Saykally, - *Water clusters.* 1996. **- 271**(- 5251).

81. Ludwig, R., *Water: from clusters to the bulk.* Angewandte Chemie, International Edition, 2001. **40**(10): p. 1808-1827.

82.   Hunter, E. P.; Lias, S. G. "Proton Affinity Evaluation" in NIST Chemistry WebBook, NIST Standard Reference Database Number 69, Eds. P.J. Linstrom and W.G. Mallard, June 2005, National Institute of Standards and Technology, Gaithersburg MD, 20899 (http://webbook.nist.gov).

83.   Ibrahim, Y.M., et al., - *Stepwise hydration of ionized aromatics. Energies, structures of the hydrated benzene cation, and the mechanism of deprotonation reactions.* 2005. **- 127**(- 19).

84.   Davidson, W.R., J. Sunner, and P. Kebarle, - *Hydrogen-Bonding of Water to Onium Ions - Hydration of Substituted Pyridinium Ions and Related Systems.* 1979. **- 101**(- 7).

85.   Meot-Ner, M. and L.W. Sieck, *The ionic hydrogen bond. 1. Sterically hindered bonds. Solvation and clustering of protonated amines and pyridines.* Journal of the American Chemical Society, 1983. **105**(10): p. 2956-61.

86.   Hunter, E.P.L., S. G., *"Proton Affinity Evaluation" in NIST Chemistry WebBook, NIST Standard Reference Database Number 69, Eds. P.J. Linstrom and W.G. Mallard, , .* National Institute of Standards and Technology, Gaithersburg MD, 20899 (http://webbook.nist.gov), June 2005.

87.   Bohme, D.K., - *Proton Transport in the Catalyzed Gas-Phase Isomerization of Protonated Molecules.* 1992. **- 115**(- 2-3).

88.   Petrie, S., et al., *Experimental study of HCN+ and HNC+ ion chemistry.* Journal of the American Chemical Society, 1990. **112**(20): p. 7121-6.

89.   Audier, H.E., et al., - *Catalyzed Isomerization of Simple Radical Cations in the Gas-Phase.* 1994(- 20).

90.   Cunje, A., et al., - *Interconversion of ROC+ and RCO+ (R = H and CH3): Gas-phase catalysis by argon and dinitrogen.* 1998. **- 102**(- 2).

91.   Daly, G.M., et al., - *Termolecular proton transfer reactions assisted by ionic hydrogen bond formation: Reactions of aromatic cations with polar molecules.* 1996. **- 104**(- 20).

92.   Silverman, J., et al., - *Pulse-Radiolysis Studies on Short-Lived Intermediates in Radiation-Induced Polymerization of Bulk Styrene and Methanol Styrene Solutions.* 1983. **- 22**(- 6).

93.   Mahmoud, H., et al., - *Resonant two-photon ionization spectroscopy of styrene (methanol), clusters, n=1-9.* 2003. **- 107**(- 31).

94.   Postma, R.; Ruttink, P. J. A.; Duijneveldt, F. B.; Terlouw, J. K.; Holmes, J. L. Can. J. Chem. 1984, 62, 289.

95.   Herbst, E., *Chemistry in the interstellar medium.* Annual Review of Physical Chemistry, 1995. **46**: p. 27-53.

96.   Okumura, M., et al., *Infrared spectra of the solvated hydronium ion: Vibrational predissociation spectroscopy of mass-selected H3O+.(H2O)n.(H2)m.* Journal of Physical Chemistry, 1990. **94**(9): p. 3416-27.

97.   Meot-Ner, M. and F.H. Field, *Proton affinities and cluster ion stabilities in carbon dioxide and carbon disulfide. Applications in Martian ionospheric chemistry.* Journal of Chemical Physics, 1977. **66**(10): p. 4527-31.

98.   Hiraoka, K., et al., *Stability and structure of cluster ions in the gas phase: carbon dioxide with chloride ion, oxonium, carbon dioxide conjugate monoacid, and oxomethylium.* Journal of Chemical Physics, 1986. **84**(4): p. 2091-6.

99.   Meot-Ner, M., et al., *The Carbon Lone Pair as Electron Donor. Ionic Hydrogen Bonds in Isocyanides.* Journal of the American Chemical Society, 1997. **119**(43): p. 10430-10438.

100.   Herbst, E., *Chemistry in the Interstellar-Medium.* Annual Review of Physical Chemistry, 1995. **46**: p. 27-53.

APPENDIX A
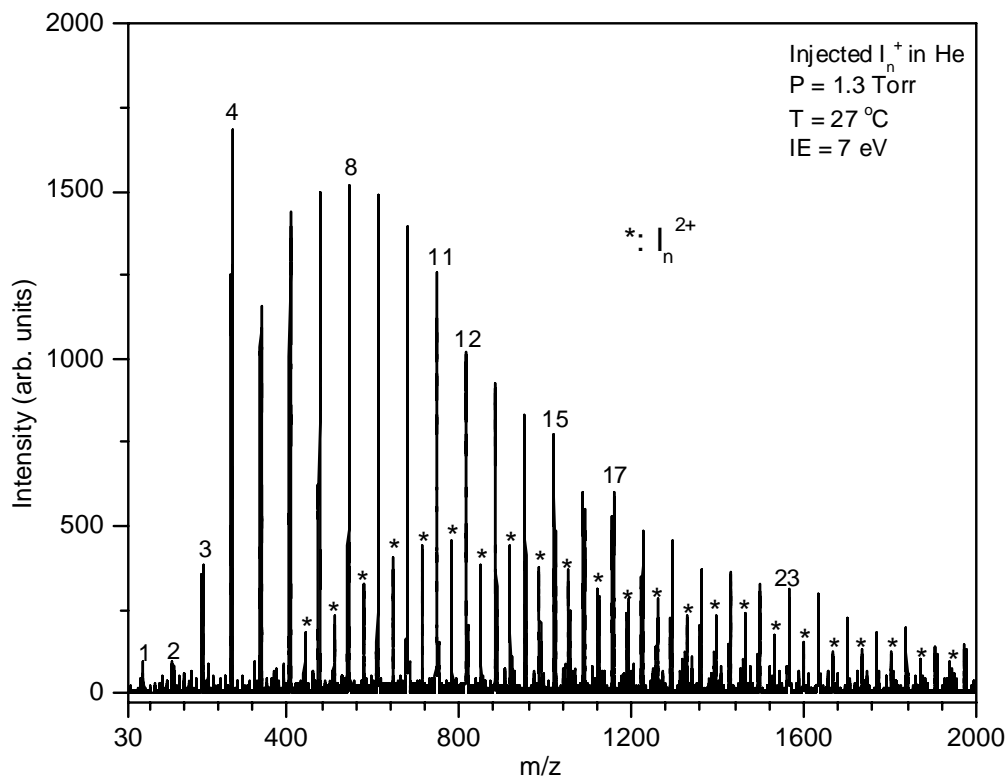
Figure 46: Collected mass spectrum of the injected isoprene cluster ions at 7 eV into the drift cell containing 1.3 Torr of pure He. The major series is relative to the singly charged isoprene cluster ions I_m^+ where m = 1-29 and the inner series is the doubly charged isoprene cluster ions I_n^{2+} starting at n = 9.
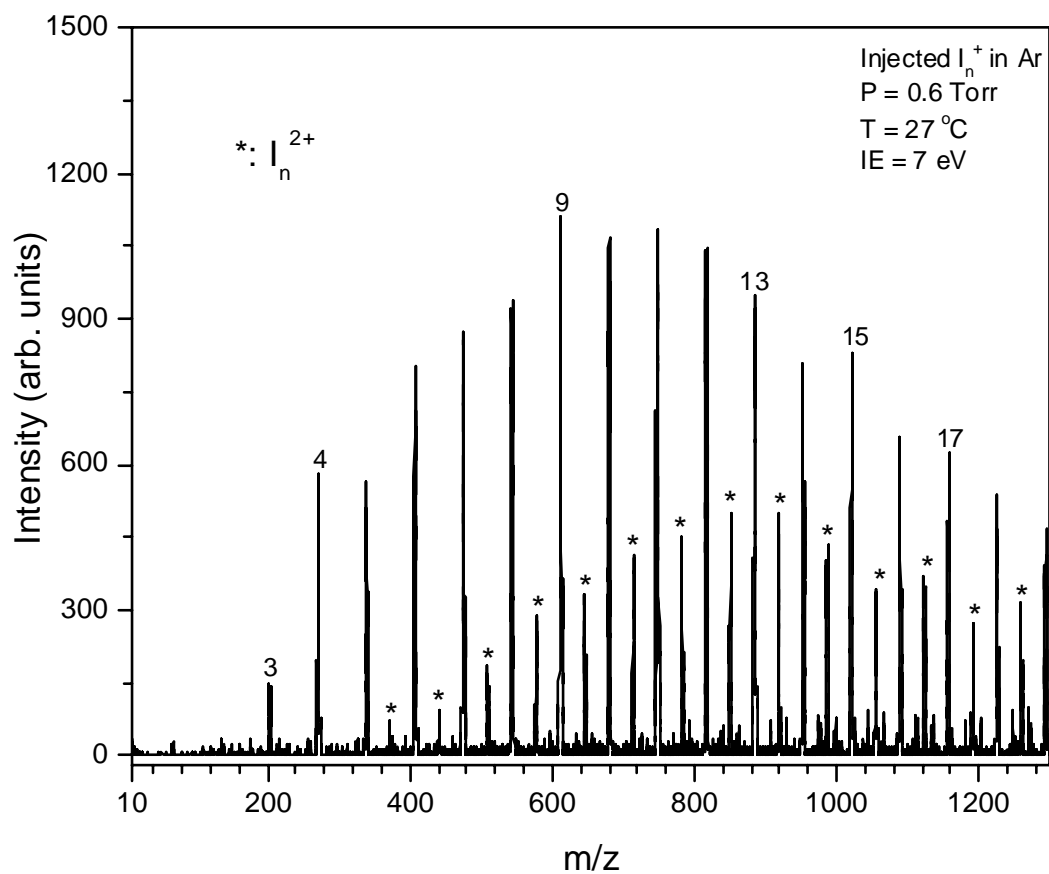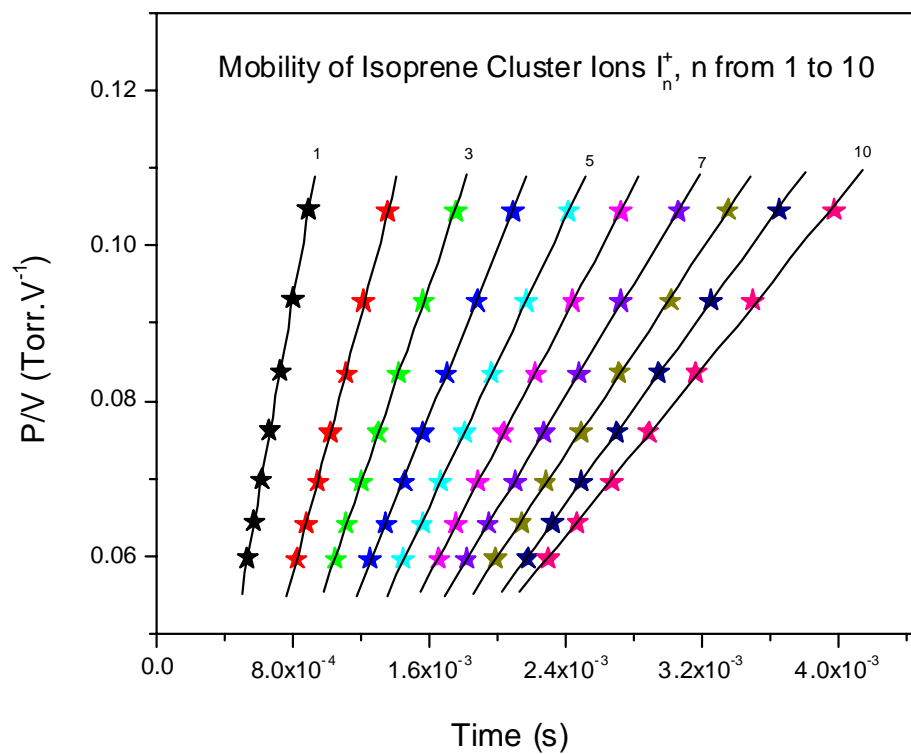
Figure 47: The injection of the isoprene cluster ions in argon buffer gas did not show a charge transfer reaction from the doubly charged cluster ions to the argon, which mean that the ionization potential (IP) of the doubly charged cluster ions is lower than 15.7 eV.
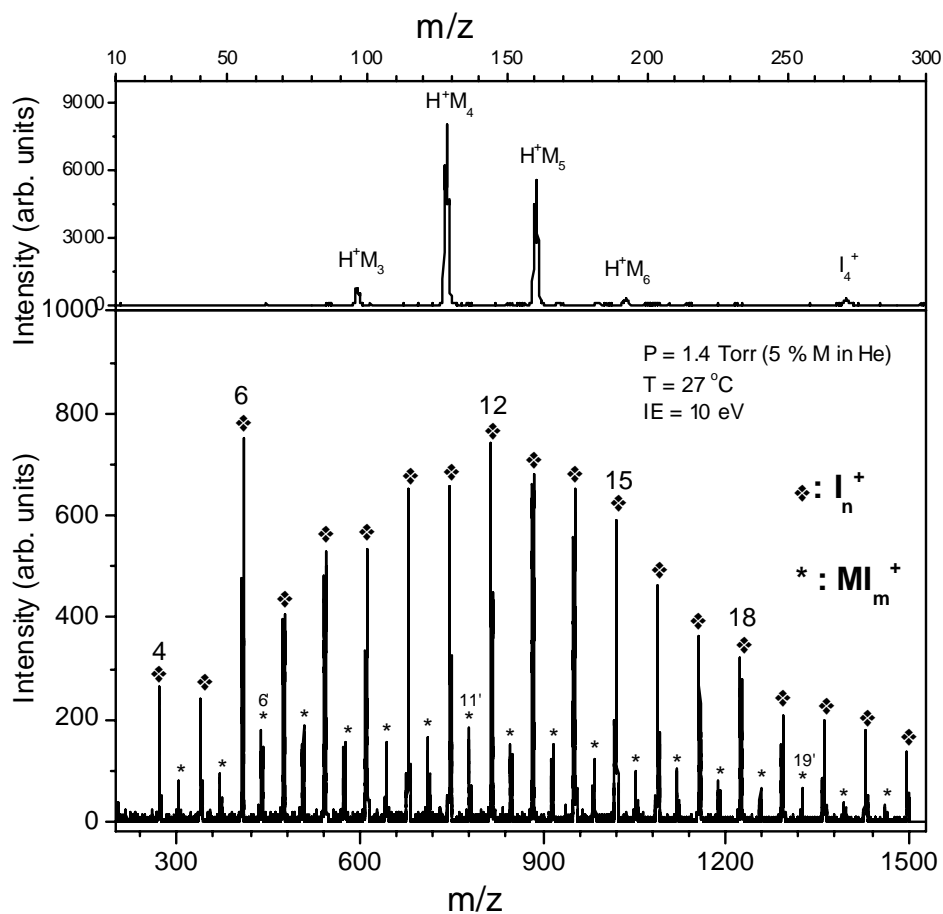
Figure 48: Collected mass spectrum following the injection of the isoprene cluster ions into the drift cell containing 1.4 Torr of 5 % methanol (CH_3OH) in He. Reaction of charge transfer from the doubly charged cluster ions to the methanol is observed and it is illustrated in the top panel by the presence of the protonated methanol clusters (H^+M_n) and in the second panel by the inner series marked by the stars, which is relative to the addition of isoprene on methanol (MI_n^+).
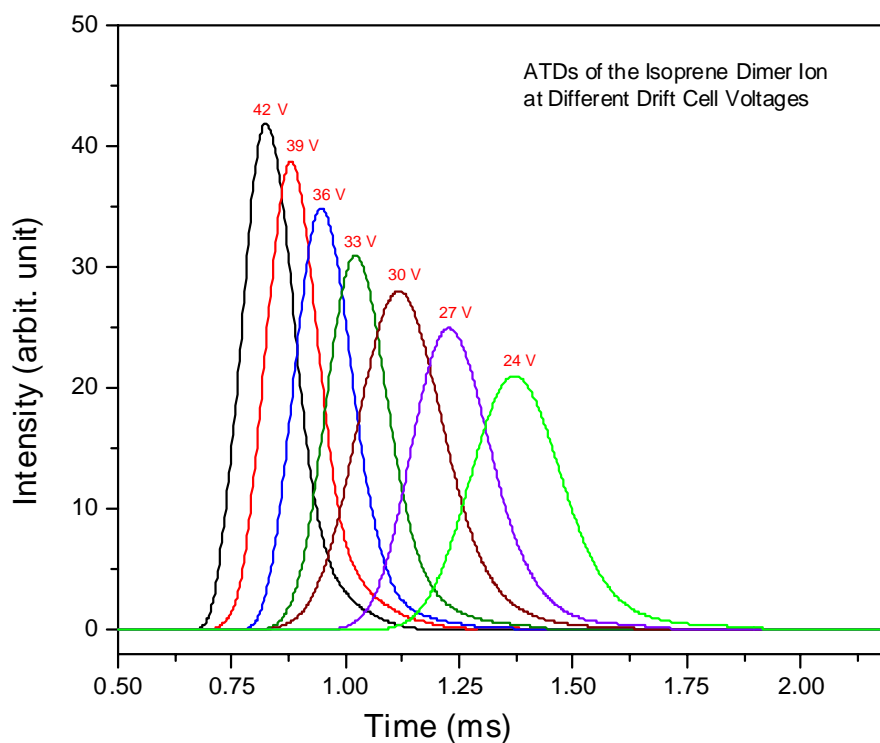
Figure 49: Collected ATDs of the isoprene dimer cation at different drift cell voltages showing the relation between the drift time of the ion and the applied voltage to the drift cell; when the cell voltage is decreased, the drift time is increased.

Figure 50: Plot of the mobilities of the isoprene cluster ions (I_n^+) for n = 1-10.

**Table 12:** Collected collision cross-sections (in $\mathring{A}^2$) of the singly charged isoprene cluster ions $I_n^{\bullet+}$

mass	68	136	204	272	340	408	476	544
Ω ($\mathring{A}^2$)	47.2	71.1	90.1	108.9	124.9	143.1	162	175.7

Table 13: Collision cross-sections of isoprene cluster ions with contributions from singly and doubly charged species.

mass	612	680	748	816	884	952	1020	1088	1156	1224	1292	1360
Ω ($\mathring{A}^2$)	179.8	193.4	198.3	203.5	207.5	211.5	217.5	222	229.6	236.7	243.1	247.6

Table 14: Collision cross-sections of the doubly charged isoprene cluster ions $I_n^{2\bullet+}$

| Ion (mass)	646	714	782	850	918	986	1054	1122
Ω ($\mathring{A}^2$)	178.3	186.3	193	199.5	208	213	220	228.4
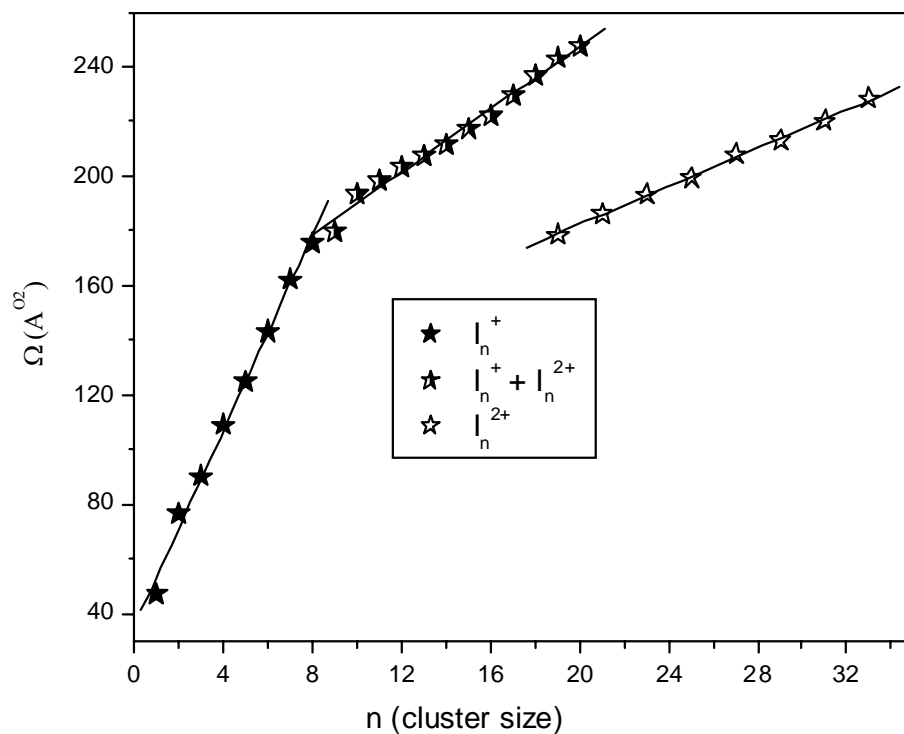
Figure 51: Plots of the collision cross-sections (Ω in $\mathring{A}^2$) as a function of the cluster size (n). Full stars for the singly charged isoprene cluster ions (I_n^+), empty stars for the doubly charges isoprene cluster ions (I_n^{2+}) and the half-full stars for the mixed isoprene cluster ions
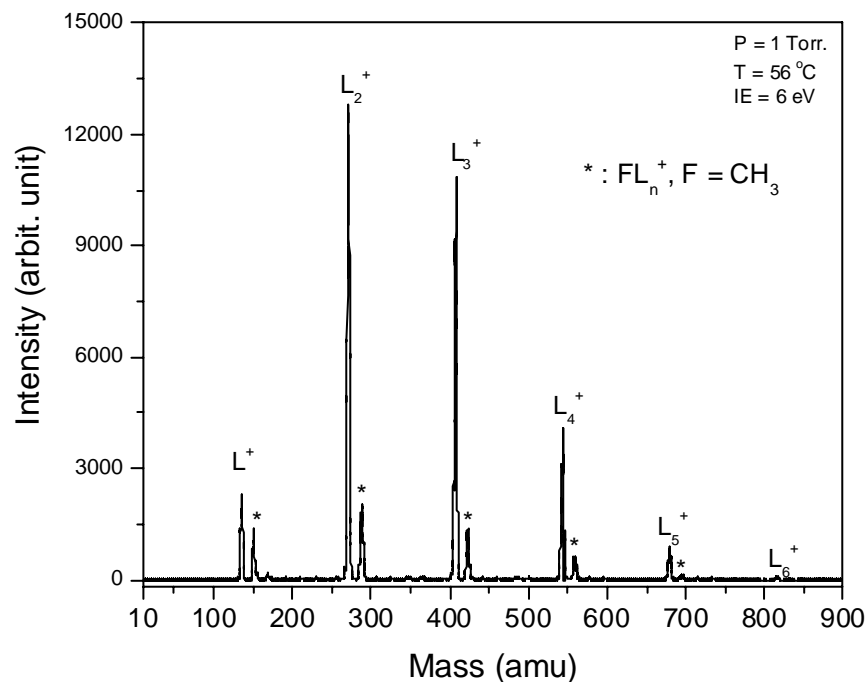
Figure 52: Mass spectra collected after the injection of limonene cluster ions into the drift cell filled with one Torr of pure He. The temperature is maintained at 26 °C, and the injection energy is 6 eV. The mass spectrum is showing a major cluster series relative to L_n^+ for n =1-6 and a lower intensity cluster series for the addition of limonene on CH_3 fragment.

Table 15: Experimental mobility values for the limonene collected at different drift cell pressures.

| Ion	W (Å^2)
L^+	71.1
L_2^+	113.2
L_3^+	149.5
L_4^+	179.4
L_5^+	211.2
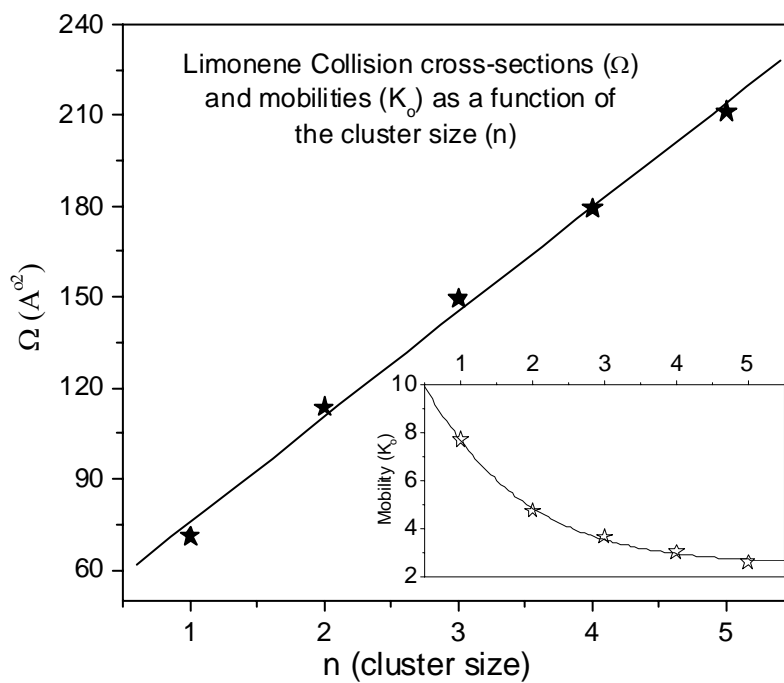
Figure 53: Plots of the measured collision cross-sections (Ω) of the limonene cluster ions and their mobilities (the inside plot) as a function of the cluster size (n).
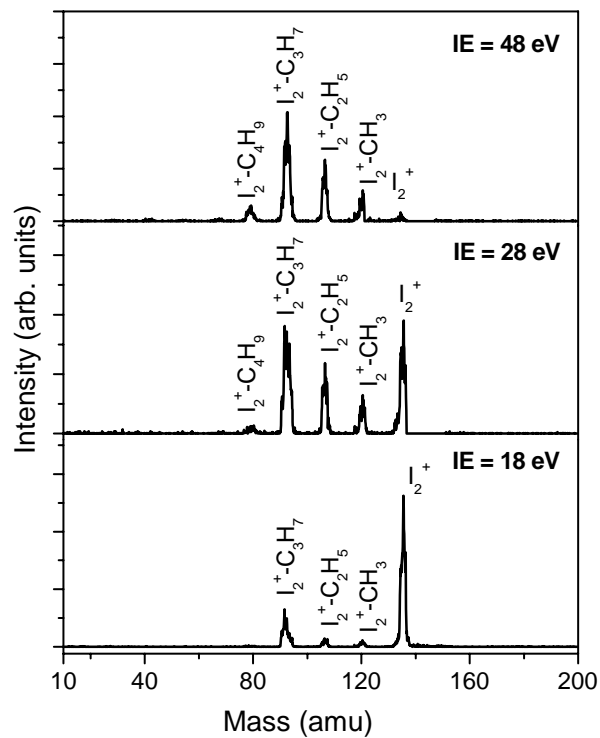
Figure 54: Dissociation of the isoprene dimer cluster ion. When the injection energy is increased to 48 eV, the dimer shows dissociated fragments without losing an isoprene unit.
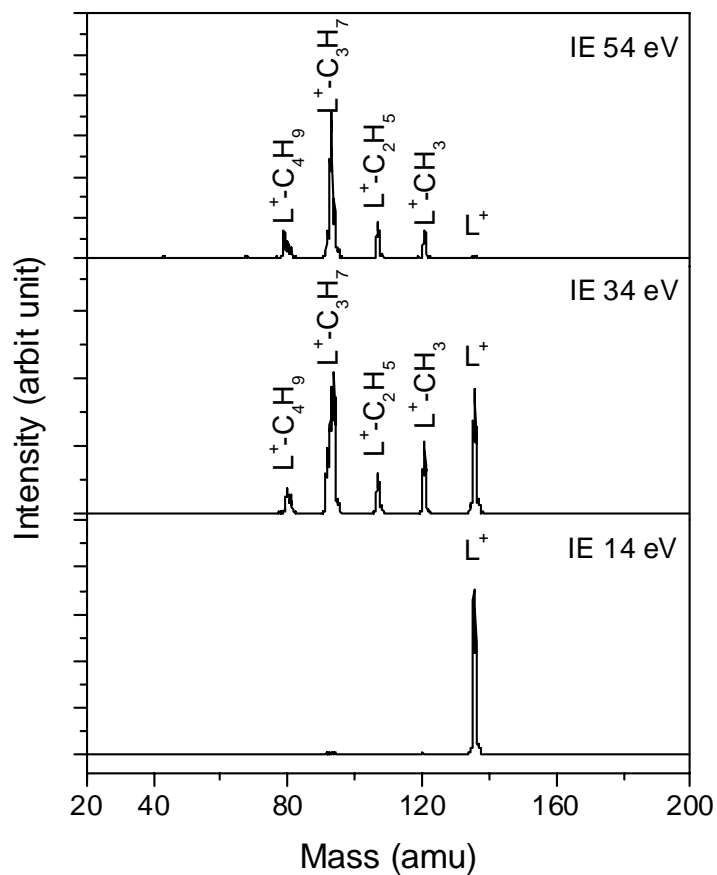
Figure 55: Collected mass spectra by scanning the second quadrupole, following the injection of mass-selected limonene monomer ion at different injection energies, showing the resulting fragments.
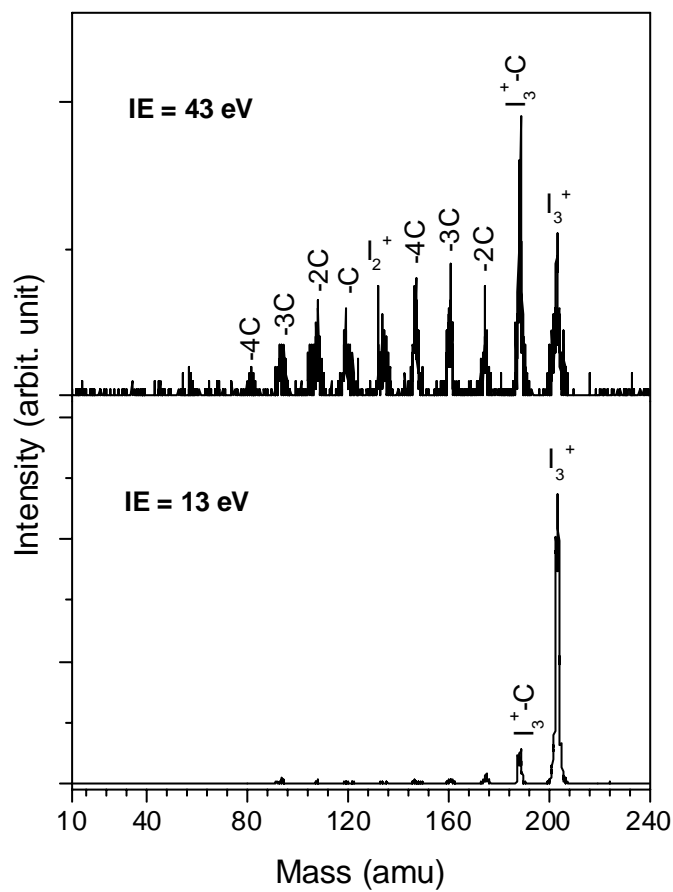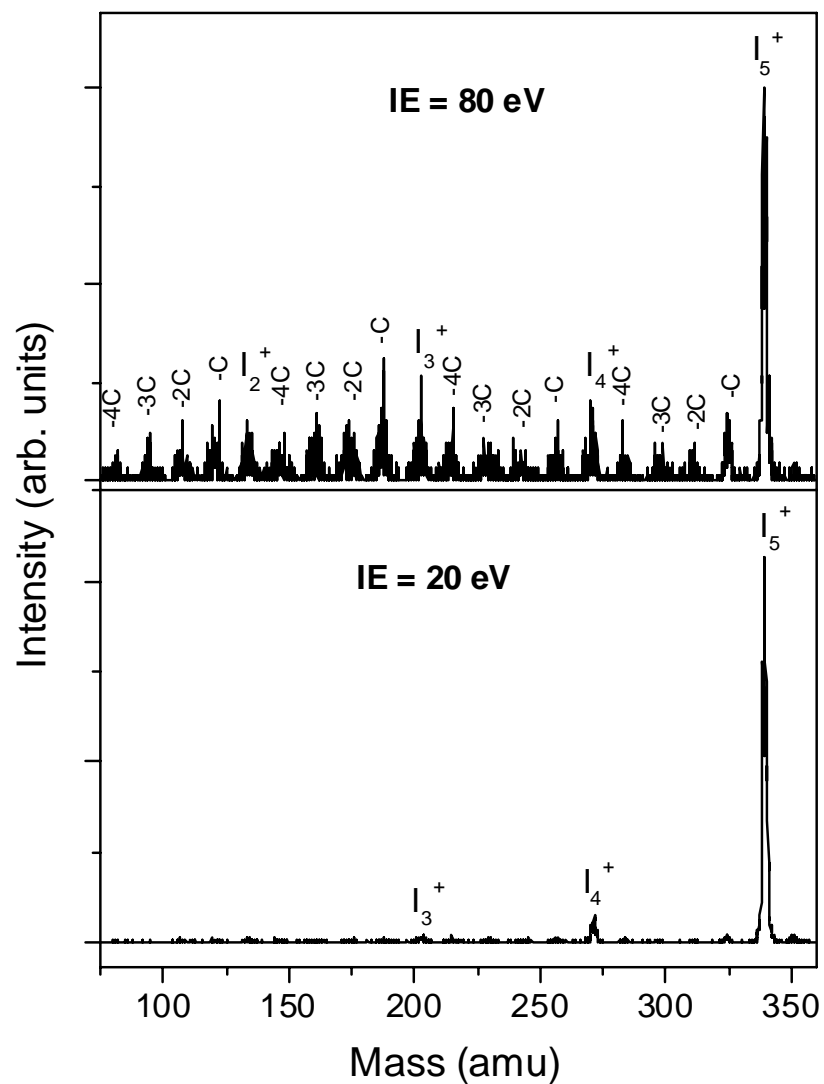
Figure 56: Collected mass spectra at different injection energies showing the resulting fragmentation of the isoprene trimer cluster ion (I_3^+).
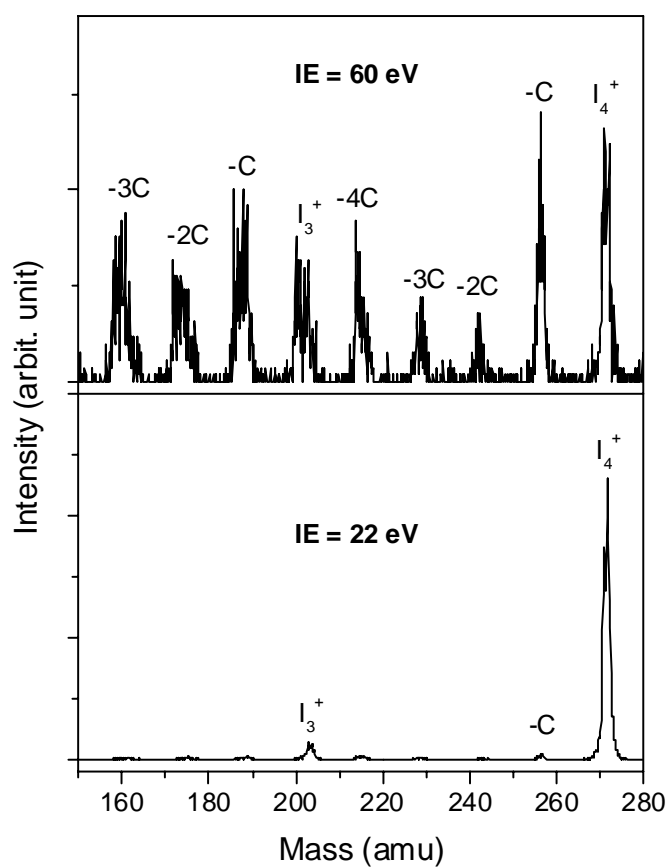
Figure 57: Dissociation of the isoprene tetramer cluster ion (I_4^+) at different injection.

Figure 58: Injection energy study for the dissociation of the pentamer isoprene cluster ion.

<u>VITA</u>

Ridha B. Mabrouki

<u>EDUCATION</u>

Ph.D. in Physical Chemistry May 2007

Virginia Commonwealth University, Richmond, Va

Advisor: **M. Samy El-Shall**

Thesis title: <u>Drift Tube Ion Mobility Measurements for Thermochemistry, Kinetics and Polymerization of Cluster Ions</u>

Bachelor of Science in Physics and Chemistry (July 1998), (Graduated with High Honor), University of Sfax, College of Life Sciences, Sfax, Tunisia

<u>SKILLS AND EXPERTISE</u>

Instrumentation

- Ion-Mobility Mass Spectrometry technique (IM-MS)
- Ion Mobility Spectrometry (IMS)
- Resonance Enhanced Multi-Photons Ionization (REMPI)
- Resonance Enhanced two Photons Ionization (RE2PI)
- Time of Flight Mass Spectrometry (ToF-MS)
- Reflectron Time of Flight Mass Spectrometry (RToF-MS)
- Matrix-Assisted Laser Desorption-Ionization Time-of-Flight Mass Spectrometry (MALDI-ToF-MS)

Software

- PC platform: Microsoft Excel, Microsoft PowerPoint, Microsoft Word Origin-LAB 6.1, 7.0 and 7.5
- Extrell CMS
- IntelliCAD
- MobCal, Force 2.0
- MathCad

Data Acquisition

- National Instrument GPIB interface
- Multi-Channel Scaling (MCS)
- Extrell Merlin Spectral Scan (EMSS)
- Cluster program

<u>RELEVANT EXPERIENCE</u>

Research Assistant, Virginia Commonwealth University, Richmond Va, 03/03-Present

- Establishing ion mobility mass spectrometry as a unique tool to address challenging scientific problems
- Use ion mobility mass spectrometry (IM-MS) for:

- o Gas phase structures investigation and characterization of homo- and hetero-molecular cluster ions
- o Thermochemistry and kinetics of solvated ionized organic molecules
- o Thermal dissociation and activation energy of unimolecular cluster ions
- o Cationic polymerization of unsaturated hydrocarbons in the gas phase examples of styrene, isoprene, limonene, etc
  - Utilize REMPI and RE2PI techniques to study the spectroscopy of some organic chromophores
  - Use time of flight mass spectrometry (ToF-MS) and reflectron time of flight mass spectrometry (R-ToF-MS) to study the gas phase solvation of anionic and cationic metal cluster ions
  - Use MALDI Matrix-Assisted Laser Desorption-Ionization Time-of-Flight Mass Spectrometry (MALDI-ToF-MS)

Teaching Assistant, Virginia Commonwealth University, Richmond Virginia
- o Taught 32 students physical chemistry lab 303 levels, 01/07-05/07
- o Taught approximately 72 students chemistry lab 101 and 102 levels, 08/03-05/04
- o Graded papers and answered student questions
- o Prepared lab and maintained it for students' safety

Research Assistant, University of Life Sciences, Tunisia, 09/98-07/00
- o Run experiments for organic synthesis of natural products
- o Helped grade exams and papers

AWARDS

Chairman Award in Gordon Research Conference on Gaseous Ions: Structures, Energetics & Reactions 2005

AFFILIATION

- American Society of Mass Spectrometry
- American Chemical Society
- Nature Methods